國立臺灣大學電機資訊學院生醫電子與資訊學研究

博士論文

Graduate Institute of Biomedical Electronics and Bioinformatics

College of Electrical Engineering and Computer Science

National Taiwan University

Doctoral Dissertation

自組裝人類小動脈晶片及其在動脈功能檢測及疾病模型之應用

Self-assembled Human Arteriole-on-a-Chip for Arterial Functionality Testing and Disease Modelling

施凡妮

Subhashree Shivani

指導教授：林致廷　博士

許聿翔　博士

Advisors: Prof. Chih-Ting Lin, Ph.D.

Prof. Yu-Hsiang Hsu, Ph.D.

中華民國 114 年 12 月

December, 2025

doi:10.6342/NTU202600103

Acknowledgements

First, I would like to convey my deepest gratitude to my advisor Prof. Chih-Ting Lin for accepting me as his student in the third year of my degree program. His steady guidance and encouragement helped me navigate through many academic and administrative challenges and got me many scholarship opportunities. His kind words and swift processing of official matters saved me valuable time. His belief in me and encouragement during difficult times gave me the strength to complete this dissertation.

Secondly, I would like to sincerely thank my co-advisor Prof. Yu-Hsiang Hsu. I have worked under Prof. Hsu's guidance since 2015 (during my Masters) and in these 10 years of knowing him, he has taught me everything I know about wet lab experiments and research ethics. His patience and positive attitude towards even failed experiments showed me how to truly look at data and assess the results. Other than being an extraordinary professor, his empathetic leadership has impacted me the most. My pregnancy in 2024 was a happy journey, only due to his constant emotional and financial support. He fully funded me during the months I could barely come to work and also during my difficult post-partum phase. His kindness helped me push through many difficult times and focus on doing the experiments. Even when our experiments failed multiple times during the optimization phase, he always encouraged me to look forward. Although he is extremely busy with so many students, he always has time for everyone and a kind heart to listen to everyone's request. His teachings are beyond the academic setup and I hope I can implement a few of his qualities in my future roles.

Next, I would like to thank CJ who is a dear friend in Lab 102. I have also known him since 2015, and talking to him releases most of my stress. He helped me understand the microfluidic designs and helped me simulate many theories. More than that he helped me

doi:10.6342/NTU202600103

by just being there to talk about different aspects of life and research. I would also like to thank HJ for being a sweet junior and helping me maintain my devices whenever I was out of town. Other members of Lab 433 have been great help during my PhD in many aspects and I am obliges to each one of them.

I would like to thank the NTU OIA and the EECS Department for providing financial support through scholarships during my PhD journey. I am also grateful to the Chung Hwa Rotary Club, Taiwan, for recognizing my work and awarding me their Outstanding Scholarship in 2022.

Finally, I would like to thank my family and my 10-month old for being the backbone of this journey. I would be forever grateful to my father and husband, who encouraged me to switch advisor during my third year due to increasing mental stress. The switch gave me clarity, introduced me to this amazing field of OoC and got me such kind and supportive advisors that I am able to graduate while having a baby, within a span of four years. I am indebted to my parents and parents-in-laws for being the sweetest grandparents and staying with us for almost one year and taking care of their grandchild. It is difficult to stay in a foreign country for 6-months at stretch, but they never complained and happily supported me during my post-partum. Without them it was impossible to finish journal or write this dissertation. I am thankful to my 10-month old for allowing me to perform experiments during pregnancy and also being patient enough to finish my dissertation.

Lastly, none of this would have been possible without the divine interventions. I thank Lord Jagannath for watching over me and giving me strength when I was on the verge of giving up. Your blessings carried me through the most difficult moments of this journey.

doi:10.6342/NTU202600103

中文摘要

目前體外血管模型主要基於微壓印、人工血管或自組裝微血管為主。然而因主要技術是使用靜脈內皮細胞或其他多能幹細胞轉化的內皮細胞，所培養出的血管以微血管為主。然而，動脈在調節血管張力和疾病進展中是為主要血管組織，但如何在體外重建其多層細胞結構和血液動力學環境仍然是此領域的重大挑戰。在本研究中，我們開發了一種微流控平台，能夠共培養人類動脈內皮細胞、平滑肌細胞（SMC）和纖維母細胞，誘使其產生自組裝病培養出具有功能性的小動脈組織。本研究藉由在經片中產生低氧條件下，誘導血管生成和並將其發展成穩定且成熟的小動脈組織，並證明週期性血流會使其產生動態重塑機制。本研究透過改變剪應力，我們證實了小動脈的血流依賴性的血管重塑機制，以實驗證明在靜態培養下會喪失血管功能，在低剪應力下會誘導擴張性重塑，而高剪應力則會觸發擴張和退化性重塑，最終形成具有小動脈層狀結構的功能性血管。本研究並以有限元素分析進一步分析出剪應力與初級和次級血管發育之間的關聯。本研究亦驗證平滑肌細胞具有血管收縮及舒張之小動脈功能，並證明此小動脈模型能夠重現早期動脈粥狀硬化的疾病模型。綜合以上所述，本研究所開發的小動脈晶片能夠重現人類小動脈的關鍵組織結構、功能和病理特徵。此平台將可做為研究動脈生成、內皮層及平滑肌細胞相互作用和血管疾病的一項體外工具，並有望應用於未來的藥物測試和個人化醫療。

關鍵字 – 小動脈晶片、微流體晶片、 血管重塑、血管舒縮、動脈粥樣硬化、器官晶片、微生理系統。

doi:10.6342/NTU202600103

Abstract

Current *in vitro* vessel models are primarily based on micro-patterning, artificial vessels, or self-assembled microvascular networks. However, most studies have used venous endothelial cells (ECs) or other pluripotent-derived ECs, resulting in the formation of capillary-like vessels. Arteries play a central role in regulating vascular tone and disease progression; however, recreating their multicellular structure and hemodynamic environment *in vitro* remains a major challenge. In this study, we developed a microfluidic platform capable of co-culturing primary human arterial endothelial cells, smooth muscle cells (SMC), and fibroblasts to generate self-assembled, perfused, and functional arteriole-like networks. Guided by vasculogenesis and angiogenesis under controlled hypoxia, the vascular structures matured into stable arterioles that responded o oscillatory flow. By varying shear stresses, we demonstrated flow-dependent vascular remodeling: static cultures showed loss of perfusion, low shear induced expansive remodeling, and high shear triggered both expansive and regressive remodeling, resulting in perfused vessels with an arteriole-layered anatomical structure. Finite element analysis further revealed the association between the magnitude and distribution of shear stress and the development of primary and secondary vessel hierarchies. Arteriole functionality was validated by SMC-mediated vasomotion, demonstrating the model's ability to recapitulate early atherosclerotic events. Together, these results establish a physiologically relevant arteriole model that recapitulates key human arteriole features and enables studies of arteriogenesis, endothelial–SMC interactions, vascular disease, and drug testing.

Keywords – Arteriole-chip, Microfluidics, Vascular remodeling, Vasomotion, Atherosclerosis, Organ-on-a-Chip, Micrphysiological system.

doi:10.6342/NTU202600103

Contents

doi:10.6342/NTU202600103

doi:10.6342/NTU202600103

doi:10.6342/NTU202600103

List of Abbreviations

2D	:	2 dimension
3D	:	3 dimension
ANG	:	Angiogenin
BBB:	:	Blood Brain Barrier
bFGF	:	Basic Fibroblast Growth Factor
bMFA	:	bioinspired microfluidic assay
CAD	:	computer-aided design
CD31	:	Cluster of Differentiation 31
CFD	:	Computational Fluid Dynamic
COVID-19	:	Coronavirus disease
CVD	:	Cardio Vascular Disease
DAF-FM	:	4-amino-5-methylamino-2′,7′-difluorofluorescein
DAPI	:	4′,6-diamidino-2-phenylindole
DLL4	:	Delta-like ligand 4
EC	:	Endothelial Cell
ECFC-EC	:	endothelial colony forming cell-derived endothelial cells
ECM	:	Extra Cellular Matrix
EGM-2	:	Endothelial Growth Medium-2
eNOS	:	endothelial Nitric Oxide Synthase
EPC	:	Endothelial Progenitor Cells
FGF-2	:	Fibroblast Growth Factor-2
FITC	:	Fluorescein isothiocyanate

doi:10.6342/NTU202600103

FN	:	Fibronectin
HaEC	:	Human Aortic Endothelial Cells
HCCLM9	:	hepatocellular carcinoma cell line
HGF	:	Hepatocyte growth factor
HUAEC	:	Human Umbilical Artery Endothelial Cell
HUSMC	:	Human Umbilical Smooth Muscle Cell
HUVEC:	:	Human Umbilical Vein Endothelial Cell
IA	:	Intussusceptive Angiogenesis
IGF-1	:	Insulin-like Growth Factor 1,
IL-1β	:	Interleukin-1 beta
IPA	:	Isopropyl alcohol
iPSC	:	induced Pluripotent Stem Cell
MAPK	:	mitogen-activated protein kinase
MFD	:	Microfluidic Network
MMP	:	Matrix Mellao Proteinases
NF-κB	:	Nuclear Factor kappa-light-chain-enhancer of activated B cells
NHLF	:	Normal Human Lung Fibroblast
NO	:	Nitric Oxide
OoC	:	Organ-on-a-chip
PBS	:	Phosphate Buffer Solution
PDGF	:	Platelet Derived Growth Factor
PDGFR	:	Platelet Derived Growth Factor Receptor
PDMS	:	Polydimethylsiloxane
PECAM-1	:	Platelet Endothelial Cell Adhesion Molec**u**le-1

doi:10.6342/NTU202600103

PI3K/Akt	:	Phosphoinositide 3-kinase/Protein Kinase B
PMA	:	Phorbol 12-myristate 13-acetate
SA	:	Sprouting Angiogenesis
SDF	:	Stromal cell Derived Factor
SMC	:	Smooth Muscle Cell
TIME	:	telomerase-immortalized human microvascular endothelial cell
TMAO	:	Trimethylamine N-oxide
TNF-α	:	Tumor Necrosis Factor-alpha
VCAM-1	:	Vascular Cell Adhesion Molecule 1
VEGF	:	Vascular Endothelial Growth Factor
VEGFR	:	Vascular Endothelial Growth Factor Receptor
VoC	:	Vessel-on-a-chip
VSMC	:	Vascular Smooth Muscle Cells
vWF	:	von Wilebrand Factor
WSS	:	Wall Shear Stress

doi:10.6342/NTU202600103

1. Introduction

1.1 Significance

Cardiovascular diseases (CVD) such as ischemic heart attack and stroke account for approximately 13% of the deaths worldwide [1]. A typical timeline for obtaining a new CVD drug is around 10-15 years and costs almost around $1.1 - $2 billion.[2] However, most of the developed drugs fail in clinical trial due to various reasons, such as toxicity and efficacy. The major reason for failure is the reliance on animal models, which neither accurately reflect human anatomy nor genetically represent human *in vivo* physiology [3], [4], [5]. Hence, for faster and reliable drug development, it is important to design disease models in human-like systems. Moreover, most CVDs arise fundamentally due to the structural or functional abnormalities in the blood vessels. Therefore, it suggests that to treat CVDs we need to understand the underlying vascular pathobiology. A blood vessel consists of three layers: inner endothelial cell (EC) layer (initima), middle muscular and elastic layer (media) and outer supporting layer (adventitia) composed of connective tissues [6]. Understanding the key molecular mechanisms and cell–cell interactions across these vascular layers is essential for uncovering the underlying causes of diseases such as thrombosis, atherosclerosis, and coronary artery disease. Such insights would enable the identification of cellular-level dysfunctions and the development of targeted therapeutics with improved efficacy.

2D models have been instrumental in high-throughput screening of drugs despite their high degree of error rate due to poor recapitulation of *in vivo* complexity [7]. Hence, it is essential to develop 3D models that closely replicate the desired organ, enabling faster and more accurate drug development. To achieve this purpose, organ-on-a-chip (OoC) technology has recently gained massive popularity.[8] Many OoC platforms have recently

doi:10.6342/NTU202600103

gained wide-ranging application for different human organ mimicking platforms, such as lungs[9], gut[10], kidney[11], heart[12], liver[13], brain[14] among others. These systems have been further utilized to develop various disease models, which have been instrumental in understanding the pathobiology of underlying disease mechanisms. In the context of blood vessels, numerous researchers have engineered vascular structures within microfluidic platforms, collectively referred to as vessel-on-a-chip (VoC) systems, using various techniques to investigate vessel formation, development, and remodeling [15]. The major bottleneck in developing *in vitro* vessels is the recapitulation of heterogeneity of the vascular structure. The three-layered structure, comprising the intima, media and adventitia, is formed *in vivo* due to complex cell-cell interactions. Moreover, vessel types in vivo vary significantly across organs due to differences in their resident cell populations. Specifically, because blood flows along the intimal surface, endothelial cells (ECs) serve as the primary sensors of fluid shear stress. As a result, the hemodynamic environment experienced by a vessel is largely defined by the organ-specific characteristics of its endothelial cells. Hence, designing any vascular disease model requires the organ-specific cell composition for better understanding of the fluid dynamics and accurate replication of disease *in vitro.* A key limitation of current vessel-on-a-chip (VoC) platforms is the narrow range of endothelial cell types typically used. Most studies rely on human umbilical vein endothelial cells (HUVECs) or endothelial cells derived from pluripotent stem cells. Moreover, the self-assembled VoC models lack the middle elastic layer, thus developing capillary-like structures instead of replicating the true architecture of an artery or vein. Although, blood continuously flows through vessels, the role of sustained shear stress in vascular development remains poorly understood. Therefore, to address these gaps, there is a critical need for VoC models that incorporate diverse EC types, recreate more physiologically relevant vascular wall

doi:10.6342/NTU202600103

structures, and integrate microfluidic designs capable of maintaining continuous flow. Such advancements would deepen our understanding of cell–cell interactions, hemodynamic regulation, and the mechanisms underlying the progression of vascular disease.

1.2 Research Aims

The specific aims of this dissertation are divided into following sections as follows:

1.2.1 Development of perfusable arteriole-on-a-chip

The primary aim of this dissertation is to develop an arteriole-on-a-chip model that can develop arteriole vessels with functional smooth muscle layer surrounding the luminal endothelium. The cell construct is composed of three cell types: human umbilical arterial endothelial cells (HUAECs), human umbilical smooth muscle cells (HUSMCs) and normal human lung fibroblasts (NHLFs). We hypothesize that co-culturing these cells within an *in vivo* like micro-environment could induce vasculogenesis and angiogenesis to form an arteriole-like structure that recapitulates the layered architecture of a human artery.

After developing perfusable arterioles via vasculogenesis and angiogenesis, our overarching aim is to introduce arteriogenesis on the chip. Studies have shown that shear stress induced by continuous blood flow remodels the blood vessels [16]. However, the extent of remodeling due to varying shear stress is poorly understood. Hence, we aim to introduce continuous fluid flow through the perfusable vessels at varying magnitudes to understand flow-mediated vascular remodeling. To further approximate *in vivo* conditions, the applied flow will be pulsatile at 1 Hz, corresponding to the physiological heart rate of humans [17].

doi:10.6342/NTU202600103

1.2.2 Verifying arteriolar functionality

1.2.2.1 Assessing vasomotion in response to vasostimulants

The next aim is to verify if the developed arteriole can sustain *in vivo* functionalities. We will first assess the ability of the arterioles to support blood perfusion. Perfusable devices will be introduced to the blood flow, and we will examine whether the blood can traverse the engineered vessel network. This will validate the system for modeling blood-related diseases.

Next, we aim to evaluate the functional competence of the SMCs by assessing their contractile ability. The primary role of SMCs *in vivo* is to contract or relax in response to the biochemical cues transmitted from the endothelial cell (EC) layer. We aim to introduce vasostimulant to perfusable devices and monitor the ability of the SMCs to respond appropriately, confirming SMCs' vasomotion ability within the engineered arterioles.

1.2.2.2 Verifying NO production in response to shear stress

When blood flows across the endothelial surface, the frictional force (shear stress) is sensed by mechanoreceptors such as PECAM-1, VE-cadherin, integrins, and the glycocalyx. This mechanical signal activates intracellular pathways, including PI3K/Akt and calcium–calmodulin signaling, that lead to the phosphorylation and activation of endothelial nitric oxide synthase (eNOS). Activated eNOS converts L-arginine to NO [18], [19]. This released NO diffuses into SMC layer, causing vasodilation, reducing vascular load and maintaining blood flow homeostasis. Hence, it suggests that NO production should be higher in high flow than in low flow or static conditions.

First, we will generate perfusable MVNs under both static and high flow conditions. Following perfusion, we will assess nitric oxide (NO) production by

doi:10.6342/NTU202600103

immunostaining the devices with NO-sensitive fluorescent probes. By comparing the two groups, we expect to observe increased NO levels in vessels exposed to higher flow rates, and therefore higher shear stress, indicating that our arterioles exhibit physiologically relevant mechanotransductive responses.

1.2.3 Arterial disease modeling

We aim to develop arterial disease in our system to prove their efficacy as a platform for disease modeling. We aim to develop two arterial diseases: (i) thrombosis and (ii) atherosclerosis. The mechanism of developing these two models is described briefly below:

1.2.3.1 Arterial thrombosis

The primary cause underlying most heart attacks and strokes is thrombosis. To understand the cell-cell interaction during thrombosis is critical to designing better effective drugs. There are basically three pathways by which thrombus is formed: (i) endothelial injury (ii) blood flow abnormalities and (iii) hypercoagulability of blood [20]. In our dissertation, we aim to develop thrombus via stimulating endothelial injury. We aim to inflame the endothelial layer to release von Wilebrand factor (vWF), a glycoprotein that promotes platelet adhesion [21], [22], [23]. Under physiological conditions, vWF is stored in Weibel–Palade bodies within endothelial cells and is released upon endothelial activation or injury [24]. Once released, vWF binds to exposed subendothelial collagen and circulatory platelets via glycoprotein Ib–IX–V complexes, serving as a critical initiator of thrombus formation.

Following the induction of vWF release, we will perfuse whole blood through the engineered vessels. If the endothelial cells respond as expected and secrete sufficient vWF, platelets in the blood will adhere to the activated endothelium and to each other,

doi:10.6342/NTU202600103

forming microthrombi within the engineered vessels. By monitoring thrombus formation in this perfusable system, we can evaluate the ability of our system in developing platelet-mediated arterial thrombus formation.

1.2.3.2 Atherosclerosis

Atherosclerosis is a chronic vascular disease in which vascular plaques are formed due to the accumulation of lipids, inflammatory cells and connective tissues in the arterial wall [25]. In chronic atherosclerosis, monocytes adhere and differentiate into macrophages and subsequently become foam cells. SMCs also migrate into the intima and form a fibrous cap over lipids by secreting extracellular matrix (ECM) [26].

Trimethylamine-N-oxide (TMAO), a gut microbiota–derived metabolite, has recently emerged as a significant contributor to atherosclerosis [27]. TMAO activates inflammatory pathways in endothelial cells through p38 MAPK and NF-κB, thereby increasing the expression of adhesion molecules, including VCAM-1, and promoting leukocyte adhesion [28]. TMAO enhances macrophage lipid uptake by upregulating scavenger receptors (e.g., CD36, SR-A1), which promotes foam cell formation—an essential step in plaque development [29]. Hence, TMAO has multiple pro-atherogenic effects that impair endothelial cell function, enhance inflammation and oxidative stress, promote foam cell formation, and destabilize vascular structure. Hence, TMAO could be used both as a biomarker and therapeutic target in atherosclerotic-related CVDs. Hence, in our model we aimed to develop atherosclerosis by inflaming the ECs with TMAO.

We aim to flow TMAO through the developed arterioles for a few hours to inflame the ECs and activate pro-atherogenic pathways. Subsequent perfusion with blood should promote leukocyte adhesion to the inflamed ECs, representing the initial stage of

doi:10.6342/NTU202600103

atherosclerosis. This would validate the model for studying atherosclerosis and allow verifying the role of TMAO in initiating atherosclerosis.

1.3 Dissertation Structure

This dissertation is divided into six chapters:

Chapter 1 (Introduction) provides an overview of the motivation and objectives of this research, outlining the rationale for developing an arteriole-on-a-chip system. It also summarizes the key functionalities and disease-modeling applications that this platform is designed to enable.

Chapter 2 (Literature Review) reviews the literature on biological and engineering principles of vessel-on-chip systems. It begins with a discussion on cardiovascular network and the key processes in vessel formation *in vivo*. Next, it reviews various methods for developing vessels-on-a-chip and their applications in disease modeling. Finally, it examines studies on flow and arteriogenesis, highlighting the rationale and necessity for developing an arteriole-on-a-chip system.

Chapter 3 (Design Concept) discusses the design principles of the proposed arteriole-on-a-chip microfluidic platform, which aims to provide a physiologically relevant environment for arterial tissue culture. It also describes the overall culture process designed for the vascular chip.

Chapter 4 (Experimental Methods) outlines the fabrication process of the vessel-on-a-chip, describe vascular tissue culture methods and presents the analysis techniques employed in the research.

doi:10.6342/NTU202600103

Chapter 5 (Results), the structural parameters of generated vessels are analyzed depending on the culture methods viz., static, low flow and high flow conditions. Vascular remodeling is compared to the initial vessel structure. Finally, the evaluation of vascular functionality and results of disease modeling experiments are also presented.

Chapter 6 (Discussion) summarizes the key findings of the study, highlighting how the engineered arteriole-on-a-chip system replicates physiologically relevant vascular structure, remodeling, and functionality. The chapter also discusses the limitations of the current model and provides insights into how these findings advance our understanding of vascular biology and microfluidic engineering. Finally, it outlines perspectives for future research, including potential improvements, applications in disease modeling, and translational relevance in vascular research and drug testing.

Chapter 7 (Conclusion) This chapter concludes the dissertation by providing an overview of the development of the arteriole-on-a-chip models and the key findings associated with each research aim. It highlights the specific research gaps addressed throughout the work and explains how the outcomes advance the broader understanding of vessel-on-a-chip development.

Chapter 8 (Future Work) This chapter outlines perspectives for future research, including potential improvements, applications in disease modeling, and translational relevance in vascular research and drug testing.

doi:10.6342/NTU202600103

2. Background

2.1 Cardiovascular Network

The Cardiovascular network is a highly dynamic and intricately organized system responsible for the circulation of oxygen, nutrients and removing metabolic waste from cells. The system consists of the heart and blood vessels that continuously pump and deliver blood throughout the body. The vascular network is a complex, hierarchical system composed of arteries, veins and capillaries, each serving distinct physiological roles in circulation. Arteries are high-pressure resilient blood vessels that delivers oxygenated blood to the peripheral tissues from the heart, while veins bring the deoxygentated blood from the organs back to the heart. Capillaries are the smallest vessels that form a dense network and enables gas exchange, nutrient delivery and waste removal from the cellular level. Apart from this, MVNs consist mostly of arterioles, venules and capillaries that are critical for maintaining tissue homeostasis and are primary sites for angiogenesis and vascular remodeling. These vascular subtypes differ both in structure and cell types and have distinct mechanical properties that influence their physiological and pathological roles.

Except capillaries, a typical blood vessel is a tubular structure consisting of three concentric layers that provide support, motion and biochemical responsiveness (Figure 2-1). The inner most layer is called tunica intima, which is composed of endothelial cells that line the lumen and regulate barrier function. The middle layer is called tunica media and is composed of smooth muscle cells and elastic fibers that enable vasmotion in response to physiological stimuli. The outermost layer, called tunica adventitia, consists of fibroblasts and connective tissues that provide structural integrity to the structure and anchor the vessel to the surrounding tissues. Arteries have a thicker layer of muscle cells

doi:10.6342/NTU202600103

to withstand high pressure whereas veins have thinner layer and valves to prevent backflow. Capillaries have endothelial layer and basement membrane and do not have muscle cells to efficiently facilitate exchange of gases, nutrients and waste.

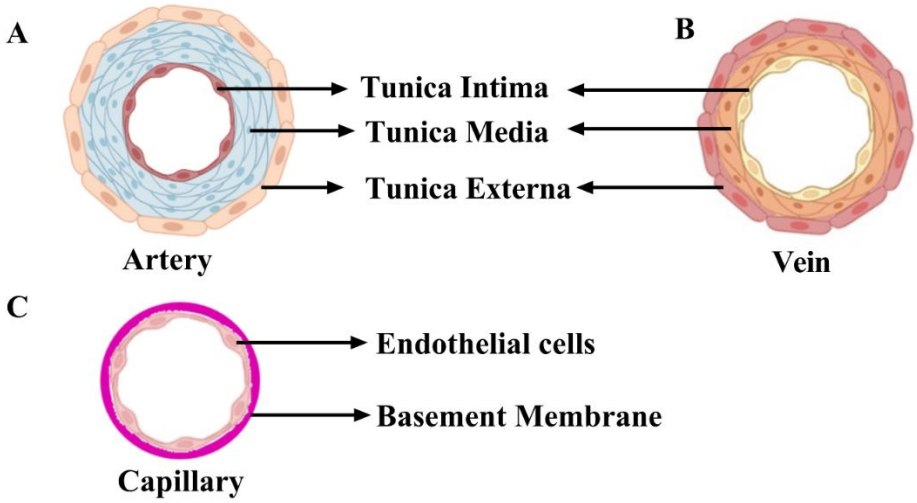

Figure 2-1 Schematic cross-sectional representation of (A) artery (B) vein (C) capillary. (Figure made using Biorender.com)

The vascular network is created through highly regulated biological processes that occur both during embryonic development and in adults under specific conditions. In the following section, we will describe the methods of blood vessel formation.

2.2 Methods of vessel formation

The blood vessels *in vitro* are created mostly by two processes vasculogenesis and angiogenesis. In the following sections we will briefly learn about their role in vessel development.

2.2.1 Vasculogenesis

Vasculogenesis is the *de novo* formation of blood vessels from endothelial progenitor cells, derived from the mesoderm, during embryogenesis. Briefly, mesodermal

doi:10.6342/NTU202600103

precursor cells differentiate into angioblasts i.e. endothelial progenitor cells [30]. These cells migrate to specific positions of the embryo and form blood clusters that further differentiate into endothelial cells and hematopoietic cells. These endothelial cells form the early capillary-like vessel structures known as primitive vascular plexus. Vascular endothelial growth factor (VEGF), fibroblast growth factor (FGF) and other proteins are key regulators of this process.

Although vasculogenesis is predominant during embryogenesis, adult tissues also undergo vasculogenesis during reparative conditions such as ischemic tissues, wound healing and tumor neovascularization. Vasculogenesis in adult tissues vary from embryogenic vasculogenesis in cell type, molecular mechanism and physiological condition [31]. In postnatal vasculogenesis, endothelial progenitor cells (EPCs) circulate in the blood and are recruited at the site of injury where they differentiate into endothelial cells and form new vascular structures [32]. Vasculogenesis is regulated by growth factors such as VEGF, angiopoietin and stromal cell derived factor -1 (SDF-1) [33].

Immature blood vessels are made of endothelial cells alone. Vessel maturation is the process of forming stable functional vessels by recruitment of mural cells (smooth muscle cells and pericytes), formation of the basement membrane and the organization of the vessel wall.[34], [35] Endothelial cells release platelet-derived growth factor-B (PDGF-B) which attracts PDGFR-beta receptor producing mural cells via chemotaxis[36], [37] A specialized extracellular matrix (ECM) structure known as basement membrane (BM) is formed between endothelial cells and the surrounding tissues and is important in regulating vessel function and stability.[38] BM is composed of laminin, collagen IV, nidogen and heparin sulfate proteoglycans that self-assemble under the endothelial cells and provide a scaffold for further cellular organization.[39], [40], [41]

doi:10.6342/NTU202600103

2.2.2 Angiogenesis

Angiogenesis is the formation of new blood vessels from existing blood vessels.[42] Critical in embryonic development, angiogenesis is also instrumental in wound healing, tissue regeneration and pathological processes such as tumor growth.[43], [44], [45], [46] It is a complex process involving controlled interplay of growth factors, receptors, signaling pathways and ECM remodeling. There are two types of angiogenesis: (i) sprouting angiogenesis (SA) and (ii) intussusceptive angiogenesis (IA) [47] . Following segments will explain both mechanisms in detail.

2.2.2.1 Sprouting Angiogenesis

In SA, ECs proliferate, migrate and form new vessels in the guidance of pro-angiogenic factors such as VEGF. The process begins when a hypoxic condition triggers release of VEGF which then binds to its receptor VEGFR-2 on endothelial cells.[48] The mature vessels are destabilized by reducing the interaction between ECs and mural cells. Ang2 binds to Tie2 receptors and detaches smooth muscle cells and loosens the ECM.[49], [50] This activates downstream signaling and initiates the degradation of basement membrane by secreting matrix mellaoproteinases (MMPs) and activates bFGF, VEGF and IGF-1 growth factors.[51] Endothelial cells exposed to higher levels of VEGF differentiate into tip cells characterized by higher levels of secretion of VEGFR-2 and delta-like ligand 4 (DLL4).[52] The DLL4 on tip cells binds to Notch receptors of neighboring ECs and promotes their differentiation into “stalk cells” which are more proliferative [53]. Stalk cells elongate the sprout, form the base for a new vessel and undergo tubulogenesis, forming the lumen of the new vessel [54]. As the vessel matures, mural cells migrate and stabilize the new vessel. Sprouting is the angiogenesis is the basis for vessel formation in most OoC models to generate MVNs.

doi:10.6342/NTU202600103

2.2.2.2 Intussusceptive angiogenesis

It is the process of forming new blood vessels by splitting existing blood vessels [55]. The process begins by the remodeling of the endothelial junction due to the overexpression of signals such as VEGF [56]. The endothelial cell junction becomes dynamic allowing localized invagination. Opposing EC walls from a capillary loop extend towards each other into the lumen and at the contact point, the endothelial membranes flatten and fuse together to create the transcapillary pillar [57]. Pericytes, myofibroblasts and ECM components like Collagen I and IV infiltrate the pillar, stabilizing it and gradually enlarging it [55]. As the pillar grows, the vessel lumen is split into two, thereby producing two vascular structures.

Studies have reported that the initial vessel network is formed by SA while vessel remodeling is taken over by IA [58], [59]. IA is reportedly more efficient than SA as there is no requirement for disruption of basement membrane [60], [61]. Also, in IA, the ECs don't need to proliferate, rather enlarge and flatten, which reduces the metabolic cost.[62] Due to this difference in mechanical properties of SA and IA, the genes involved in ECM remodeling are upregulated in SA and genes involved in endothelial morphology, such as neuropilin, midkine and restin, were upregulated in IA. Interestingly, IA is less dependent on VEGF than SA and have shown increased angiogenic activity during VEGF inhibition in experimental tumors [63], [64]. In fact other diseases like chronic inflammation [65] and COVID-19[66] have shown increased IA activity.

2.2.3 Arteriogenesis

Arteriogenesis is the process of enlarging pre-existing small arteries to become functional arteries, thereby restoring blood flow when a main artery is blocked [67]. Unlike angiogenesis, which focuses on creating new vessels, arteriogenesis focuses on

doi:10.6342/NTU202600103

the remodeling of the existing small arterioles in case of occlusion of larger vessels. The primary trigger for arteriogenesis is shear stress due to increased fluid velocity in the collateral arteries when the main vessel is occluded. The process involves multiple steps such as EC activation, basal membrane degradation, leukocyte invasion, proliferation of vascular cells, neointima formation, changes of the ECM and cytokine participation [68]. Elevated shear stress activates the ECs via mechanosensory complexes such as PECAM-1, VE-cadherin, VEGFR-2 and integrins. This triggers the upregulation of adhesion molecules, such as ICAM-1 and VCAM-1 and chemokines, including monocyte chemoattractant protein-1 (MCP-1). Monocytes attach to the activated ECs and then infiltrate the vessel wall, where they produce growth factors and proteases that initiate the remodeling process. Vascular cells proliferate inside the vessel wall creating a new layer within the vessel wall known as neointima [68]. Growth factors such as VEGF, FGF-2 and PDGF and cytokines such as TNF-α and IL-1β help in proliferation and creating an environment for wall remodeling.

In typical arteriogenesis process, SMCs play a prominent role as they are the key cells that undergo migration and proliferation, which stabilize and thicken the vessel wall. However, in our study, we also observed increased vessel diameter without SMC co-culture, suggesting capillary remodeling that remain arteriole-like but without the contractile properties of an actual artery. In future section, we will elaborate on this observation.

2.3 Intravascular flow

Intravascular flow refers to the flow within the blood vessels that determines the vascular health and function. The mechanical forces generated due to blood flow creates shear stress that has profound effect on vessel health. Shear stress is directly related to

doi:10.6342/NTU202600103

blood flow and viscosity and is inversely related to the third power of arterial radius.[69] Shear stress regulates a wide range of biophysical processes within blood vessels, including endothelial function, vascular tone, and disease progression. The ECs are the primary sensors and responders for changing shear stress. ECs have mechanosensors such as glycocalyx structures, integrins, ion channels, primary cilia and junctional proteins such as PECAM-, VE-cadherin that can sense the change in shear stress and convert them to intracellular signaling cascades.[70] Under laminar flow, ECs elongate and align in the direction of flow and enhances the expression of anti-inflammatory, anti-thrombotic and vasodilatory mediators such as nitric oxide (NO). The physiological range of wall shear stress (WSS) for bigger vessels ranges between 1-6 dyn/cm^2 in veinous systems, 10-70 dyn/cm^2 in arteries. For thinner vessels, the WSS varies from 20-40 dyn/cm^2 in venules to 60-80 dyn/cm^2 in arterioles. Average shear stress is lowest in larger veins (<1 dyn/cm^2) and highest in smaller arterioles (~ 80 dyn/cm^2).[71]

However, disturbed flow such as low, oscillatory or turbulent flow, induces multiple types of EC dysfunction. Increased pro-inflammatory phenotyope, such as upregulation of adhesion molecules (VCAM-1, ICAM-1), disruption of tight junctions and increased permeability, reduced NO availability and impaired vasomotion are some of the observable EC dysfunction [70]. Studies have also shown an association between abnormal shear stress changes and increased cardiovascular diseases such as atherosclerosis, aneurysms, thrombosis and microvascular disorders [72], [73], [74], [75]. Narrow arteries or bifurcations create disturbed blood flow that leads to low or oscillatory shear stress. This leads to the activation of pro-atherogenic gene expression and the ECs become susceptible to oxidative stress. The altered ECs promote the migration and adhesion of leukocytes to the vessel wall. Collectively, lipids and inflammatory cells accumulate in the vessel wall forming atherosclerotic plaque [76]. Conversely, in high

doi:10.6342/NTU202600103

shear stress (above 5000 s^{-1}) von Wilebrand Factor (vWF) elongates and captures platelets from the blood [77]. The rapid platelet adhesion on exposed collagen surfaces leads to life threatening occlusive thrombi formation that can lead to heart attack.

Apart from cellular health, shear stress is a major contributor to vessel remodeling. Studies have shown that under low shear stress, vessel diameter decreases, and under high shear stress (above physiological range), the diameter increases [78], [79]. In both conditions, EC expresses inflammatory genes to recruit leukocytes and decreases vessel stability. Other than vessel remodeling, shear stress also helps in remodeling the vascular network to promote network stabilization, pruning and maturation [80], [81]. In low shear stress mediated remodeling, the vessels prune and ECs migrate towards high flow areas. For high shear stress, diameter increases, thinner vessels become impermeable, and high flow vessels increase in diameter. Since intravascular flow is critical in vessel creation and stabilization, it is important to incorporate it in *in vitro* models to better understand the underlying mechanism and advancing therapeutic strategies.

2.4 Interstitial Flow

Interstitial flow refers to the movement of fluid through the ECM and interstitial spaces surrounding the cells and tissues. It is a specialized form of convection based mass transport driven by hydrostatic and osmotic pressure gradients between blood vessels, lymphatics and the surrounding tissue [82]. Although the velocity of interstitial flow is very low (0.1 – 0.5 μm/s), yet it plays a significant role in nutrient and waste transport, cell signaling and mechanotransduction, immune surveillance and tissue homeostasis [83]. Dysregulation of interstitial flow in the human body leads to disease progression, such as excess fluid accumulation (edema), fibrosis and cancer progression. [84] In cancer progression, increased intratumoral pressure creates a surge of flow that pushes the cancer

doi:10.6342/NTU202600103

cells from the tumor to the surrounding tissue, metastasizing cancer into distant sites [85]. Fluid flow also influences growth and proliferation of tumor cells, forming new blood vessels (vasculogenesis) and lymphatic vessels (lymphangiogenesis) within the tumor [86], [87]. Positively, interstitial flow can also be targeted for efficient drug delivery. The increased fluid flow can influence the transport of therapeutic drugs to the tumor sites, promoting better drug delivery.[85] Moreover, understanding the change in fluid flow could also serve as a potential marker in disease progression, leading to the development of new diagnostic tools or treatment strategies [88].

In the context of OoC, interstitial flow is replicated in the microfluidic chamber to supply nutrients, remove waste and provide other physiological cues that mimic the complex dynamics of the human organs [89], [90], [91]. The effect of interstitial flow has been studied extensively showcasing influence on influence angiogenesis[92], [93], vasculogenesis[94], [95], [96], lymphangiogenesis [97], [98] , tumor cell migration [99], [100], [101], myofibroblast differentiation [102] and embryogenesis [103], [104] in *in vitro* models. Control of interstitial flow is essential for vascular development, as it directs angiogenesis and microvascular organization. Understanding how different flow levels influence vessel formation is therefore key to assembling stable, physiologically relevant vascular networks that closely mimic in vivo architecture.

2.5 In vitro Models for Developing Vessel-on-a-chip

Many researchers have developed various methods for replicating human vasculature-on-a-chip. However, the process and methods are different depending on the type of developed vessel structures. Overall, the *in vitro* vessels are developed in majorly three ways: (i) patterned microchannel (ii) sacrificial 3D bioprinting (iii) self-assembly. In the following sections, we will describe each type briefly.

doi:10.6342/NTU202600103

2.5.1 Patterned microchannel

In this method, the design of the vasculature is created using soft lithography on a device and then the cells are seeded in the pattern with hydrogels to grow according to the design. Although the developed channels have rectangular cross section, this method is high-throughput with controlled mechanical and physical stimulus. Wang et al. developed cellulose-based microtubes using a chitosan template to engineer a tumor microenvironment that integrates blood vessels and tumor cells, enabling the modeling of tumor cell transvascular migration [105]. The developed transparent, elastic and porous artificial vessel structures mimicked the vessel wall. They proliferated HUVECs inside the tube to resemble vascular lumen and used this setup to investigate the interaction between tumor cells and the HUVECs. They observed that HGF promoted migration of the cancer cells (HCCLM9) to the cell wall and heightened interaction between ECs and tumor cells. This led to EC barrier dysfunction and eventually transvascular migration of the cancer cells depending on the HGF concentration.

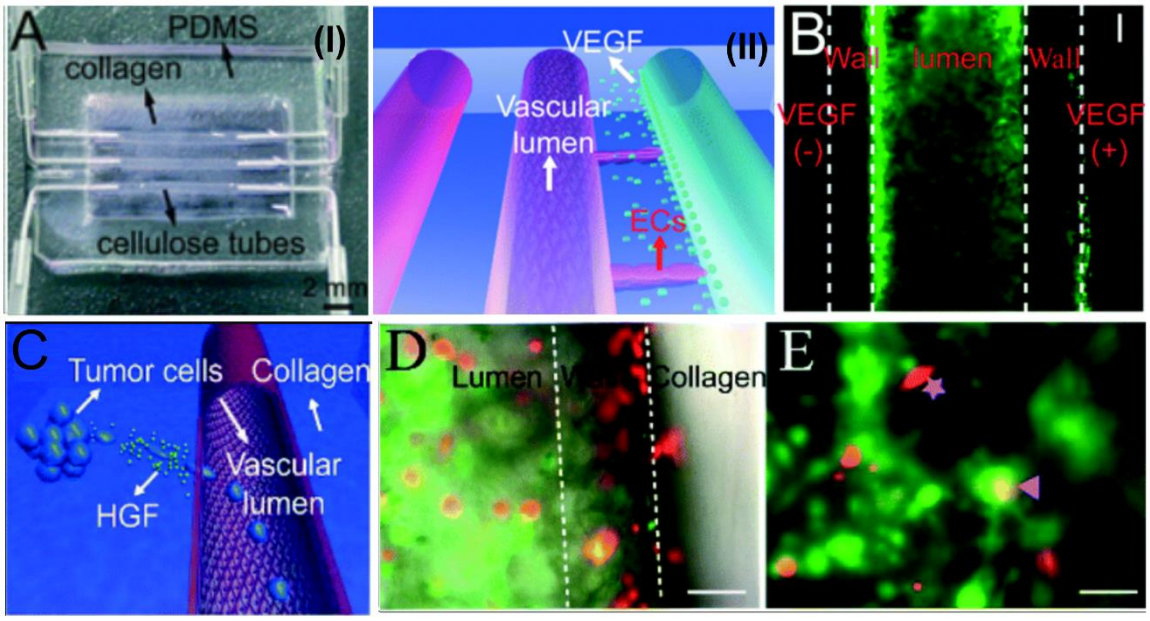

doi:10.6342/NTU202600103

Figure 2-2 (A) (I) Micrograph showing three cellulose/collagen artificial blood vessels embedded within a collagen matrix. (II) Diagram depicting endothelial cell migration induced by VEGF, along with microscopy images of HUVECs under VEGF-treated and untreated conditions (B) Diagram depicting HCCLM9 cell intravasation triggered by HGF. (C) Schematic representation of HCCLM9 cell intravasation in response to HGF. (D) Fluorescence image illustrating HCCLM9 cell behavior in response to HGF across the artificial blood vessel wall. (E) Fluorescence image showing the spatial distribution of HCCLM9 cells and HUVECs. (scale bar: 100 μm) [105]

Lamberti et al. designed an intricate bioinspired microfluidic assay (bMFA) for studying leukocyte-endothelium interaction [106]. They used AutoCAD to design the microfluidic network based on Geographic Information and System based mapping of MVNs obtained by intravital microscopy of rodent vasculature and fabricated the design on silicon wafers using SU-8 photoresist to obtain the master mold. Using soft lithography technique, the final substrate was obtained by polydimethylsiloxane (PDMS) curing and plasma bonding. HUVECs were cultured in the patterned channels until confluency and the setup was used to study the rolling, adhesion and migration behavior of neutrophils in the bMFA. They observed similar migration and adhesion pattern of leukocytes in bMFA as compared to *in vivo* models. The neutrophils adhered near to the bifurcation diameter and the adherence decreased with increased distance from the nearest bifurcation. Moreover, neutrophil adhesion was inversely related to shear stress, as observed in *in vivo* model as well.

doi:10.6342/NTU202600103

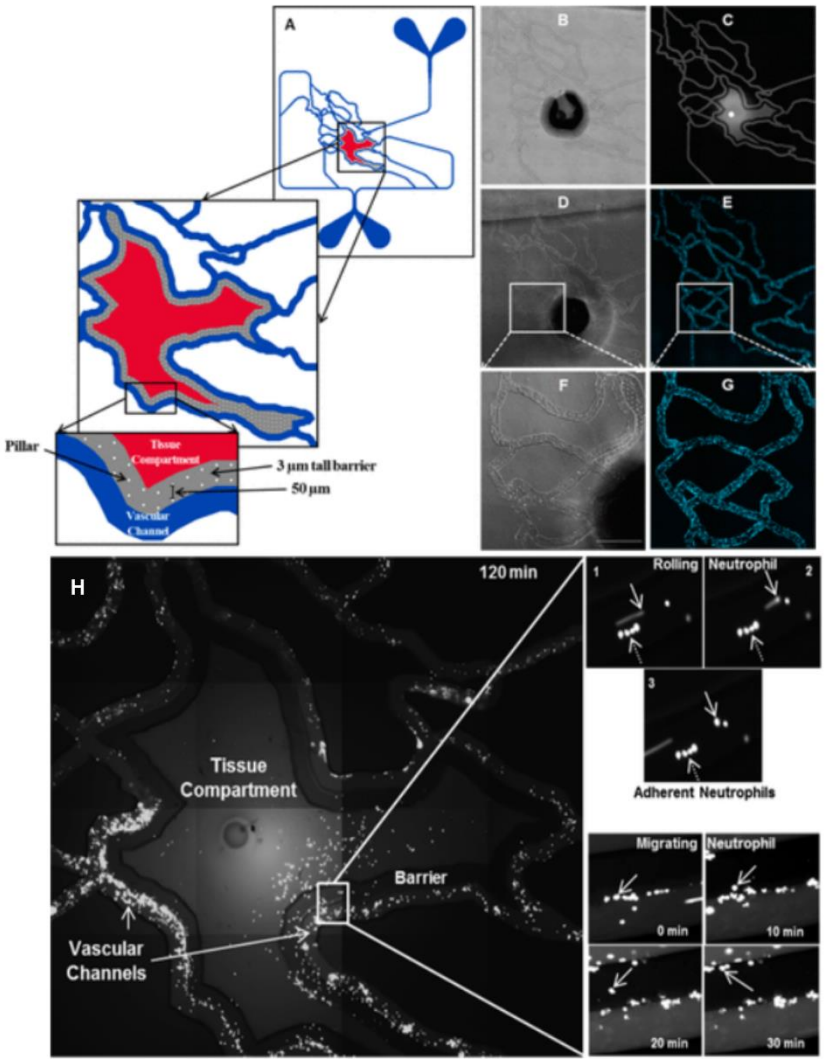

Figure 2-3 (A) Illustration of the bMFA architecture showing two vascular microchannels (100 μm wide and 100 μm high) flanking a central tissue chamber. The compartments are divided by a 100 μm wide porous barrier with a pore diameter of 3 μm. (B) Optical image of the fabricated bMFA device incorporating the 3 μm pore-size barrier. (C) Visualization of channel integrity and connectivity using FITC dye perfusion. (D) Phase-contrast image demonstrating a confluent endothelial monolayer within the vascular channels, with cells aligned along the direction of fluid flow. (E) Endothelial cell viability within the bMFA, confirmed by Hoechst nuclear staining. (F–G) Higher-magnification views of endothelial cells under phase-contrast and fluorescence microscopy (scale bar: 500 μm). Dark regions visible in panels (B) and (D), as well as the intense fluorescent spot in panel (C),

doi:10.6342/NTU202600103

correspond to the tubing used to connect the tissue compartment to the syringe pump. (H) Neutrophil dynamics within the bMFA, including rolling, firm adhesion, and transmigration. Fluorescently labeled neutrophils are shown entering the tissue compartment after 120 minutes of continuous perfusion. In the upper right panels, solid arrows indicate a rolling neutrophil that subsequently becomes adherent, while dashed arrows denote firmly attached neutrophils. The lower right panel illustrates the stepwise migration of a neutrophil from the vascular channel across the porous barrier into the tissue compartment over time. [106]

2.5.2 Sacrificial molds

In this method, the spaces for the microfluidic structures are filled with temporary molds and are removed just before cell seeding. Using this technique, cylindrical microchannels can be created and can facilitate co-culture of multiple cells around the channels. However, the reproducibility and resolution can be lower than that of patterned microchannels [107]. Ngyuen et al. fabricated hollow cylindrical channels surrounded by collagen matrices in patterned PDMS layers for the study of angiogenic sprouting morphogenesis [108]. First, acupuncture needles were inserted in the PDMS grooves and then rat tail collagen type 1 was pipetted into the chamber and allowed for polymerization at 37ºC for 30 mins. After polymerization, the needles were removed to create two hollow channels. HUVECs were seeded into one channel, while pro-angiogenic factors were introduced into the opposite channel. The devices were then gently rocked to establish gravity-driven flow. Using this setup, they observed two combinations i.e. (i) HGF, bFGF, MCP-1, VEGF and S1P (HFMVS) and (ii) MCP-1, VEGF, PMA and S1P (MVPS) induced significant multicellular sprout like structures. They also observed S1P and PMA induced significant matrix invasion towards the source channel. This model recapitulates

doi:10.6342/NTU202600103

typical morphogenic sequences seen *in vivo* such as tip cell formation, stalk cell proliferation and elongation behind the tip, lumen formation and branching.

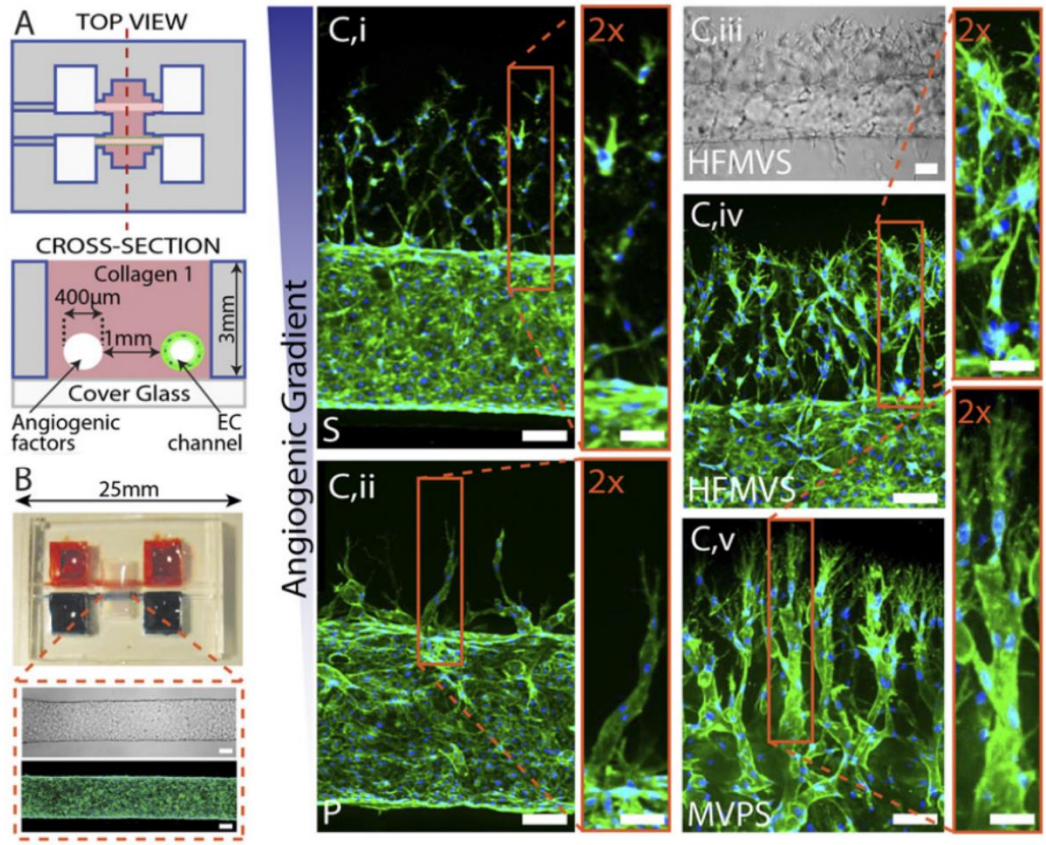

Figure 2-4 (A) Schematic diagram of device design (B) (A) Image of the fabricated microfluidic device. Enlarged views display phase-contrast (top) and fluorescence (bottom) images of a vascular channel lined with endothelial cells. The actin cytoskeleton and cell nuclei are visualized using phalloidin (green) and DAPI (blue), respectively. (C) Representative confocal immunofluorescence images illustrating endothelial cell sprouting and migration in response to gradients of distinct pro-angiogenic stimuli. Conditions include S (i), P (ii), HFMVS cocktail (iv), and MVPS cocktail (v). Panel (iii) presents a phase-contrast image showing directional sprouting triggered by the HFMVS cocktail. [108]

doi:10.6342/NTU202600103

Buchanan et al. created 3D microfluidic tumor vascular model to study the effect of WSS in endothelial barrier function and tumor-endothelial paracrine signaling [109]. The device is created by injecting collagen mixed with tumor cells (MDA-MB-231) into FEP tubing fit with a needle, with PDMS sleeves. After gelation, the needle is removed to create a hollow lumen and telomerase-immortalized human microvascular endothelial cell line (TIME) is cultured inside it until confluency to replicate the co-culture of ECs with tumor cells. They observed that HSS (10 dyn/cm^2) significantly reduced the endothelial barrier permeability in both endothelial mono-cultures and co-culture with tumor cells. Also, HSS significantly down regulated angiogenic and hypoxia associated genes such as MMP9, HIF1, VEGFA, ANG1, ANG2 in co-culture system but not in tumor mono-cultures or in conditioned media experiments without ECs.

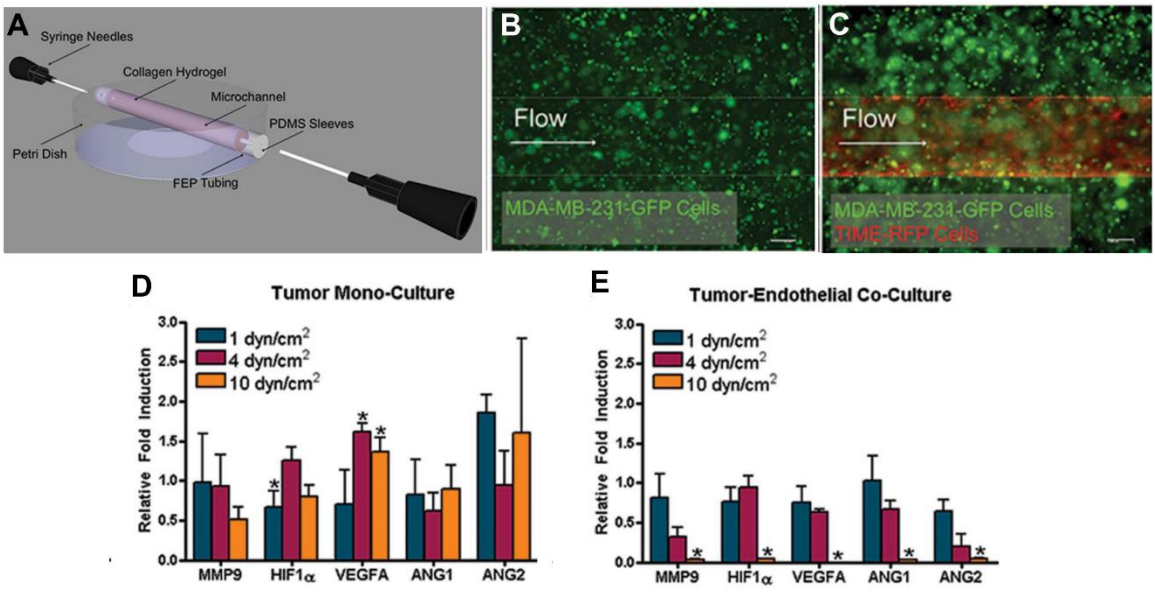

Figure 2-5 (A) Schematic of microfluidic tumor vascular model for 3D culture of tumor and endothelial cells under flow conditions. (B) Tumor mono-cultures and (C) co-cultures with endothelial cells for 72 hrs post which target WSS (tW D 1, 4, or 10 dyn/cm2) was introduced through the microchannel for a total 6 hrs. Total tumor mRNA was then

doi:10.6342/NTU202600103

isolated for gene expression analysis. Relative mRNA to GAPDH mRNA expressed as a fold induction § standard deviation. [109]

2.5.3 Self-Assembly

Although previous models mimicked the vascular structures, however they were artificially created with single cell types. To accurately replicate blood vessels, it is essential to develop miniaturized vessels incorporating the various cell types present in native vasculature. Consequently, many researchers have employed *in vivo* self-assembly methods to develop functional blood vessels directly from human cells. The major steps in generating these structures are vasculogenesis and angiogenesis [110]. On-chip vasculogenesis depends on ECM composition, angiogenic factors such as VEGF and bFGF, and co-culture of endothelial cells with supporting stromal cells. Hsu et al. demonstrated the role of physiological mass transport in inducing vasculogenesis on chip [95]. They mixed endothelial colony forming cell-derived endothelial cells (ECFC-ECs) and normal lung human fibroblast (NHLFs) in a fibrin gel and cultured in a 3D tissue chamber connected to a microfluidic platform capable of controlling mass transport. The control parameter was the Péclet number (Pe), defined as the ratio of convective to diffusive transport. Their platform generated Pe values ranging from 0.0056 to 160, enabling diffusion-dominated ($Pe < 1$), intermediate ($Pe \sim 1$), and convection-dominated ($Pe > 1$) mass transport regimes. They showed that vasculogenesis can be independently induced by either interstitial flow ($Pe > 10$) or hypoxic condition ($Pe < 0.1$). However, in intermediate regime vasculogenesis couldn’t be observed.

doi:10.6342/NTU202600103

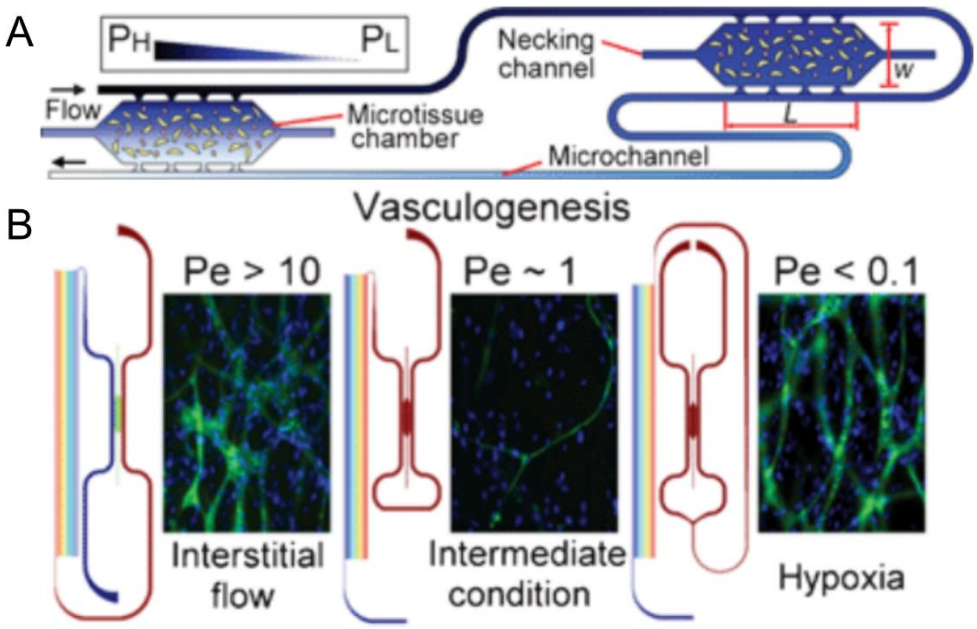

Figure 2-6 Schematic illustration of the use of a long microchannel to control the physiological environment in a microtissue chamber (B) Generation of vessels in different mass transport conditions. [95]

Kim et al. used both vasculogenesis and angiogenesis to create perfusable 3D microvascular or tumor vascular networks based on the co-culture of HUVECs with either lung fibroblasts (LFs) or cancer cells [111]. The devices consisted of five channels: (i) central chamber for culturing HUVECs (ii) two inner side channels for culture media and (iii) two outer side channels for culturing LFs. This setup enabled diffusion-based, contact-independent cell–cell communication, supporting the progression of both vasculogenesis and angiogenesis. To induce vaculogenesis, HUVECs were cultured in the central chamber and LFs were cultured in the outer side channels. Within 4 days, HUVECs produced perfusable vascular plexus using the pro-angiogenic factors secreted by the LFs. To induce angiogenesis, HUVECs were cultured in the left wall adjacent to the central chamber filled with fibrin matrix and LFs were cultured in the opposite outer

doi:10.6342/NTU202600103

wall to expose the ECs to a gradient of LF-secreted factors. They observed sprouting within 24 hrs of co-culture where the tip cells guided the stalk cells towards the LF gradient across the fibrin matrix. By Day 4, the tip cells reached the flanking medium channels, lost their filopodia and formed lumenized vessel structures to form perfusable networks. To verify the role of tumor cells in angiogenesis, they also co-cultured HUVECs with highly malignant human glioblastoma multiforme cells (U87MG) in the outer right channel. Within 24 hrs, HUVECs extended into fibrin matrix, similar to LF-induced angiogenesis, in response to U87MG-derived factors. However, the sprouts showed immature tubules with multiple tip cells and fused with adjacent vessels, resembling well known tumor-derived vasculatures *in vivo*.

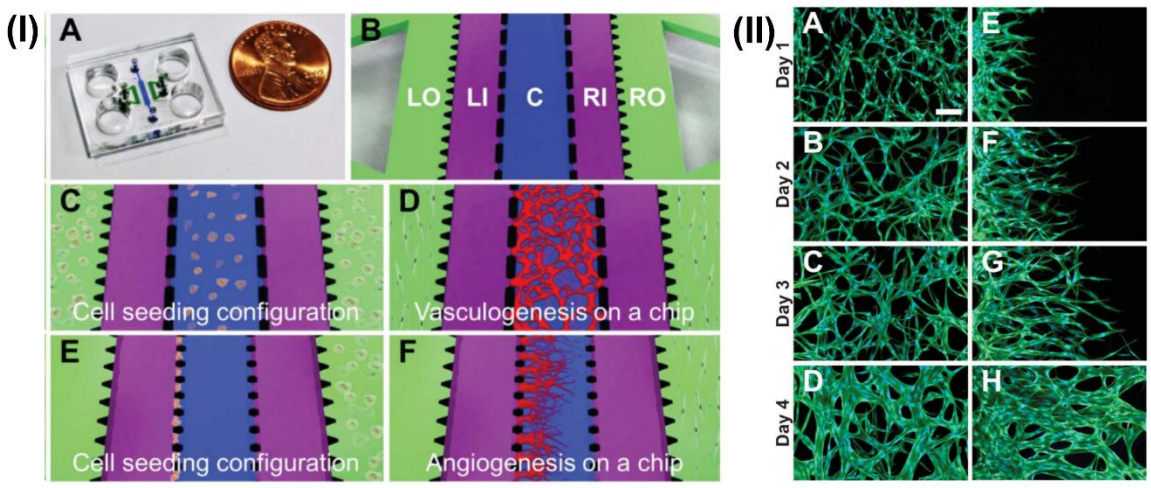

Figure 2-7 (I) Microfluidic chip design and cell seeding configurations for developing microvascular network via vasculogenesis and angiogenesis (II) Time-series micrographs of vasculogenic and angiogenic vessel formation in the fibrin matrix (A-D) Vasculogenesis (E-H) Angiogenesis (Scale bar = 100 μm)

Campisi et al. developed human blood-brain barrier (BBB) in a simpler microfluidic chip using vasculogenesis and angiogenesis [112]. They co-cultured human induced pluripotent stem cell derived endothelial cells (iPSC-ECs), astrocytes (ACs) and

doi:10.6342/NTU202600103

pericytes (PCs) in fibrin gel in the central chamber of a three-channel microfluidic device to induce vasculogenesis (Figure 2-8 (A-B)). A dense monolayer of iPSC-ECs was seeded on one side channel on Day 2 and the other side channel on Day 3 to promote angiogenesis. On Day 7, they observed the formation of highly interconnected μVNs (Figure 2-8 C). They compared several ECM markers secreted in tri-culture system with co-culture (iPSC-EC+PC) and monoculture (iPSC-EC) systems. The tri-culture system resulted in better biologically relevant networks with smaller diameters, more circular cross-sections more intricate patterns. It also showed higher expression of tight junction proteins (ZO-1, occluding and claudin), better deposition of basement membrane, upregulation of BBB transporter genes (P-GP,MRP1, MRP4,GLUT-1, LAT-1).

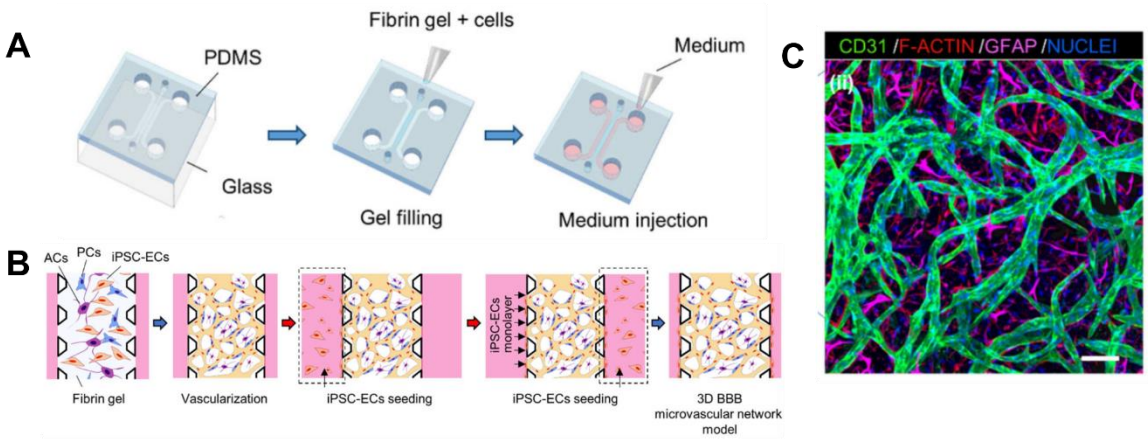

Figure 2-8 Blood brain barrier (BBB) in vitro (A) chip design (B) experiment protocol (C) confocal image of developed microvasculature [112]

2.5.4 In vitro arterial models

Most vessel-on-a-chip (VoC) research have employed HUVECs or iPSC-derived endothelial cells to generate venule- and capillary-like structures. However, studies focusing on the development of artery- or arteriole-like on-a-chip (AoC) models remain limited. In a primary work of AoC, Gunther et al. isolated mouse mesenteric artery

doi:10.6342/NTU202600103

segments and fixed it reversibly in a temperature controlled microfluidic environment to maintain physiological temperature and pressure of 37º C and 45 mmHg (Figure 2-9 (A-B)) [113]. Application of sub-atmospheric pressure immobilized the arteries and separated the luminal and abluminal fluid streams. They used this set up to test the dose-dependent response of phenylephrine and acetylcholine to observe their effect on vasomotion (Figure 2-9 (C-D)).

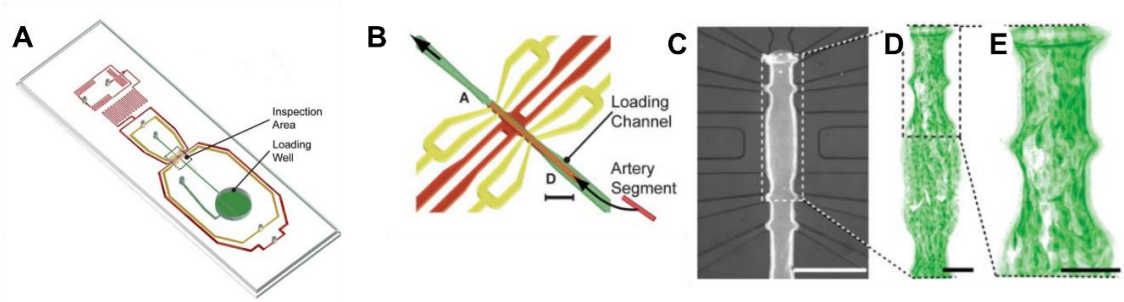

Figure 2-9 (A) AoC chip design. (B) Illustration of loading, fixation and perfusion (C) fluorescent micrograph of artery segment (D) confocal images of GFP-expressing ECs in the inspection section and (E) a segment of the artery [113]

Engeland et al. developed an intimal-medial unit like structure using human aortic endothelial cells (HaECs) and human human aortic vascular smooth muscle cells (VSMCs) to study cell-cell cross talk in hemodynamic conditions [114]. The authors built a microfluidic co-culture chip comprising of two parallel PDMS channels separated by a flexible porous PDMS membrane that mimics the internal elastic lamina separating endothelium and smooth muscle layer *in vivo*. On both sides of the culture channels, there are vacuum channels. When cyclic suction is applied, these channels stretch and relax the membrane, which in turn applies cyclic strain to the cells on culture channels. HaECs and VSMCs were cultured on opposite sides of the membrane and culture medium was flown through the EC side to mimic blood flow mediated shear stress. Using this setup, the

doi:10.6342/NTU202600103

devices generated a shear stress of ~ 1 – 1.5 Pa. They used this set up to study the cellular alignment in different hemodynamic forces, gene expression and HaEC-VSMC signaling in healthy and pathological conditions.

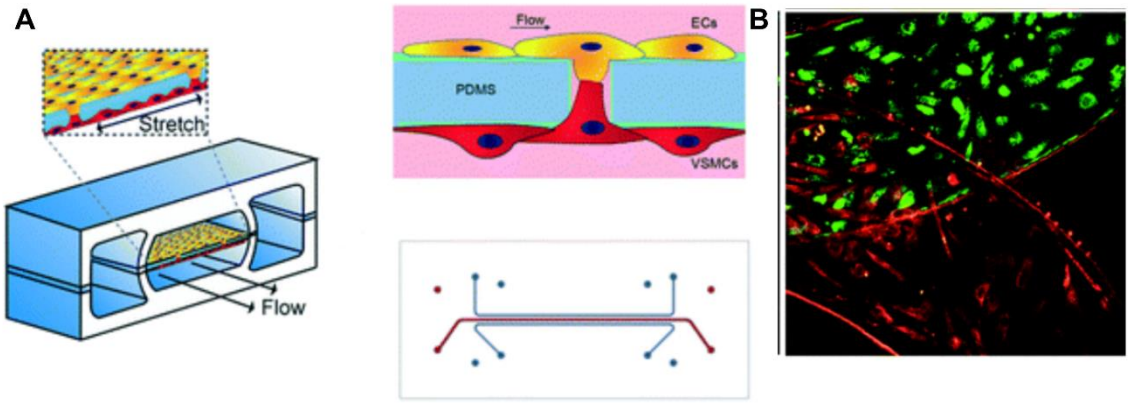

Figure 2-10 (A) Device design for developing intimal-medial unit like structure.(B) HaEC (green) and VSMC (red) co-culture [114]

Cuenca et al. developed a self-assembled VoC model using hiPSC-based cells [115]. They co-cultured hiPSC-ECs and different mural cells such as human brain vascular smooth muscle cells (HBVSMC), vascular smooth muscle cells (VSMC) and primary human brain vascular pericytes (HBVPs). The ECs formed a confluent and functional layer and SMCs provided the contractile ability with reasonable barrier and permeability properties. They characterized the vessel parameters among all models and assessed structural, molecular and functional markers. For functionality assay, they measured intracellular Ca^{2+} release (hallmark of VSMC contractility) by measuring GCaMP6f fluorescence intensity in response to vasoconstrictor (Endothelin-1) and vasodilator (Carbachol).

doi:10.6342/NTU202600103

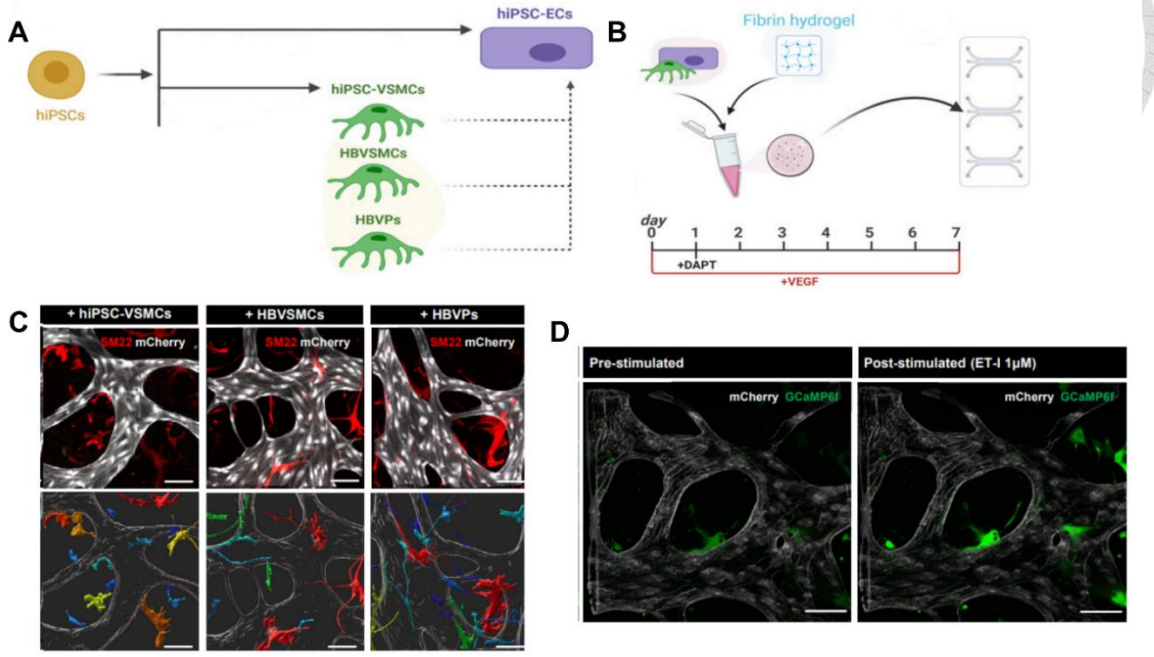

Figure 2-11 (A-B) Experimental protocol for developing self assembled VoC using hiPSC-based cells. (C) Confocal images showing ECs and mural cells co-localization. (D) Intracellular Ca^{2+} before and after stimulation with endothelin-1

2.5.5 Vascular disease models on a chip

Vascular diseases have been historically tested in rat models. However, with advancement in VoC, many researchers have designed microfluidic models for developing vascular diseases chips to further the understanding of disease mechanisms.

Su et al. developed an arterial wall-on-a-chip to understand EC-SMC cross talk and the phenotypic switching of SMC from quiescent to migratory state during atherosclerosis that contributes to the intima thickening [116]. Their device is made of four parallel straight channels that reconstituted the arterial intima-media interface. Human aortic ECs and human aortic SMCs were co-cultured so that ECs faced the luminal side and ECs and SMCs sandwiched a “cell-free” hydrogel channel that served as sub-endothelial ECM layer. They observed that when the sub-endothelial layer (subE) had a

doi:10.6342/NTU202600103

composition of 20% collagen and 80% matrigel, the SMCs remained quiescent and aligned, characterizing healthy arterial SMCs. When the EC layer was stimulated with pro-inflammatory cytokines (IL-1β, TNFα) and oxidized LDL (oxLDL), ECs showed elevated ICAM-1 expression demonstrating endothelial inflammation. In this condition, SMCs started migrating towards the luminal side via ECM, mimicking the early medial-to-intima migration observed in atherogenesis. The inflamed EC layer also promoted monocyte adhesion. Upon treatment with anti-atherogenic agents like vitamin D and metformin, cytokine induced monocyte adhesion to the ECs and SMC migration reduced significantly, confirming the atheroprotective effects of both drugs.

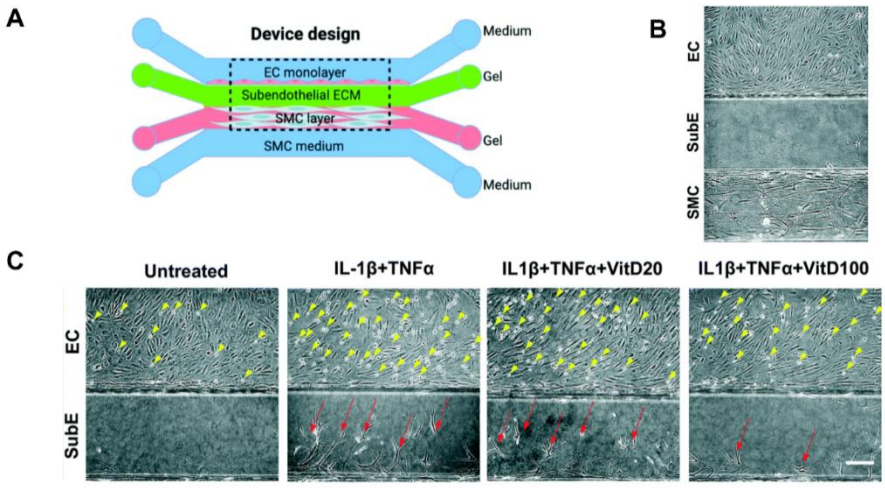

Figure 2-12 (A-B) Device design for developing arterial wall-on-a-chip (C) ECs, sub-endothelilal (subE) layer and SMCs in quiescent stage (C) Migration of SMCs to the subE layer in untreated, inflamed and treatment with various dosage of vitamin D [116]

Zheng et al. designed patterned microfluidic vessels to study the effect of inflammatory response in developing thrombosis [117]. In this study, they fabricated MVNs within type 1 collagen by molding microstructures using injection-molding technique. HUVECs were cultured in the walls and human brain vascular pericytes (HBVPCs) or HUASMCs were cultured in the collagen bulk to form vessel like conduits

doi:10.6342/NTU202600103

embedded in collagen scaffold. The ECs in these artificial-vessel like structures were able to sprout into the surrounding matrix in response to angiogenic stimulation. To test the functionality of these vessels, they developed a thrombosis model. In quiescent conditions, the ECs in the engineered vessels restricted platelets adhesion and clot formation when perfused with whole blood. However, when the vessels were stimulated with phorbol 12-myristate 13-acetate (PMA), the ECs were inflamed and von Wilebrand factor (vWF) was released. vWF is a glycoprotein that plays a key role in blood clotting and thrombosis [21], [22], [23]. Upon flowing blood over the inflamed ECs, platelet adhesion rate increased significantly, resulting in the formation of thrombus.

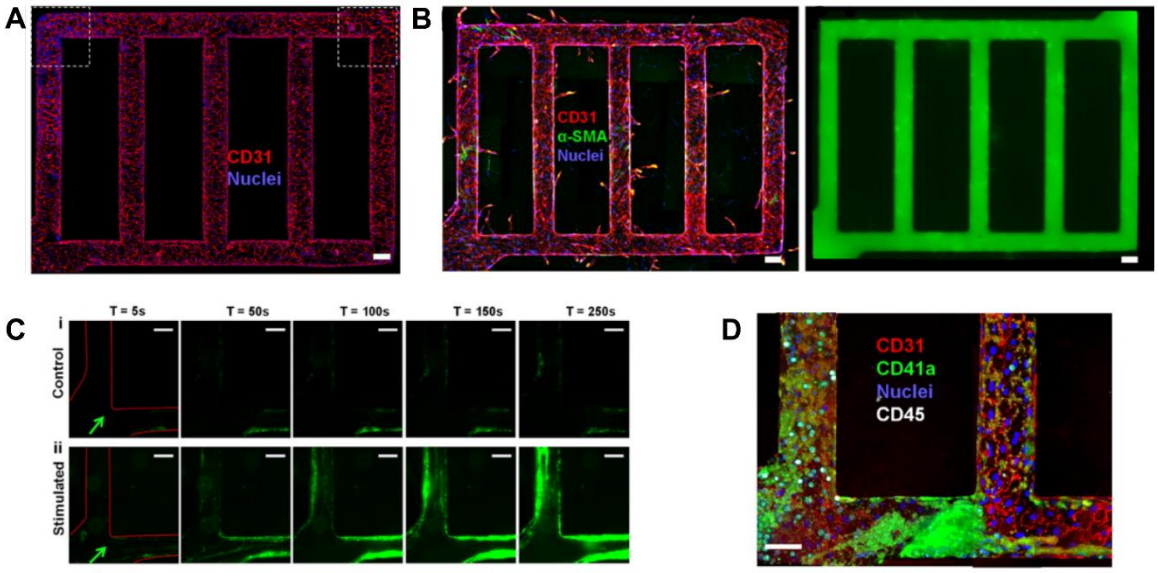

Figure 2-13 (A) Patterned MVNs with HUVECs cultured to confluence (B) angiogenic sprouting into the collagen matrix in response to angiogenic stimulation (C) platelet adhesion in control vs stimulated MVNs with PMA (D) Platelets and leucocytes adherent in the stimulated vessels after 1 hour of blood perfusion

doi:10.6342/NTU202600103

Zhang et al. demonstrated both thrombosis and thrombolysis in their bioprinted thrombosis-on-a-chip model [118]. They created microchannels using sacrificial biorinting and coated a confluent layer of HUVECs mixed with gelatin methacryloyl (GelMA). To induce thrombosis, they added 10 vol.% 0.1M $CaCl_2$ to whole human blood and injected into the microchannels. $CaCl_2$ acted as a thrombus agent and formed fibrin-rich clots within 10 mins of perfusion. Upon perfusion with tissue plasminogen activator (tPA), the authors observed dissolution of thrombi formed after day 1 and day 7. They also demonstrated that tPA becomes ineffective under thrombus fibrosis conditions — a chronic stage in which blood clots transform into fibrotic tissue through the deposition of collagen and other extracellular matrix proteins by fibroblasts.

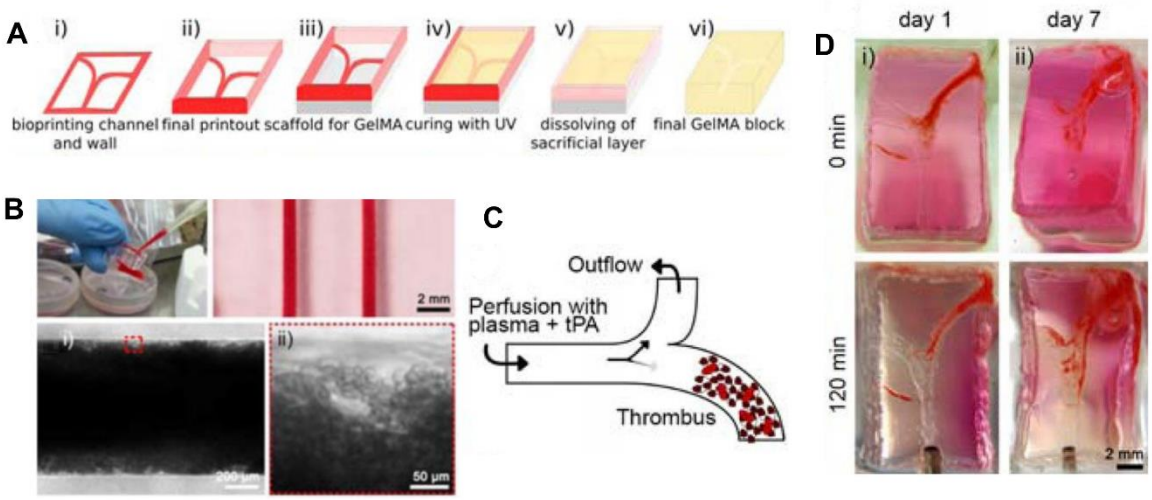

Figure 2-14 (A) Schematic representation of device fabrication (B) Blood flow and thrombus formation (C) schematic representation of tPA thrombolysis study (D) time-lapse photographs showing thrombolysis of 1-day clot and 7-day clot [118].

Other than atherosclerosis and thrombosis, other vascular diseases have also been studied in OoC platforms such as inflammation, ischemia-reperfusion, microcirculatory

doi:10.6342/NTU202600103

obstruction and hematologic disorders in malaria etc. Shakeri et al. did a detailed review on these studies [119].

2.6 Study of flow and arteriogenesis on a chip

Fluid circulation within an OoC model is important for recreating dynamic physiological environment that cells experience in the body. In the context of vascular biology, this continuous circulation is important to regulate multiple *in vivo* phenotypes such as cell alignment, barrier integrity, gene expression and anti-inflammatory functions [120]. To promote continuous, gravity driven flow in a single direction, Wang et al. designed UniChip [121]. This pump-less design converts reciprocating gravity-driven flows into continuous unidirectional perfusion with a backflow-proof mechanism that ensures unidirectional flow through the tissue chamber. The device design consists of a cell perfusion channel (C_u), two open access reservoirs and supporting channels (a_1, a_2, b_1 and b_2) and two supporting valves (v_1 and v_2). They experimentally verified that when the device is tilted on a rocking platform at an angle of ± 18º, the flow through C_u is always in a single direction. The valves halt the backflow in channels b1 and b2 if the elevation difference between two reservoirs does not exceed the capillary rise (h).

They cultured HUVECs in Unichip condition and compared their morphology with Bichip (reversing flow) to analyze shear stress sensitivity in long-term dynamic culture. The cells were cultured for 5 days with a shear stress magnitude of 5.3 dyne/cm^2. ECs cultured in Unichip showed elongation and alignment in the direction of flow, mimicking tissue morphology under laminar flow. However, ECs in BiChip showed no oriental preference, mimicking cell cultured in static condition.

doi:10.6342/NTU202600103

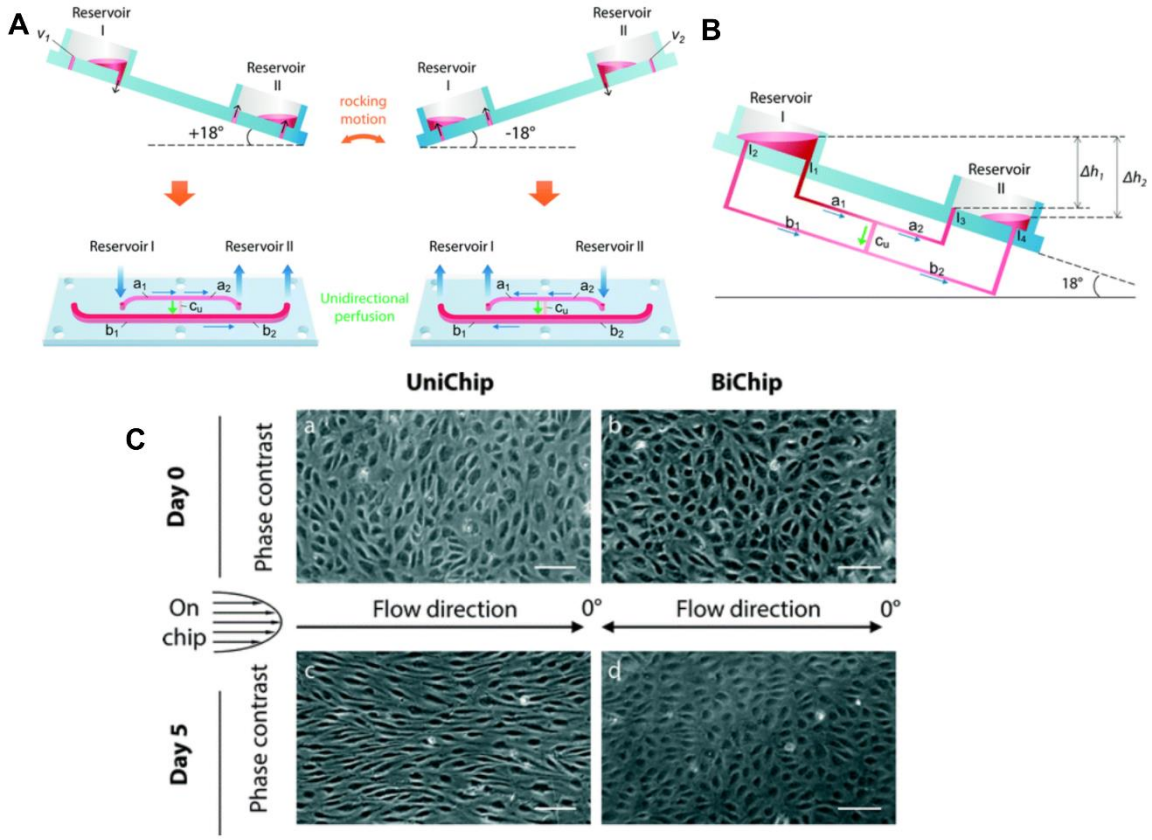

Figure 2-15 (A) Schematic representation of flow in UniChip during rocking motion (B) Schematic illustration of fluid channel network structure and connections among different channels in UniChip device (C) Comparision between cell response to UniChip and BiChip perfusion on Day 0 and Day 5 of culture [121]

To evaluate the effect of unidirectional and bidirectional flow in “artery”, Ehlers et al. used OrganoPlate 2-lane-48 UF microfluidic device [122]. They custom-made the 48-microfluidic chip based device to create unidirectional flow and used the commercially available titer plate for bidirectional flow when flow is induced by gravity through reciprocal rocking. Each chip consists of an ECM channel, a perfusion channel and a bypass channel. The vessel structures were created by either monoculture of human coronary artery ECs (HCAECs) or co-culture of HCAECs and human coronary artery smooth muscle cells (HCASMCs). Under unidirectional flow, they observed EC

doi:10.6342/NTU202600103

alignment along the flow direction, reduced fibronectin deposition and non-contractile SMC phenotype, resembling healthy arterial condition. However, under bi-directional flow, the vessels showed markers of early EC dysfunction with polygonal vessel morphology, increased fibronectin secretion, higher ICAM-1 staining and lipid accumulation, suggesting of atherogenic changes. However, the shear stress generated was only 3.7 dyne/cm^2, lower than actual arterial shear stress.

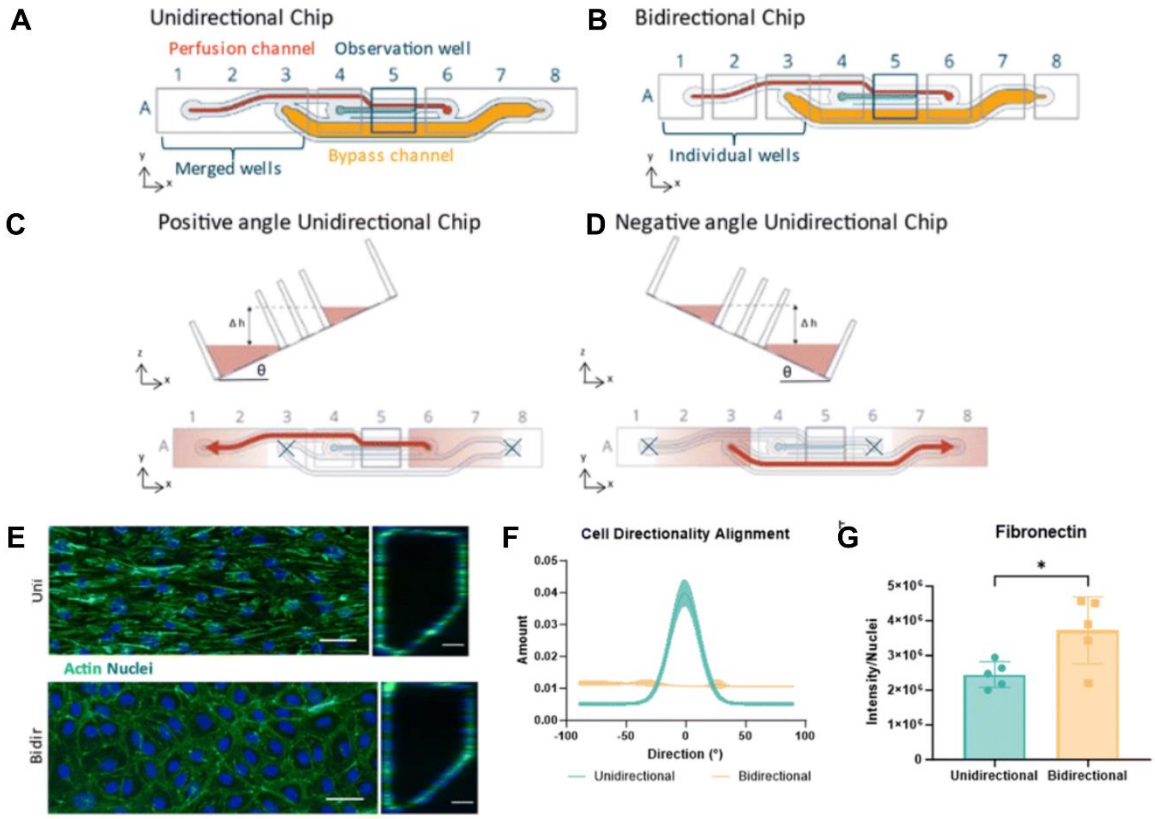

Figure 2-16 Schematic representation of (A) unidirectional chip and (B) bidirectional chip. Illustration of (C) positive angle perfusion (D) Negative angle perfusion in unidirectional chip. (E) Cell morphology in unidirectional and bidirectional culture condition. Comparison of (E) cell directional alignment and (F) fibronectin secretion in unidirectional and bidirectional conditions [122]

doi:10.6342/NTU202600103

Shafiyi et al. studied the relation between blood flow and vascular remodeling under long-term perfusion in low and high VEGF conditions [123]. They used a 5 channel microfluidic chip where the HUVECs were cultured in the central chamber and media was perfused on either side by micro-posts. Human pulmonary fibroblasts (HPFs) were cultured in the outer chambers and the secreted VEGF facilitated open lumen formation on-chip. By day 8, 3D MVNs were formed through vasculogenesis. Perfusion was established through the networks by using low-pressure pump systems from day 9 to day 12. For the static condition, they cultured the devices without flow. At low VEGF levels i.e., healthy models, vascular remodeling occurred according to animal models. Vascular remodeling occurred to increase flow via pruning and vessel hierarchy. However, in static condition, vessel grew continuously without pruning or optimization of network. Under tumor-mimicking high VEGF condition, under flow aberrant overgrowth of vessels was observed with inefficient pruning and unimproved flow velocities. They also observed that the anti-VEGF drug bevacizumab was efficient in high VEGF + flow condition to normalize network if low VEGF and flow was present. However, in static culture or low VEGF conditions, bevacizumab was not as efficient.

doi:10.6342/NTU202600103

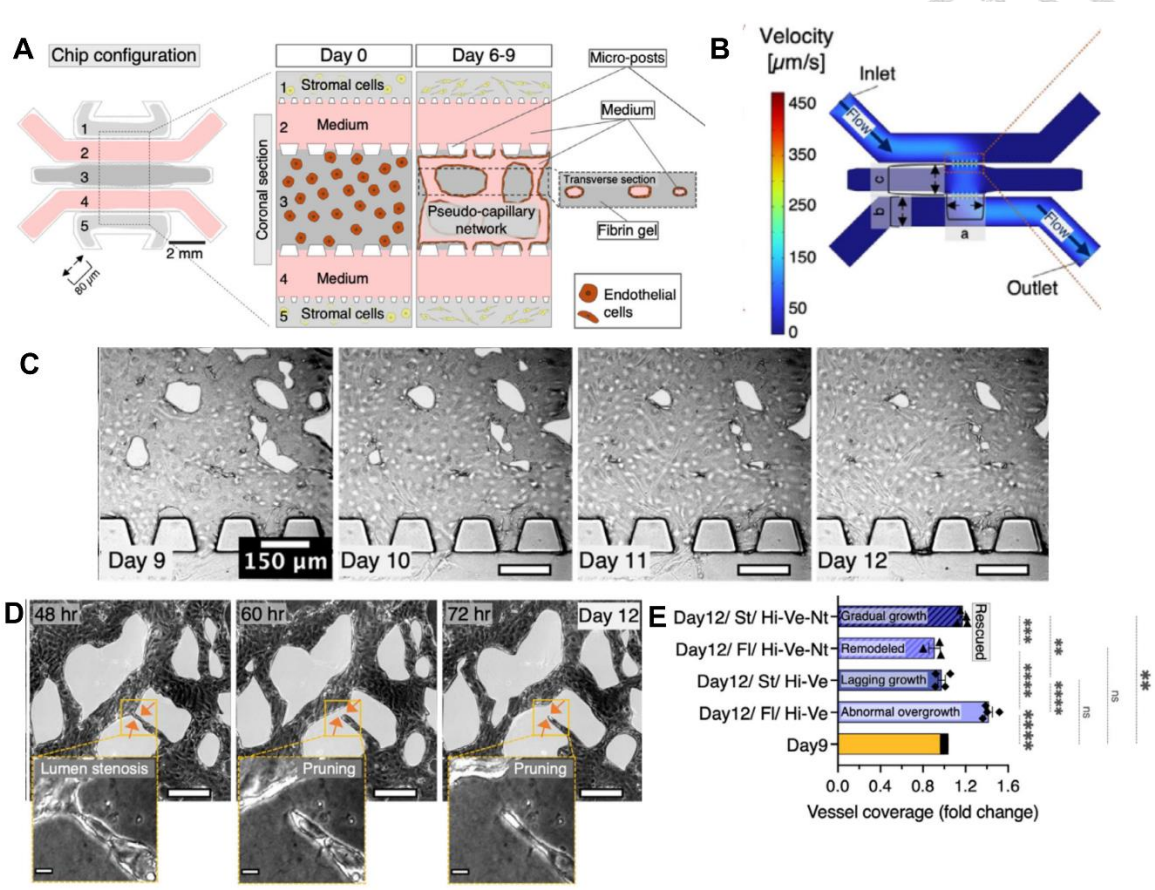

Figure 2-17 (A) Design of the microfluidic chip and experimental setup (B) Flow-velocity simulation of the empty device, illustrating velocity distributions across the openings. (C) Bright-field image of static vascular networks demonstrating progressive vessel development. (D) Bright-field image of a flow-conditioned vascular network, with enlarged views highlighting lumen narrowing and pruning-branch disruption. (E) Vessel coverage quantified as area density in day-12 networks under high-VEGF (Hi-Ve) and high-VEGF plus bevacizumab (Hi-Ve-Nt) conditions, for both flow-conditioned (Fl) and static (St) cultures, expressed as fold changes relative to day-9 measurements.

doi:10.6342/NTU202600103

3. Design Concept of Microfluidic Devices

3.1 Design Principles for developing Arteriole-on-a-chip devices

3.1.1 Microfluidic design principle concepts

To design a microfluidic device that recapitulates *in vivo* mechanisms, understanding the fluid flow inside the micro-chamber and the microfluidic network is crucial. However, as the network becomes more complex, interpreting the fluid movement inside the microfluidic network becomes challenging. Furthermore, the design of such microfluidic networks requires specialization in computational fluid dynamic (CFD) based software, which is expensive and needs trained experts in the field. Hence, a simplified understanding of fluid motion within the microfluidic networks is required to intuitively visualize the flow behavior inside the micro-chamber. One way to achieve this is by using a real-world analogy that explains how pressure drop, flow resistance, and flow rate behave inside these devices. Such an analogy can make it easier to predict fluid motion without relying entirely on complex CFD tools.

Hagen-Poiseuille law describes the pressure-driven laminar flow in a long, cylindrical tube for a Newtonian, incompressible and laminar flow fluid [124]. A similar analogy to this in electric circuit is Ohm's law, which describes the movement of current through materials at a constant temperature and resistance [125]. Figure 3-1 shows schematic representations of the application of Hagen-Poiseuille's law and Ohm's law. The impedance created when a fluid flows inside a microfluidic wafer is similar to the impedance created by the flow of current through a wire. Just as electrical impedance in a circuit depends on the conductor's cross-sectional area and length, the hydraulic resistance (impedance) in a microfluidic channel is also governed by its geometry, such as the channel's cross-sectional dimensions and length.

doi:10.6342/NTU202600103

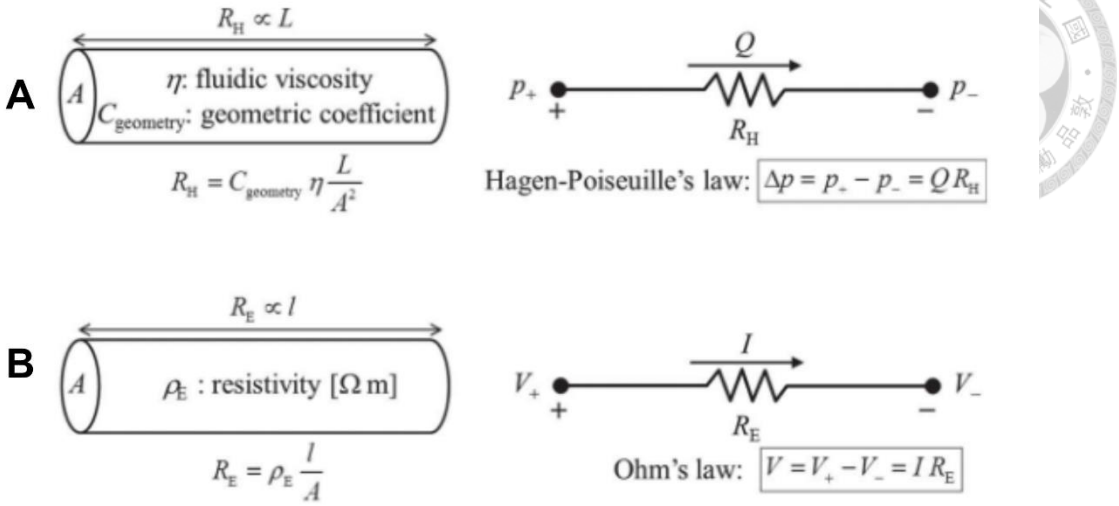

Figure 3-1 Analogy between Hagen-Poiseuille law and Ohm's law [126]

To obtain the flow rate inside the microfluidic channels, we need to understand the Hagen-Poiseuille's equation. For a microfluidic system, we assume that the fluid flowing through microchannels is steady, incompressible, viscous and fully developed laminar flow. Figure 3-2 A shows the flow of a fluid inside a circular microchannel. The pressure at the inlet is P and at the outlet is P+ΔP, where P > (P+ΔP) to ensure forward movement of the liquid. The diameter of the section is 2R and the length is L.

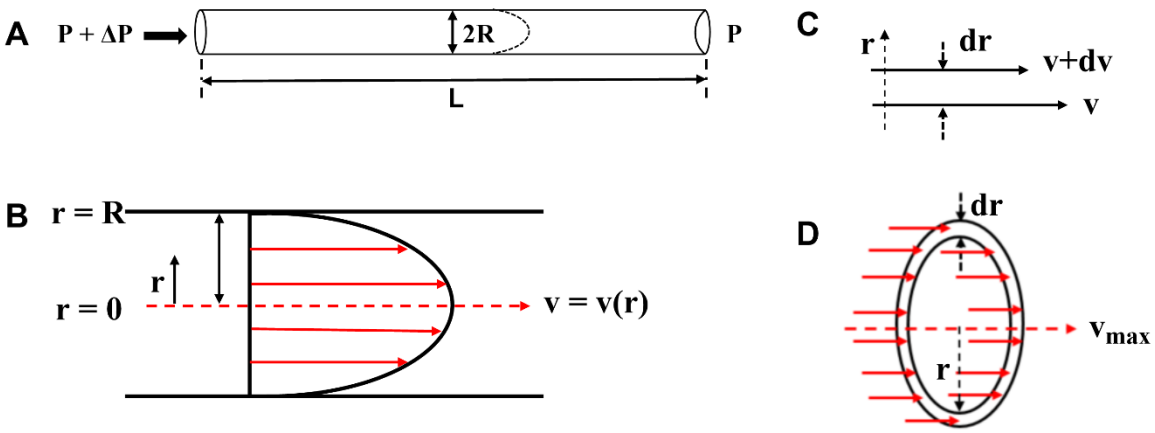

doi:10.6342/NTU202600103

Figure 3-2 (A) Fluid flow through a microchannel (B) Flow profile inside a cross section of the microchannel (C) Schematic illustration of fluid layers used to explain viscosity (D) Cross-sectional schematic used to calculate volumetric flow rate (diagrams are not drawn to scale)

Assume the viscosity of the liquid is η. Due to the viscosity of the fluid, there is a resistance in the opposite direction of the flow. In this condition, the flow within the channel obeys the Poiseuille Law and is characterized by a parabolic velocity profile as shown by dashed line in Figure 3-2 A. The volumetric flow rate is defined as the fluid passing through a given cross-section of the channel per unit time. It is defined as:

$$Q = \frac{dV}{dt}, \tag{1}$$

Where: V = volume, t = Time

To obtain the volumetric flow rate, let us take a cross section of the channel as shown in Figure 3-2 B. At any radius, r, from the center of the flow, the fluid is moving in x-direction with a velocity, v, which is a function of the radius, v(r). At the center, the velocity is maximum and it reduces as the r moves perpendicular towards the wall of the microchannel. At the wall of the microchannel, velocity is zero. Hence,

$$V = 0 \; at \; r = R \; (no \; slip \; condition)$$

$$V = V_{max} \; at \; r = 0$$

Assume, there are two layers of liquid moving (Figure 3-2 C), where the velocity of the first layer is v and the velocity of the second layer at a distance of dr is $v+dv$. The layer that is moving faster exerts a friction force that has a stress created between two layers. Let the stress be $\boldsymbol{\tau}$ and is expressed as:

doi:10.6342/NTU202600103

$$\tau \propto \frac{dV}{dr} \quad (2)$$

$$\tau = \eta \frac{dV}{dr}, \quad (3)$$

Where, τ = shear stress, η = viscosity and dV/dr = velocity gradient

In our case, as r moves towards the wall, velocity decreases. Hence, the velocity gradient is negative. The forces acting on the cylinder are then the force by the fluid and the shear stress that is acting negatively on the channel. Hence,

$$F_{fluid} = (P + \Delta P)\, \pi r^2$$

$$F_{friction} = (2\pi rL).\eta.\frac{dv}{dr}$$

Now, since the flow is steady at the outlet, the friction force is balanced by the force exerted by the 'ΔP' part. Hence,

$$\Delta P \pi r^2 = (2\pi rL).\eta.\frac{dv}{dr} \quad (4)$$

As ΔP is positive because the fluid is moving forward and velocity gradient is negative. To balance the Eq. 4, we add a negative sign to the friction force. Hence, equation 4 becomes:

$$\Delta P \pi r^2 = -(2\pi rL).\eta.\frac{dv}{dr} \quad (5)$$

Rearranging Eq. 5, we get:

$$-\int dv = \frac{\Delta P}{2\eta L}\int r dr \quad (6)$$

Integrating from r to R, we get:

$$-\int_v^0 dv = \frac{\Delta P}{2\eta L}\int_r^R r dr \quad (7)$$

doi:10.6342/NTU202600103

$$v = \frac{\Delta P}{2\eta L}\left(\frac{R^2 - r^2}{2}\right) \quad (8)$$

$$v = \frac{\Delta P}{4\eta L}\left(R^2 - r^2\right) \quad (9)$$

Eq. 9 gives us the velocity profile of the fluid through the microchannel. From this equation, we can intuitively obtain the fluid velocity as discussed above. For r = 0, velocity is maximum at the center and is denoted by:

$$v_{max} = \frac{\Delta P}{4\eta L}\left(R^2\right) \quad (10)$$

For, $r = R$ i.e., at walls, the velocity is zero. Hence, the fluid flow displays the parabolic profile as shown in Figure 3-2 B.

Next, to obtain the volumetric flow rate, we need to first calculate the flow within a cross section of the microchannel. Figure 3-2 D shows the cross section of a tube with radius r and width dr. Let the fluid velocity be v at this cross section. The volumetric flow rate within this section is:

$$Q = 2\pi r dr.v \quad (11)$$

For total volumetric flow rate, integrating equation 11:

$$Q_{total} = \int_{r=0}^{R} 2\pi r dr.v \quad (12)$$

Replacing v with Eq. 9, we get:

$$Q_{total} = \int_{r=0}^{R} 2\pi r dr \frac{\Delta P}{4\eta L}\left(R^2 - r^2\right) \quad (13)$$

$$= \frac{\Delta P}{2\eta L}\left(\int_0^R (R^2.r - r^3)\right) \quad (14)$$

doi:10.6342/NTU202600103

$$= \frac{\Delta P}{2\eta L}\left(R^2\frac{R^2}{2} - \frac{R^4}{4} - 0 - 0\right) \quad (15)$$

Hence, the total volumetric flow rate becomes:

$$Q_{total} = \frac{\Delta P \pi R^4}{8\eta L} \quad (16)$$

Equation 16 represents the Hagen-Poiseuille's equation for total volumetric flow rate. This can be simplified as:

$$Q = \frac{\Delta P}{R_H}$$

Where, R_H is the hydraulic resistance and is defined as:

$$R_H = \frac{8\eta L}{\pi R^4} \quad (17)$$

As the Hagen-Poiseuille's law is analogous to Ohm's law, the *Q* represents the volume flow rate per time whereas in electric systems, *I* represents charge per time. *ΔP* corresponds to voltage *V* and hydraulic resistance R_H corresponds to electrical resistance *R*. As per equation 16, the R_H is inversely proportional to fourth power of the radius. Now for circle, R is radius. But, while fabricating micro-channels, the fabricated channels are either rectangular or square. Hence, for microchannel fabrication, the designer calculates the resistance of the circuit using the formula for square or rectangular shapes. Figure 3-3 shows the R_H expression for different cross-sectional shapes [127]. Thus R_H calculation for micro-channels are:

$$R_H = \frac{28.4\,\eta L}{h^4}\ (for\ square) \quad (18)$$

$$R_H = \frac{12\,\eta L}{1 - 0.63\left(\frac{h}{w}\right)}\frac{1}{h^3\,w}\ (for\ rectangle) \quad (19)$$

doi:10.6342/NTU202600103

Where, L= length, w = width, h = height of the micro-channels

Shape and parameters	R_{hyd} expression
	$\frac{8}{\pi}\eta L\frac{1}{a^4}$
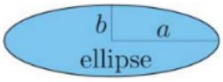	$\frac{4}{\pi}\eta L\frac{1+(b/a)^2}{(b/a)^3}\frac{1}{a^4}$
	$\frac{320}{\sqrt{3}}\eta L\frac{1}{a^4}$
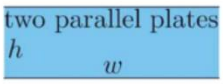	$12\eta L\frac{1}{h^3 w}$
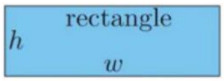	$\frac{12\eta L}{1-0.63(h/w)}\frac{1}{h^3 w}$
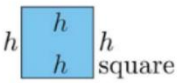	$28.4\,\eta L\frac{1}{h^4}$
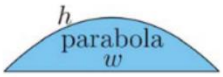	$\frac{105}{4}\eta L\frac{1}{h^3 w}$
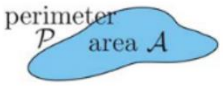	$\approx 2\eta L\frac{\mathcal{P}^2}{\mathcal{A}^3}$

Figure 3-3 Hydraulic resistance expression for channels with different cross-sectional geometries [127]

The above equations are valid for Poiseuille flow that is characterized by laminar and parabolic across the channel. Also, the equations are derived for straight channels. However, complex devices have channels that bend and have branches. To

doi:10.6342/NTU202600103

characterize whether the flow inside the channels follow Poiseuille's rule, Reynold's number is calculated. It is expressed as:

$$R_e = \frac{\rho V L}{\eta} = \frac{inertia\ force}{viscous\ force}$$

where, ρ = density, V = velocity and η = viscosity of the fluid whereas L = length of the microchannel.

Hence, as laminar flow is dominated by viscous forces, Reynolds numbers are typically low. Fluid flow in micro-channels are mostly at low Reynolds number (Re < ~1) due to the narrow diameters and slow volumetric flow rates [128]. Conversely, when inertia forces dominate the flow, the flow becomes turbulent. A low Reynolds number and the absence of turbulence are crucial in minimizing the unsteadiness of the flow at the bending of micro-channels.

Another important design parameter for micro-channels is the Péclet number, which quantifies the contribution of convection or diffusion during mass transport. Péclet number is defined as:

$$P_e = \frac{Advective\ Transport\ Rate}{Diffusive\ Transport\ Rate}$$

A high Peclet number (Pe > 10) indicates convection-dominated mass transport, while a low Peclet number (Pe << 0.1) indicates diffusion dominated mass transport. The microfluidic device design must balance channel geometry to obtain desired Péclet number suitable for the required biological development conditions.

3.1.2 Designing arteriole-on-a-chip device

The device design for developing arteriole-on-a-chip is shown in Figure 3-4. The microchannels in the device have two components as shown in Figure 3-4 B: (i) the

doi:10.6342/NTU202600103

culture chamber where the cells are cultured for developing vascular structures (ii) side channels for media perfusion and also lining HUAECs for anastomosis. There are three ports connected to the culture chamber: a gel loading port and a vent port. The vent port helps to remove any air bubble trapped in the fibrin gel while loading, ensuring the cells inside are free form bubbles. It is important because if bubbles are present inside the chamber, the gel may collapse after few hours. The culture chamber is connected to the side channels via micro-pores with a diameter of 50 μm. These pores help to confine the gel in the culture chamber without spilling it into the media channels. When the gel is injected into the central chamber, it spreads along the rows of these micropores. These pores generate a capillary pressure that confines the liquid gel in the central region before polymerization. Also, they allow controlled diffusion of soluble nutrients to the chamber to maintain a concentration gradient. They also plays an important role in arteriogenesis as small interstitial flow can be applied through them, avoiding a massive flow of media through the chamber that could rupture the gel. Additionally, since cells can migrate through them and sprout within the gel, angiogenesis and tumor invasion assays can be conveniently modeled.

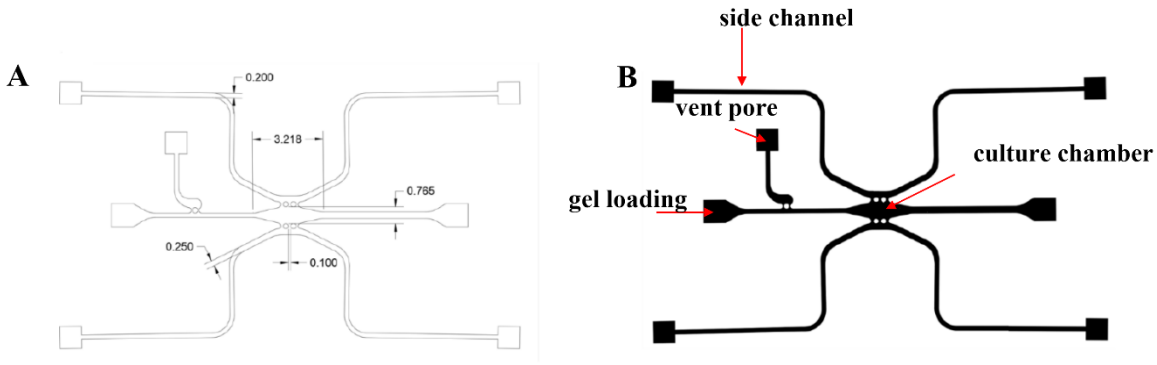

Figure 3-4 Designing the culture chamber for arteriole-on-a-chip. (A) Dimensions of different sections of the device (in mm) (B) Micrograph defining various parts of the device

doi:10.6342/NTU202600103

Next, we determine the hydraulic resistance of the microchannels to verify the device's feasibility for engineering arterioles. The equivalent electrical model of the device is shown in Figure 3-5 B. The microchannels are divided into several segments based on their dimensions. As observed, $R_{AB} = R_{FG} = R_{DE} = R_{IJ}$ and $R_{BC} = R_{CD} = R_{GH} = R_{HI}$. The device becomes symmetrical where $(R_{AB} + R_{BC}) = (R_{CD} + R_{DE}) = (R_{FG} + R_{GH}) = (R_{HI} + R_{IJ}) = R_1$. Hence, the circuit could be simplified into a Wheatstone bridge circuit as shown in Figure 3-5 C. Here $R_{chamber}$ is too high and the resistance of the entire chip becomes $R_1 = R_{chip}$.

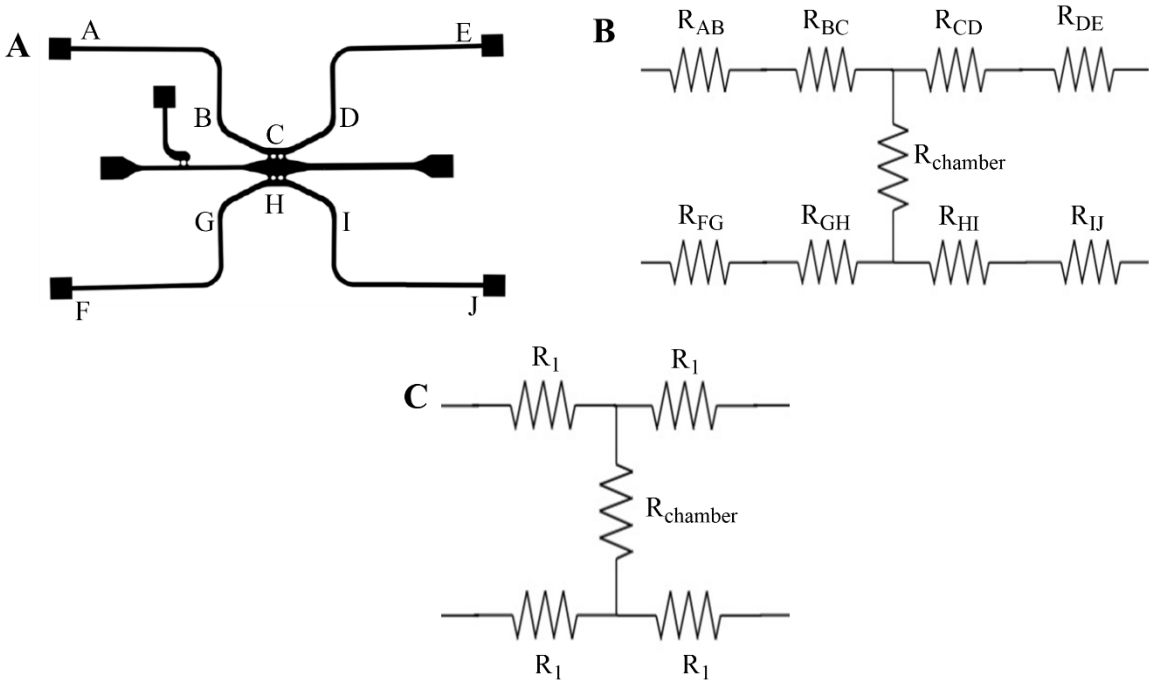

Figure 3-5 (A) Micrograph of arteriole-on-a-chip device (B) Equivalent electrical circuit (C) Simplified Wheatstone bridge network

As the chips are fabricated using standard photolithography, the devices have rectangular cross section. Hence, we calculate the hydraulic resistance of the channels using the formula for rectangular cross-section as stated in equation 19.

doi:10.6342/NTU202600103

$$R_H = \frac{12\,\eta L}{1 - 0.63\left(\frac{h}{w}\right)} \frac{1}{h^3\,w}$$

The device height is 150 μm. Length of the micro-channels are: $L_{AB} = L_{FG} = L_{DE} = L_{IJ} =$ 10.4 mm and $L_{BC} = L_{CD} = L_{GH} = L_{HI} = 3.5$ mm. Width of the micro-channels are: $W_{AB} = W_{FG} = W_{DE} = W_{IJ} = 200$ μm. Assume water's viscosity (η) of 0.68896 mPa.s at 37º C, we get:

$$R_{AB} = R_{FG} = R_{DE} = R_{IJ} = 2.41 \times 10^{11}\ Pa.s/m^3 \quad (20)$$

$$R_{BC} = R_{CD} = R_{GH} = R_{HI} = 0.55 \times 10^{11}\ Pa.s/m^3 \quad (21)$$

Hence adding 20 and 21, we get:

$$R_{chip} = 2.96 \times 10^{11} Pa.s/m^3 \quad (22)$$

Next, we calculate the resistance of the long micro-channels (LMCs) used in this experiment. The microchannel and the equivalent resistance is shown in Figure 3-6. The long micro-channels have a length of 256.704 mm from A to B. At B, the channel is bi-furcated to C and D with a length of 10.597 mm, each (Figure 3-6 A). Figure 3-6 B represents the equivalent electric circuit for the long micro-channel. Here, $R_{BC} = R_{BD}$ are in parallel and are in series with R_{AB}. So, the equivalent resistance of the circuit is $R_{AB} + (R_{BC} \parallel R_{BD})$.

The width and height of the micro-channel is 100 μm X 100 μm, so the cross section is square. Hence, we use the formula of square cross-section for calculating the hydraulic resistance from Figure 3-3:

$$R_H = \frac{28.4\,\eta L}{h^4}$$

doi:10.6342/NTU202600103

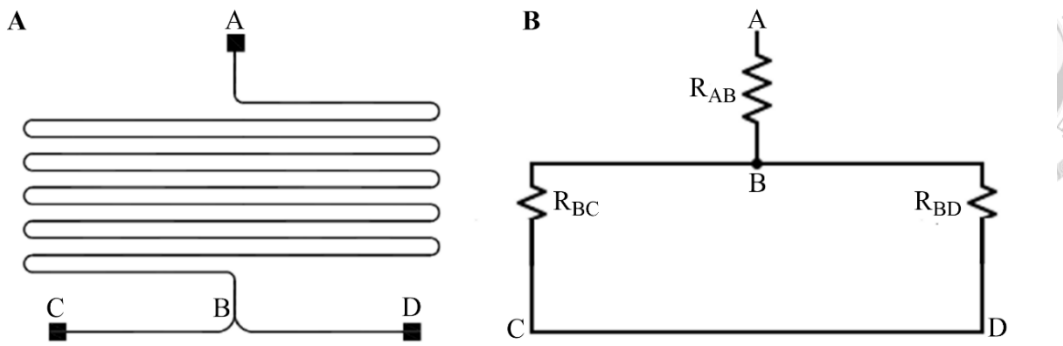

Figure 3-6 (A) Schematic representation of long micro-channel (B) Equivalent electric circuit

Substituting the values for length and viscosity of water in the above formula, we obtain:

$$R_{AB} = 5.02 \times 10^{13}\ Pa.s/m^3 \quad (23)$$

$$R_{BC} = R_{BD} = 0.207 \times 10^{13}\ Pa.s/m^3 \quad (24)$$

So, the equivalent resistance of the circuit is:

$$R_{LMC} = 5.12 \times 10^{13}\ Pa.s/m^3 \quad (25)$$

3.1.3 Designing set up for diffusion based mass transfer in the arteriole device

The objective here is to employ diffusion based mass transfer inside the culture chamber and induce hypoxia to promote vasculogenesis and angiogenesis. For diffusion based mass transfer, the arteriole chip is connected to symmetrical LMCs at the media outlets via jumpers as shown in Figure 3-7 A. The LMCs are connected to media reservoirs where P_{in} = 13 mm H_2O and P_{out} = 3 mm H_2O. Hence, the pressure difference is 10 mm H_2O. Intuitively, as same pressure difference is applied from both side channels, the pressure

doi:10.6342/NTU202600103

drop inside the chamber is negligible. This indicates that the mass transfer inside the chamber is diffusion dominated.

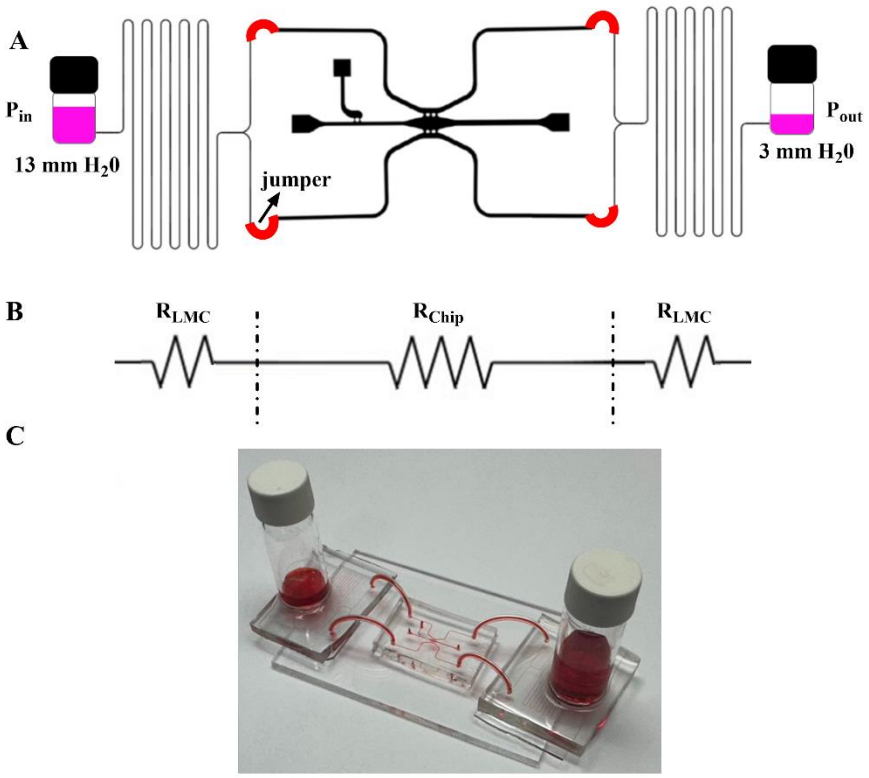

Figure 3-7 Diffusion based mass transport (A) schematic representation of microfluidic configuration (B) equivalent electric circuit (C) micrograph of device set up

The equivalent electric circuit is shown in Figure 3-7 B. As observed, the chip is symmetrically sandwiched between two LMCs. Also, the resistance of LMCs are 2 orders lager than resistance of the chip. Hence, maximum pressure drops across the LMCs and negligible pressure is dropped across the chip. To calculate the pressure drop across the LMCs and the device, we calculate the total resistance of the circuit. So,

$$R_{total} = R_{chip} + 2(R_{LMC})$$

Inserting the values from equation 22 and 25, we get

$$R_{total} = 2.96 \times 10^{11} + 2(5.12 \times 10^{13})$$

doi:10.6342/NTU202600103

$$R_{total} = 1.026 \times 10^{14}\ (Pa.s/m^3) \quad (26)$$

P_{in} is 13 mm H_20. So,

$$Q = P/(R_{total})$$

Inserting the values for P_{in} and R_{total}:

$$Q = 13/1.026 \times 10^{14}$$

$$Q = 1.267 \times 10^{-13} m^3/s \quad (27)$$

So, pressure drop across R_{LMC} is:

$$P_{LMC} = (1.267 \times 10^{-13})(5.12 \times 10^{13}) \quad (28)$$

$$P_{LMC} = 6.48\ mm\ H_2O \quad (29)$$

Pressure drop across the chip is:

$$P_{Chip} = (1.267 \times 10^{-13})(2.96 \times 10^{11})$$

$$P_{Chip} = 0.0375\ mm\ H_2O \quad (30)$$

So, 99.6% pressure drops across the LMCs and only 0.29% pressure drops across the chip. Hence, we confirm that this set up is capable of diffusion dominated mass transport and when placed inside 5% O_2 chamber, hypoxia could also be induced. Hypoxia is further promoted by fabricating the PDMS device with a greater height, thereby limiting oxygen diffusion across the PDMS and reducing O_2 exchange between the chamber and the surroundings.

doi:10.6342/NTU202600103

3.1.4 Designing set up for convection based mass transfer at high oscillating flow

The objective here is to generate convection based mass transport within the chamber to achieve controlled oscillating flow. The setup is designed to mimic physiological conditions, where the heart generates pulsatile flow, ensuring steady shear stress and promoting proper endothelial mechano-transduction. We use GenePure Rocking Shaker that rocks in a see-saw motion at an angle of 45º. We set the speed to obtain 1Hz frequency, similar to a beating heart.

Figure 3-8 A shows the schematic representation of the set up needed for generating high oscillating flow inside the chamber. The media outlets are connected with wide micro-channels (WMCs) with dimensions 30 mm x 2 mm x 300 μm. The ends of the WMCs are connected to media reservoirs so that media heights are P1 = 15 mm H_2O, P2 = P4 = 10 mm H_2O and P3 = 5 mm H_2O. The resistance imposed by these channels are calculated by using the formula for rectangular cross-section from Figure 3-3 and is calculated as:

$$R_{WMC} = 5.07 \times 10^{9} Pa\ s\ m^{-3}$$

As the low-resistance WMCs are connected in series to the device, the media can flow freely to the chip. Due to the difference in media height, there is a resting pressure difference of 5 mm H_2O from A to B and from A to C. This pressure difference already generates convection based mass transport inside the chamber.

doi:10.6342/NTU202600103

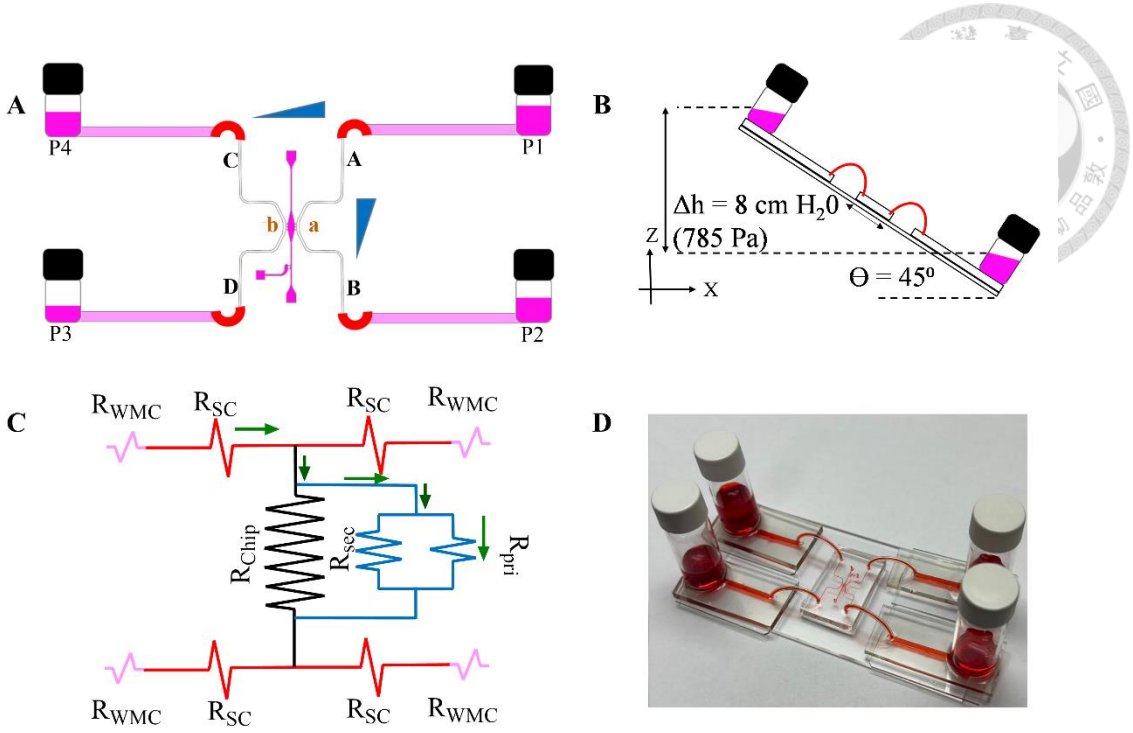

Figure 3-8 Set up for generating high oscillating flow. (A-B) schematic representation of microfluidic configuration for generating high oscillating flow (B) equivalent circuit diagram (C) micrograph of device set up.

The entire set up is rocked at 1 Hz frequency on a see-saw rocker. Figure 3-8 B shows a schematic representation of the device when it is tilted to the right side at an angle of 45º. When the device is tilted to the right, the medium flows from C → D, with flow inside the chamber moving from b → a. Conversely, when the device tilts to the left, the medium flows from A → B, and inside the chamber, it moves from a → b. As a result, the side channels experience unidirectional flow, while the flow inside the chamber oscillates between a and b. Consequently, the vessels within the chamber are subjected to periodic oscillatory flow, which drives their remodeling due to the shear stress they experience.

To calculate the dynamic pressure inside the chamber, we need to check the media height difference while tilting. The WMCs are connected to the device via jumpers of

doi:10.6342/NTU202600103

length 1-2 cm. The length of each WMC is 3 cm. Hence, the total distance between media reservoir and the outlet of the device is around 5 cm. So, the distance between the two media reservoirs is 10 ± 1 cm. Hence, when tilted, an approximate vertical distance of Δh = 80 mm H_20 is between the two media reservoirs. This generates an internal pressure of approximately 785 Pa within the device, with the majority of this pressure being borne by the chip due to the low resistance of the reservoirs.

Figure 3-8 C shows the equivalent electric circuit of the set up. When maximum pressure drops across the chamber, the connected vessels and the chamber experience that pressure. However, as the chamber resistance is higher than the perfused vessels, most of the media flows through the intraluminal space instead of the interstitial space. The shear stress induced due to this flow remodels the vessels. Figure 3-8 C shows two vessels connected across the chamber, one with a wider diameter and another with a narrower diameter. The vessel with the wider diameter is primary vessel and hence the resistance offered by this vessel is termed as R_{pri}. Similary, the resistance offered by the secondary vessel is termed as R_{sec}. Since $R_{pri} < R_{sec}$, majority of flow will be through the primary vessel.

3.1.5 Designing set up for convection based mass transfer at low oscillating flow

Figure 3-9 shows the set up for generating a low oscillating flow. In this case, the long channels are replaced by pipette tips where P1 = 30 mm H_2O, P2 = P4 = 25 mm H_2O and P3 = 20 mm H_2O. The tilted height was 12 mm H_2O that generated a pressure of 82.37 Pa. Similar to the high oscillating flow case, the inserted pressure was experienced by both the interstitial space and the vessels connecting to the pores. Figure 3-9 C shows the representative circuit diagram for flow inside the chamber. Due to direct connection of

doi:10.6342/NTU202600103

the tips to the media outlets, all the pressure was experienced by the device. Imagine two perfused vessels connected the pores from either side: (i) one with a larger diameter and smaller resistance, named as primary vessel (R_{pri}) and (ii) another with a smaller diameter and larger resistance, named as secondary (R_{sec}). As the vessels have much lower resistance than the R_{chip}, most of the flow is perfused through the vessels, especially R_{pri}. Figure 3-9 D shows a micrograph of the device set up.

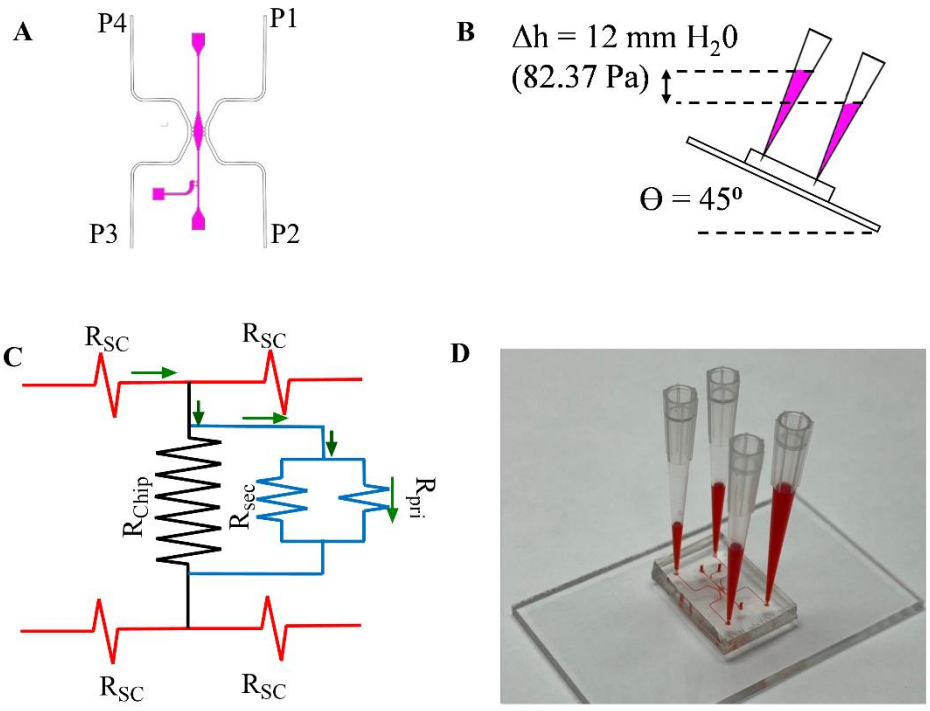

Figure 3-9 Set up for generating low oscillating flow. (A-B) schematic representation of microfluidic configuration for generating high oscillating flow (C) the equivalent circuit diagram and (D) a micrograph of device set up.

In our case, high and low flow are relative to each other and do not represent any predefined absolute value. After multiple experiments, we found that the “low” flow generated a pressure that was approximately 9.53 times lower than the pressure generated at “higher” flow conditions. Since, the vascular remodeling observed in both conditions

doi:10.6342/NTU202600103

is markedly different, we used these two pressure levels to represent and study vessel remodeling under low and high shear stress environments.

3.2 Experiment protocol for developing arteriole-on-a-chip

3.2.1 Overview of experiment timeline

Figure 3-10 A-C shows the schematic representation of the processes used in this dissertation to develop arterioles. Figure 3-10 D shows the experiment timeline for developing arterioles. The experiement timeline is divided into 3 parts: (i) vasculogenesis (ii) angiogenesis and (arteriogenesis). Vasculogenesis is performed to form the initial vascular network by co-culturing HUAECs, NHLFs and HUSMCs. For angiogenesis, high-density HUAECs are lined on side channels that can sprout into the gel and anastomose with the developed vessels inside. This step ensures that the newly formed vessels establish open connections with the adjacent side channels through the micropores, enabling direct perfusion and the establishment of controlled intraluminal flow. The perfused vessels are then subjected to arteriogenesis to study the influence of shear stress in vascular remodeling.

Vasculogenesis and angiogenesis occur under diffusion-dominated mass transport conditions, whereas arteriogenesis requires a convection-dominated transport environment. Vasculogenesis is established by Day 4 of culture, marked by the development of primitive vascular plexus in the central chamber. On Day 4, high-density HUAECs are lined along the side channels and angiogenic sprouting is initiated, giving rise to interconnected and perfusable microvessels by Day 7–8. For the next 48 hrs, arteriogenesis is induced by applying convection-driven flow using a see-saw rocker. After every 24 hrs of application of oscillating flow, the side channels were perfused with

doi:10.6342/NTU202600103

70kDa FITC dextran to observed the remodeled vascular structure. On Day 10, devices are fixed with 4% paraformaldehyde and prepared for immunostaining.

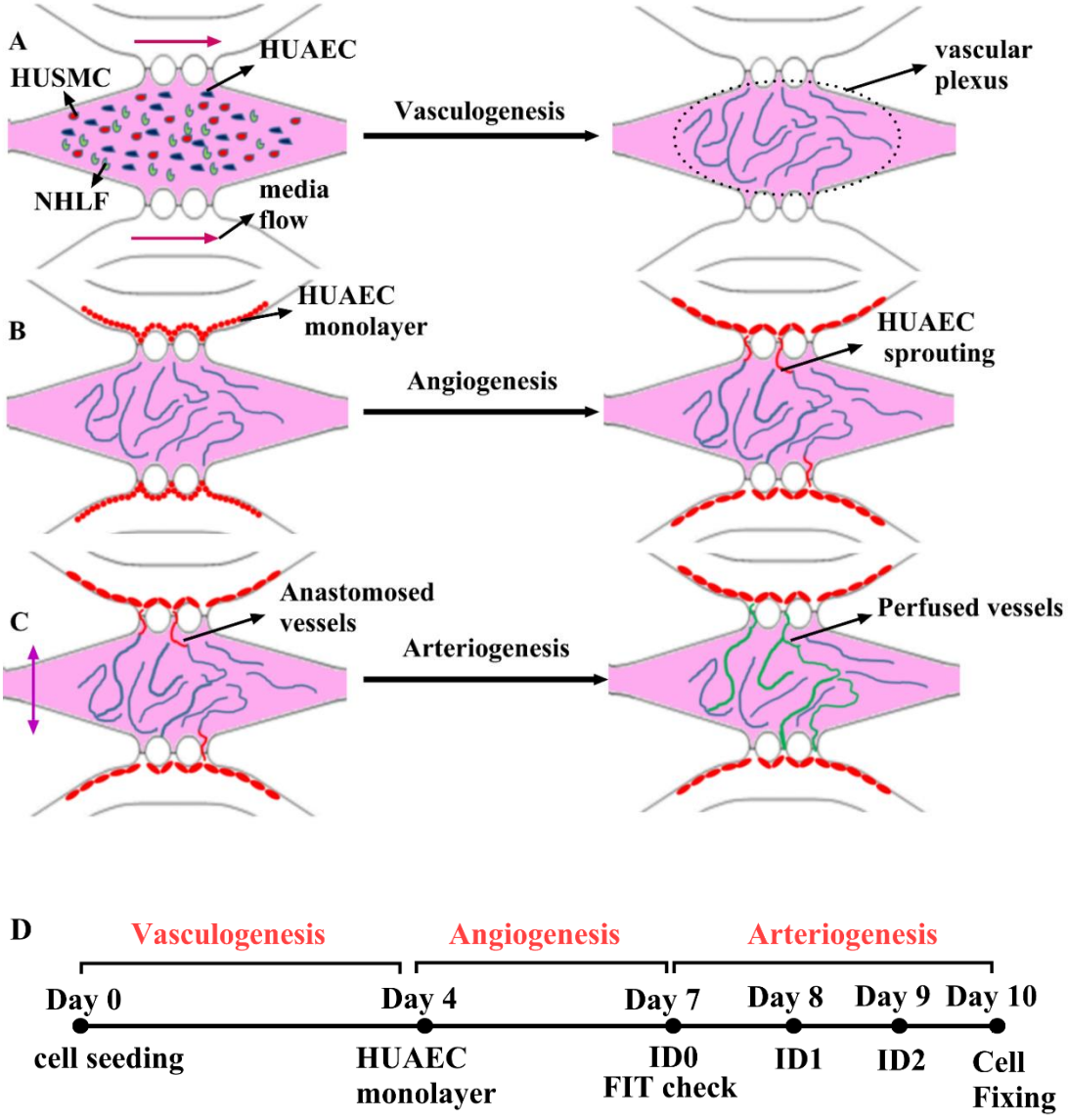

Figure 3-10 (A-C) Schematic representation of processes used for developing perfusable and matured arteriolear MVNs (D) Timeline for developing arteriole-on-a-chip.

3.2.2 Detailed workflow for developing arteriole-on-a-chip

The cells are optimized for a ratio of 2:2:0.5 for HUAECs, NHLFs and HUSMCs. A cell concentration of 2E7 cells/mL is prepared by mixing the cells in the above ratio. The cells were centrifuged at 4000 RPM for 4 minutes, after which the centrifuge tubes were

doi:10.6342/NTU202600103

inverted 180° and centrifuged again for an additional 4 minutes. Media was carefully sucked out of the tubes post-centrifugation. Cells were added to 15 μL fibrinogen (10 μg mL^{-1}) and pipetted well to mix the cells uniformly. Next, they were transferred to another Eppendorf with 4 μL thrombin (5 U mL^{-1}) and pipetted quickly 4-5 times. (Note: this step should be quick as the thrombin initiates gel polymerization)

A 200 μL pipette tip is tucked inside the outlet port of the central chamber to serve as a vertical extension. The cell-fibrin mixture is loaded into the central chamber until the cells can be observed rising in the outlet tip for ~ 5-10 mm height. This ensures that cell is confined to the central chamber and have not leaked to adjacent microchannels, indicating successful loading of the device. The devices are immediately put inside a 5%CO_2/20% O_2/37ºC incubator for 30 mins for complete solidification of the gel. After 30 mins, four 200 μL pipette tips are gently inserted into the media ports of the device. HUAEC culture medium with growth factors (Science Cell) was delivered to the side channels through the pipette tips using gel loading tips and the devices were cultured in a 5%CO_2/20% O_2/37ºC incubator for 6 hrs to allow the cells to settle down. After 6 hrs, the side channels were connected to glass reservoirs via silicon jumpers and the media was replaced by EGM-2 media without the growth factors. The media height of the reservoirs are shown in Figure 3-7 A and the entire set up was placed in a 5%CO_2/5% O_2/37ºC incubator. This created diffusion-dominated mass transport in a hypoxic environment and induced vasculogenesis.

On Day 4, the glass bottles were replaced with pipette tips and the side channels were flushed with warm PBS to remove media. Rat Fibronectin (4 uL/mL) in cold PBS was introduced to the side channels to create a thin coating for 1-1.5 hrs. After coating, the side channels were flushed with warm PBS for 15 mins to remove extra fibronectin. Next, high-density HUAEC (5E6 cells/mL) suspension was introduced into one side

doi:10.6342/NTU202600103

channel via gel loading tips and the device was tilted with coated side facing up for 15 mins to promote adhesion of the cells near the pores. This increases the likelihood of HUAEC sprouting into the gel, anastomosing with the vessel network and creating openings towards the micropores. After 15 minutes, the process is repeated for the other side channel. After lining both side channels, the device is kept in a 5%CO_2/20% O_2/37ºC incubator for 1 hr for adhesion of the cells. After 1 hour, the devices were examined under a microscope to assess cell adhesion. If adhesion appeared weak, 50 µL of HUAEC medium with growth factors was gently perfused (without disturbing the attached cells) through the pipette tips to maintain hydration and prevent cell death. The devices were then returned to the incubator (37°C, 5% CO_2, 20% O_2) for an additional 30–60 minutes. By this time, the majority of cells had successfully adhered to the side channels. After successful adhesion, the pipette tips are replaced with glass reservoirs which were filled with HUAEC medium to the same height as previously maintained. Media height is maintained every 24 hrs.

On Day 7, the glass reservoirs were replaced with pipette tips and 70k Da FITC-labeled dextran in a PBS solution was perfused through them via gel loading tips. The devices were observed under a fluorescent inverted microscope (Olympus IX71) to check vessel perfusion. If the vessels were already perfused, they were either subjected to high oscillating flow or low oscillating flow to induce arteriogenesis for 48 hrs. To assess dynamic vascular remodeling, the devices were perfused with 70k Da labeled FITC dextran after 24 hrs of initiation of convection-driven flow. The day of arteriogenesis induction is designated as “investigating day 0 (ID0)”. The subsequent observations at 24hrs and 48 hrs are referred as ID1 and ID2, respectively. Vascular parameters were quantified from the FITC images of ID0, ID1 and ID2 to evaluate remodeling over time. After ID2, devices subjected to high flow were either used for disease modeling/ drug

doi:10.6342/NTU202600103

testing before fixation and immunostaining. The low shear and control devices were fixed and prepared for immunostaining immediately.

doi:10.6342/NTU202600103

4. Materials and Methods

4.1 Fabrication of Devices

The arteriole chip is designed by the PI of this project using the design principles discussed previously. The layout was designed in AutoCAD and was converted to a photomask-ready reading file. The master mold was developed by the standard cleanroom photolithography method by a former Master's student, as described in her dissertation [129]. Using soft lithography and plasma bonding technique, multiple microfluidics chips can be reproduced. In this section, we discuss the protocol for fabricating PDMS-based arteriole chips.

4.1.1 Soft lithography technique for chip fabrication

Soft lithography technique uses soft and elastomeric materials to create micro/nano strcutures through replica molding. PDMS is widely used in microfluidic device fabrication for biological experiements due to its flexibility, transparency, high fidelity, non-toxicity, biocompatibility and controllable gas permeability [130], [131]. In addition, its ease of bonding to glass/itself and affordability makes it suitable for rapid prototyping and mass manufacturing. The following steps detail the soft lithography process used in this study:

1. Mix PDMS base (A) and the curing agent (B) thoroughly at a 10:0.9 ratio until the mixture becomes white and cloudy due to small bubbles.
2. Place the mixed PDMS in a vacuum chamber to remove air bubbles completely.
3. Slowly pour the bubble-free PDMS onto the silicon wafer mold to avoid introducing air bubbles. Place it on an optical table to level and cure naturally, ensuring the surface remains even.

doi:10.6342/NTU202600103

4. After partial curing, transfer the PDMS to a 55 °C oven and cure for 6 hours. If left too long, the PDMS will become overly rigid and may crack during hole punching, making it unusable.
5. Once fully cured, cut the PDMS inside a biosafety cabinet and punch the inlet/outlet holes. Immediately pour a new batch of PDMS onto the silicon wafer mold to prevent oxidation.
6. Use Scotch tape to remove dust from the PDMS and apply the tape temporarily to protect the micro-channels. The PDMS devices are now clean and ready to be bonded to glass coverslips to assemble the final microfluidic chips for experiments.

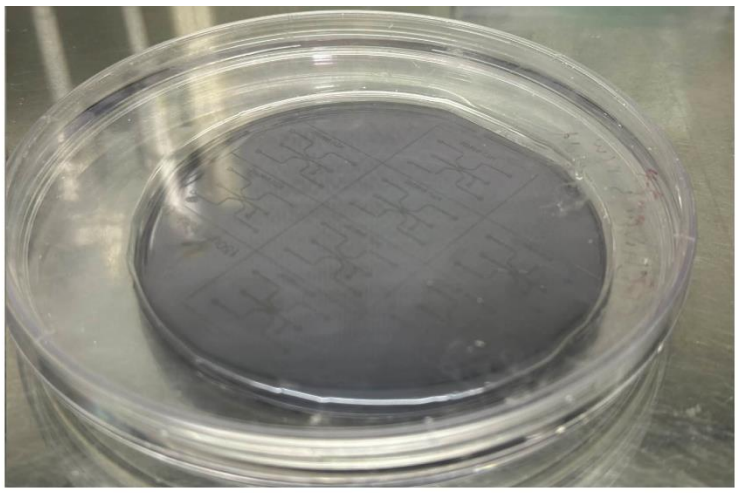

Figure 4-1 Silicon-wafer master mold fabricated according to the device design

We use a glass coverslip to seal the exposed channel surface of the microfluidic device. A thin layer of PDMS is coated on the coverslip to reduce breakage and improve sealing. A thin, uniform PDMS layer is applied to the coverslip by spin coating. The steps are described as below:

doi:10.6342/NTU202600103

1. A cover slip is placed on the spin coater's rotor and the vacuum is turned on to secure it in place.
2. PDMS is scooped with a pipette tip and placed at the center of the coverslip.
3. The chamber is closed, and the rotor is spun at 2000 RPM for 30 seconds
4. The vacuum is turned off, and the coverslip is carefully lifted from the edges to avoid disturbing the coated PDMS layer.
5. The PDMS-coated coverslip is placed on a pre-heated 70 °C hot plate for 30 minutes to allow the PDMS to cure. A folded sheet of aluminum foil is placed over the hot plate to prevent dust particles from settling on the uncured PDMS.
6. After 30 mins, the coverslips are removed from the hot plate and stored in a covered box.

After fabricating the devices, we perform oxygen plasma bonding using a Plasma Cleaner PDC-001 (Harrick Plasma, USA). Surface treatment of PDMS was performed at a maximum power of 30 W. The detailed procedure is as below:

- Clean the inside chamber and the O-ring of the plasma cleaner with IPA. Without this step, bonding will not be successful.
- Perform steps 4-6 for preparing the chamber for bonding without PDMS. For the preparation step, do not turn off the pump immediately and wait until the chamber pressure drops to **1.5 E^{-1} mTorr**. After finishing, perform steps 3-6 with PDMS for bonding.
- Place the cleaned PDMS pieces and the coverslips into the plasma chamber with the surfaces to be treated facing upward.
- Close the chamber valve and turn on the pump to evacuate the chamber until **1.5 E^{-1} mTorr**.

doi:10.6342/NTU202600103

- Once the pressure reaches **1.5 E^{-1} mTorr**, open the oxygen valve to introduce O_2 and adjust the control knob until the pressure stabilizes between **5.5 E^{-1} and 6.0 E^{-1} mTorr**. Next, turn on the plasma power, and set it to maximum. Run the plasma for **90 seconds**.
- After the process is complete, sequentially turn off the plasma power, oxygen valve, and vacuum pump. Slowly open the three-way valve to release the vacuum, preventing displacement of PDMS pieces due to rapid pressure change.
- When the pressure returns to atmospheric level, open the chamber and remove the PDMS. Immediately place the treated PDMS surfaces together for bonding and press them with little pressure to ensure proper bonding.
- Place the bonded device in a 55 °C oven for at least **20 minutes** to complete bonding and finalize the microfluidic chip assembly.

Figure 4-2 Oxygen plasma bonding machine used for device bonding

Later, check the devices by slightly pulling from edges to confirm proper bonding. If the two layers are immovable, then the bonding is successful. The bonded devices are then autoclaved for sterilization and dried inside oven at 55º C for 24 hrs to ensure proper

doi:10.6342/NTU202600103

drying of the device. This prevents bubble formation during loading and allows for PDMS to reach a hydrophobic state, thereby increasing the chances of a successful experiment.

4.2 Cell Culture and Immunostaining Methodologies

4.2.1 Cell culture

HUAECs and HUSMCs were purchased from ScienceCell and NHLF was bought from Lonza. The cells were cultured in their respective media following the manufacturer's instructions. HUAEC was expanded four times before loading at passage number 5 (P5). We observed that HUAECs loaded beyond P5 formed slower and imperfusable vessels. Hence, the cells must be loaded between P4 and P5 to obtain well-developed MVNs. HUAECS P6-P8 can be used for lining the side channels for anastomosis and angiogenesis. HUSMCs and NHLFs were cultured until P10 and P20, respectively. During expansion or before loading, the cells were passaged at ~90% confluence. The media was changed every three days during the culture period.

4.2.2 Cell Fixation

After completing the experiments, the devices were gently washed with warm PBS to remove residual media and retain the structural integrity of the MVNs. The devices were then removed from the P2 biosafety lab facility, and all subsequent steps were performed in the main lab biosafety hood to avoid exposing the live cells to any toxic reagents. 4% paraformaldehyde solution (room temperature) was perfused through the side channels for 30 mins to fix the cells. After 30 minutes, the devices were gently flushed with 0.1% Triton three times, with a 10-minute incubation period between each wash. Next, 0.5% Triton was used to permeabilize the structures for immunostaining. Again the devices were washed as described previously. The devices were then perfused with 3% BSA and stored in 4º C for one week to prevent non-specific binding and improve staining quality.

doi:10.6342/NTU202600103

Glass and PDMS can adsorb protein easily. Hence, BSA coating creates a protein shield so that the antibodies do not stick to the non-specified channel walls. After BSA treatment, the devices were washed three times with 0.1% Triton and were then ready for immunostaining.

4.2.3 Immunohistochemistry Protocol

After completing all immunostaining, the devices were washed with 0.1% Triton, and PBS was perfused through the channels before storing the devices at 4 °C for imaging.

Table 1 lists the immunostains and the antibodies used in the research. The reagents are diluted in 3% BSA and perfused through the devices for at least seven days to ensure optimal staining. The height of the reagent solution in the pipette tips was adjusted twice daily to maintain continuous flow through the MVNs. After completion of each staining, the devices were washed with 0.1 % Triton thrice before staining the next reagent. After completing all immunostaining, the devices were washed with 0.1% Triton, and PBS was perfused through the channels before storing the devices at 4 °C for imaging.

Table 1 List of reagents used in the research

Marker	Reagent	Colour	Company	Concentration
Nucleus	Hoescht 33342	Blue	Thermofisher	1: 1000
Vessels	CD31	Green/Red	ebiosciences	1: 200
Basement membrane	Collagen IV	Purple	ebiosciences	1:200
Blood platelets	CD41a	Red	ebiosciences	1:200
Smooth muscle cells	Calponin	Green	Fabgennix	1:150
Leukocytes	CD18	Red	Thermofisher	1:150

doi:10.6342/NTU202600103

Nitric Oxide	DAF-FM	Green	Thermofisher	10 μM
vWF stimulator	PMA	NA	MERCK	50 ng mL^{-1}
Atherogenic agent	TMAO	NA	Sigma Aldrich	200 μM

After completing all immunostaining, the devices were washed with 0.1% Triton, and PBS was perfused through the channels before storing the devices at 4 °C for imaging.

4.3 Whole blood acquisition

Fresh whole blood was drawn from a consenting individual into a collection tube with 3.8% sodium citrate. The blood was mixed uniformly with the sodium citrate to avoid clotting and was introduced to the MVNs within 2 hrs of acquisition. Blood collection was conducted in accordance with the Human Subject Research Act and was approved by the Ethics Committee of National Taiwan University. The corresponding Institutional Review Board number is 202112MH021.

4.4 Quantification and Analysis

The devices were live-imaged from ID0 to ID2 to monitor vessel development and assess structural remodeling. The live images were done using an inverted fluorescence microscope (Olympus X71). The fluorescent images were obtained using a z-stack setting of spin disk confocal microscope (Andor BC43, Oxford instruments). The images were analysed using ImageJ software. All detectable vessels were analysed to obtain the vessel parameters, including diameter, number of branch points, vessel segments and MVN area. Normality of data and homogeneity of variance were assessed using GraphPad Prism software and parameteric or non-parametric tests were performed accordingly. Statistical significance was determined at $p < 0.05$ and each experiment was repeated at least three times to confirm reproducibility.

doi:10.6342/NTU202600103

4.5 Finite Element Analysis

4.5.1 Obtaining 3D surface renderings of the vascular/basement network

To obtain the velocity and shear stress profiles inside the developed MVN, the network architecture was obtained from the confocal disk images. The 3D surface rendering was obtained using the following steps:

1. The vessel and basement membrane immunostains were imaged as z-stacks in the spin-disk microscope
2. The images were opened in IMARIS software and the "SURFACE" function was used to obtain the corresponding surface profiles of the z-stacked images. This provided a 3D rendering of the vascular network. Similarly, we obtained 3D rendering of the basement membrane network.
3. To export the 3D renderings, go to **3D view** > **Export Selected Objects**
4. Open the desired location and save the file as a **VRML2** file type with **.wrl** extension.
5. The exported file is converted from **.wrl → .stl**
6. The **.stl** file is cropped to obtain the desired section of the 3D image needed for finite element analysis.

4.5.2 Obtaining Finite Element Analysis

The cropped .stl file of the vessel was imported into COMSOL Multiphysics® for finite element analysis. To simulate hemodynamics under high-flow conditions, a constant pressure of 785 Pa was applied at the inlet and 0 Pa at the outlet, while no-slip boundary conditions were imposed on all vessel walls. The model was solved under steady-state conditions to obtain the velocity distribution, wall shear stress (WSS), and volumetric

doi:10.6342/NTU202600103

flow rate throughout the vessel. To analyze spatial variations in flow, the vessel was sectioned at eight distinct planes along both primary and secondary regions. At each plane, the velocity and wall shear stress were averaged across the cross-section, and profiles were plotted to quantitatively assess the local flow dynamics and shear stress distribution.

doi:10.6342/NTU202600103

5. Results

5.1 Optimizing experimental protocol

5.1.1 Optimizing thrombin concentration

Thrombin and fibrinogen are the key components for making the fibrin gel. Using the optimal stiffness of fibrin gel ensures better vasculogenesis and stability of the vascular networks. Previous studies reported that thrombin concentrations ranging from 0.5 - 3 U/mL with 2-10 mg/mL fibrinogen solution provide optimal concentration for vasculogenesis [132], [133]. However, in our case, we found the thrombin concentration of 3 U/mL concentration to be too viscous to flow within the microchamber and the cells were coagulated along the streak of thrombin (Figure 5-1). On Day 4, the cells grew along the streak without migrating towards the pores. This is not suitable for developing perfusable vessels as there cannot be any opening at the pores. Hence, we experimented with lower thrombin concentration to optimize the fibrin gel for our experimental requirements.

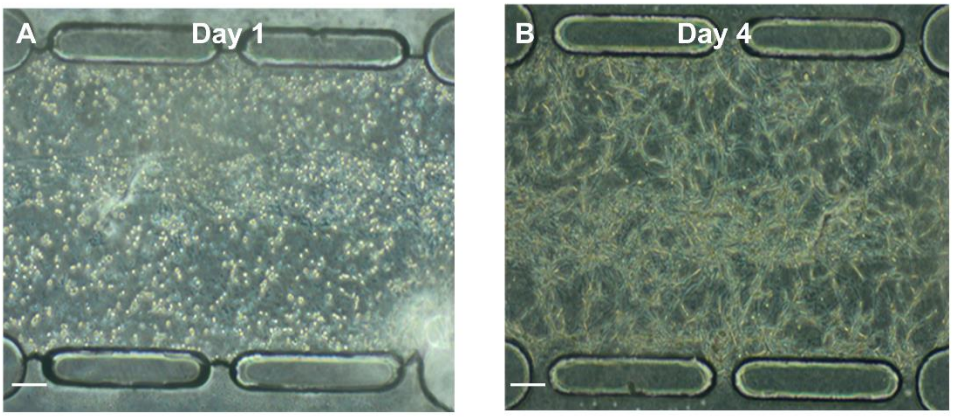

Figure 5-1 Fibroblast loaded with thrombin (3U/mL) in 1% fibrinogen (A) Day 0: due to higher concentration of thrombin, cell dispersion is not uniform and lined along the thrombin. (B) Cells grow along the lines with minimum migration towards the pores (scale bar = 100 μm)

doi:10.6342/NTU202600103

We loaded 0.5 E7/mL fibroblasts with different concentrations of thrombin (Fig. 5): (A) 0.5 U/mL (B) 0.83 U/mL (C) 1.16 U/mL (D) 1.5 U/mL with 10 mg/mL fibrinogen. Figure 5-2 shows the growth of fibroblasts in different thrombin concentrations. Although same concentration of cells are loaded in all cases, the cell distribution inside the chamber varied markedly with thrombin concentration. Notably, the thrombin concentration of 1.16 U/mL resulted in most uniform cell dispersion throughout the chamber (Figure 5-2 A). The cells were separated with minimal aggregation or cell cluster indicating a stable and homogeneous incorporation into the fibrin gel. Interestingly, at this concentration, the cells inside the chamber appeared to be more densely distributed than in other conditions, although initial loading density of fibroblasts was same. This could be due to the difference in fluidity of the gel while injecting into the chamber. As thrombin concentration influences the viscosity and rate of polymerization of the gel, the flow rate and consequently the uniformity in cell distribution can vary between thrombin concentrations.

On Day 4, the device with thrombin concentration of 1.16 U/mL (Figure 5-2 C) had the best spread of fibroblasts with maximum occupancy of the chamber. In contrast, the other thrombin concentrations produced uneven cell distributions, with regions of high-density clumping or areas with sparse cell. Hence, for our experimental conditions, final thrombin concentration of 1.16 U/mL is best for vessel growth.

doi:10.6342/NTU202600103

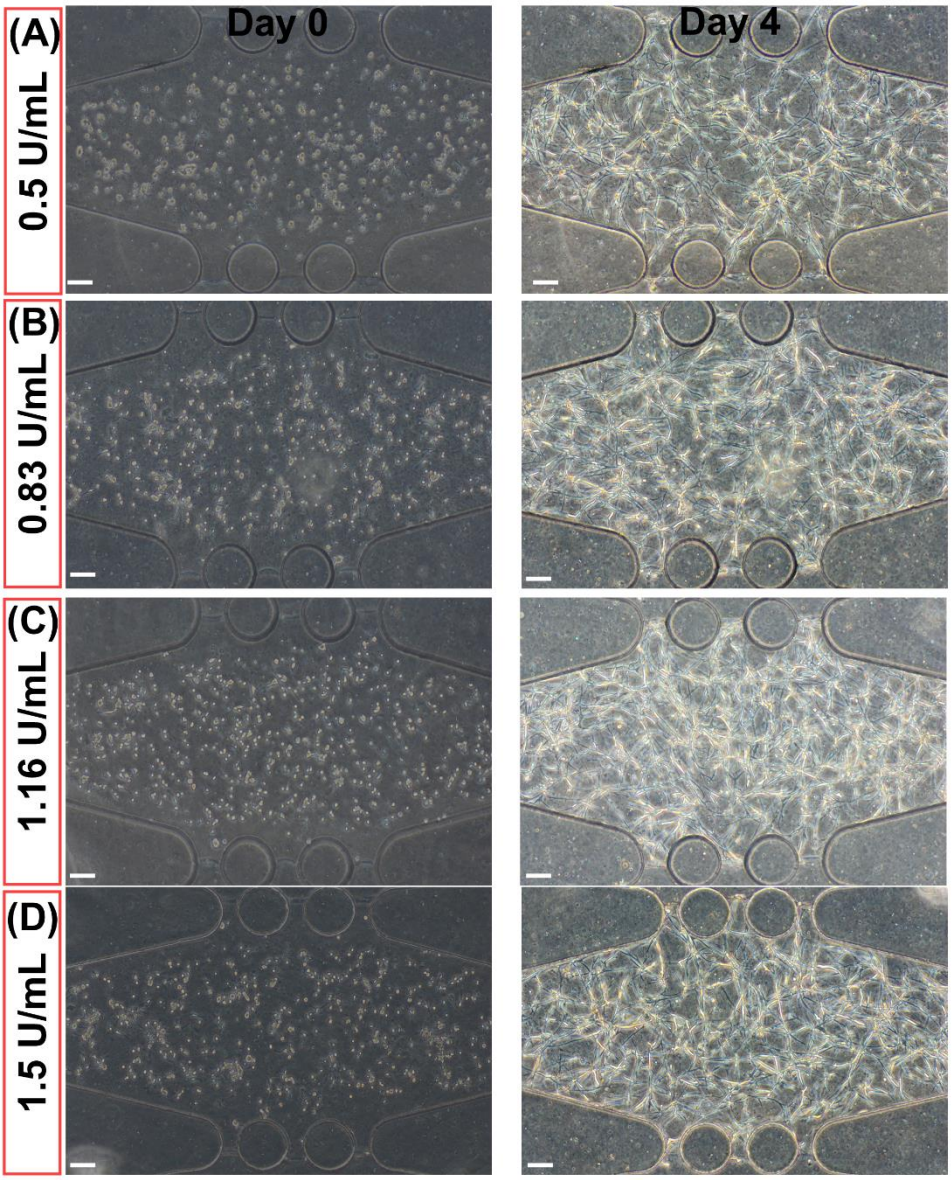

Figure 5-2 Comparison of fibroblasts growth in different thrombin concentrations (A) 0.5 U/mL (B) 0.83 U/mL (C) 1.16 U/mL (D) 1.5 U/mL (scale bar = 100 μm)

5.1.2 Optimizing fibronectin coating of side channel

Before lining the cells on side channels for anastomosis, we coat the side channels with extracellular matrix (ECM). This coating on side channels promotes faster cell adhesion to the device ensuring enough cell density for anastomosis. Since we are using HUAECs and HUVECs, it is important to optimize the coating concentration for both cell types.

doi:10.6342/NTU202600103

We used three ECM for testing: (i) Rat fibronectin (ii) human fibronectin (iii) matrigel (200x). Previous studies suggested using 10 – 30 μg/mL concentration of fibronectin is suitable for coating. Hence, we first used 10 μg/mL of fibronectin with varying time conditions for our testing. We wanted to test which conditions provided with most stable cell adhesion. First, we tested for HUVEC with following conditions:

Table 2. HUVEC coating testing conditions

Fibronectin (10 μL/mL)	Coating Time	Washing time
Rat	2 hrs	30 mins / overnight
Human	2 hrs	30 mins / overnight
Matrigel (200x)	2 hrs	overnight

As shown in Table 1, an important criterion for testing condition is washing time. Washing time suggests the maximum time the side channels were flushed with either noGF media or PBS to remove excess ECM. If not removed, the cells might attach to the extra ECM instead of the device and might flow away when connected to long channels.

We used no growth factor (noGF) media to wash the excess fibronectin. To understand the effect of washing time, we studied two conditions: (i) coated ECM/matrigel on side channels for 2 hrs one night before seeding, reconnected media to continue vasculogenesis and seeded the cells next day on side channels (ii) coated ECM/matrigel 2.5 hrs before seeding, washed with noGF media for 30 mins and then seeded the cells. Figure 5-3 shows the results of the three conditions after 2 hrs of seeding the cells on side channels (Day 0) and the next day (Day 1). Human fibronectin worked best for HUVEC attachment in both washing conditions (Figure 5-3 A and B). Matrigel also worked well for overnight washed devices. However, rat fibronectin worked better only if it was washed overnight with noGF media (Figure 5-3 A). When washed for 30 mins, the cells

doi:10.6342/NTU202600103

didn’t attach to the surface at all on Day 0 (Figure 5-3 B0) and mostly flow away from the pores on Day 1 (Figure 5-3 B1).

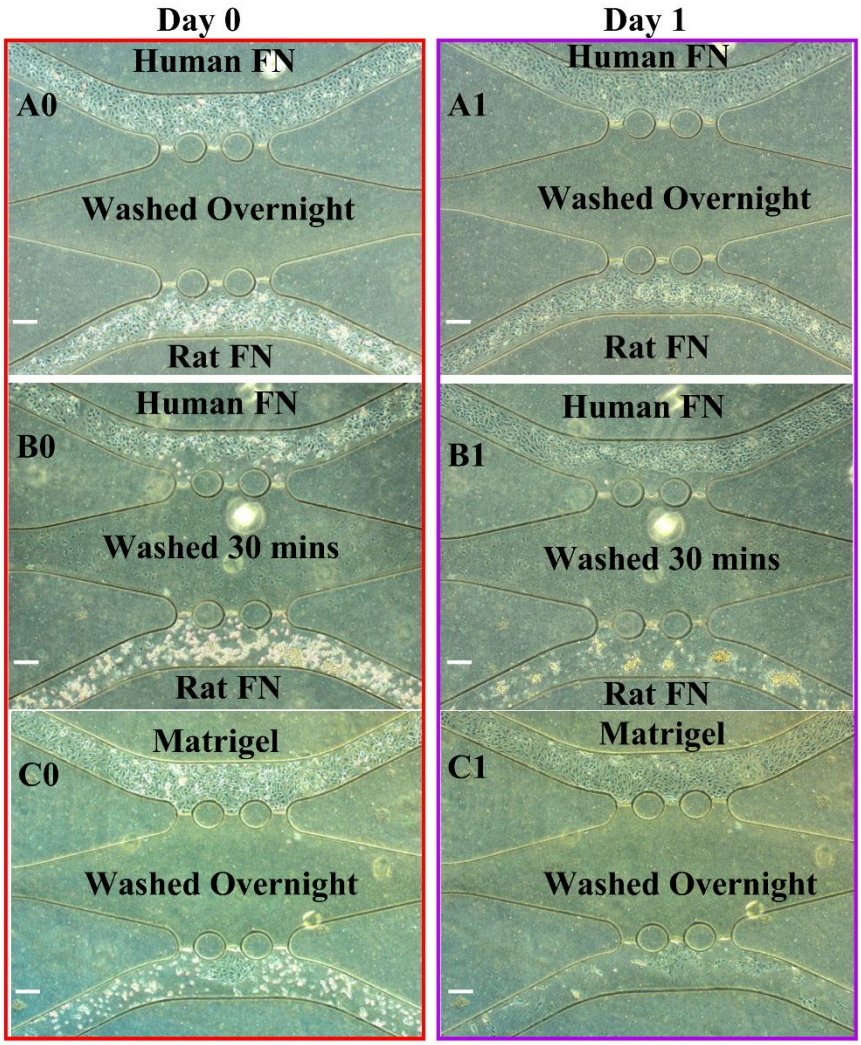

Figure 5-3 HUVEC coating optimization with (A) Rat fibronectin (10 μg/mL) (B) Human Fibronectin (10 μg/mL) and (C) Matrigel 200x

In the above scenario, we had used a relatively higher concentration of ECM coating (10 μg/mL). Additionally, both human and rat fibronectin (FN) coatings performed better with overnight washes compared to 30-minute washes. We hypothesized that the higher FN concentration required a longer flushing period to remove excess FN. Therefore, for the HUAEC coating test, we reduced the FN concentration and evaluated

doi:10.6342/NTU202600103

human FN coating by flushing with both PBS and noGF media. Table 3 summarizes the FN coating concentrations.

Table 3 HUAEC coating testing conditions

FN type	FN concentration	Washing medium
Human	2 μL/mL	PBS/nGF media
	4 μL/mL	PBS/nGF media

The side channels of two test devices were coated with two different concentrations of human FN for 2 hrs and washed with either PBS or noGF media for 30 mins. HUAECs were seeded (Day 0) and the images of both conditions were taken the next day (Day 1) as shown in Figure 5-4. As observed, HUAECs didn't attach well to the devices that was washed with noGF media. This could be due to the strong adherence of media to the FN that could potentially strip them off from the devices. However, flushing with PBS helped remove only the excess FN and allowed better attachment of HUAEC to the side channels as shown in Figure 5-4 B.

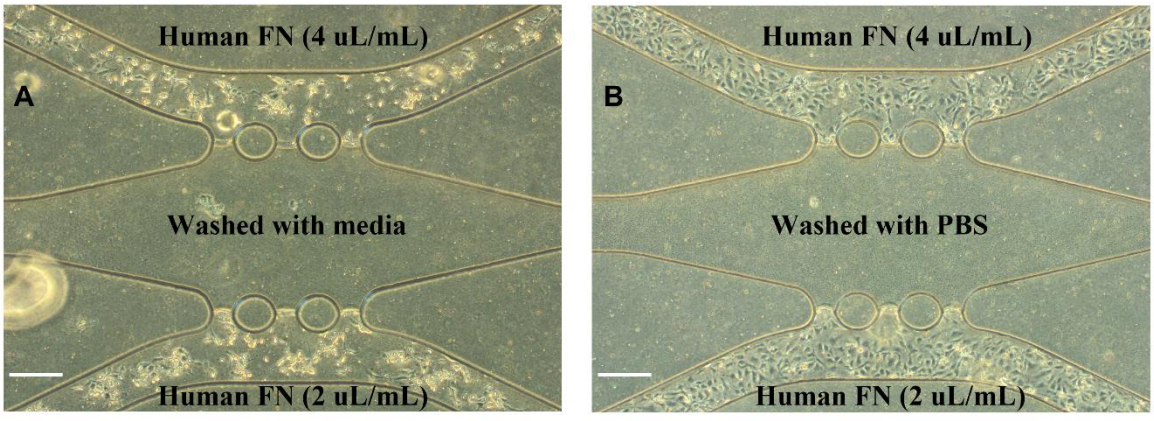

Figure 5-4 Day 1 images of Human FN at different concentrations washed with (A) noGF media (B) PBS

doi:10.6342/NTU202600103

After several additional tests, we obtained consistent results using rat FN at a concentration of 4 μL/mL with a 15-minute PBS flush. Therefore, our optimized ECM coating protocol involves coating with rat FN for 2 hours, followed by a 15-minute flush with warm PBS.

5.2 Developing arteriole-on-a-chip

5.2.1 Vasculogenesis and angiogenesis for developing primary plexus

As discussed before, our experimental plan consists of two parts: (i) diffusion and (ii) convection. Diffusion based system induces hypoxia and uses vasculogenesis and angiogenesis to develop perfusable vascular networks. After the developed MVNs are checked for successful perfusion, the devices are cultured in a convective system for inducing arteriogenesis to optimize and mature the MVNs for disease modelling and drug testing. In this section, we will describe diffusion system for inducing vasculogenesis and angiogenesis.

Using diffusion, we simulate the seeded cells to form the primary vascular network or vascular plexus. The system comprises of the microfluidic device connected to two symmetrical long channels as shown in figure 3.1. Briefly, HUAEC, HUSMC and NHLF are co-cultured in the central chamber in a fibrin gel. The experimental parameters are as mentioned in Table 4.

Table 4 Experimental parameters for developing arteriole-on-a-chip

Cell concentration (seeding)	Cell Ratio	Cell concentration (Lining)	O_2 Concentration	Device fixing

doi:10.6342/NTU202600103

2.0 E7 cells/mL	HUAEC:NHLF:HUSMC 2:2:0.5	5.0 E6 cells/mL	5%	Day 10

The cells are mixed in a fibrin gel and then loaded into the central chamber. To create the fibrin gel, the cells were first mixed in 15μL of fibrinogen (10mg/mL) and then quickly mixed with 4 μL of thrombin (5 U/mL). The final volume of cell is ~ 20 μL (19 μL of fibrin gel when mixed with cells become ~ 20 μL). After loading the cells in the AC, the device is kept in 20% O2/5% CO2 incubator for 6 hours. During this period, pipette tips were connected to the side channels, and HUAEC culture medium containing all growth factors was perfused through the device. After 6 hours, the pipette tips are replaced with symmetrical long channel devices (LCD) and HUAEC media is replaced with EGM-2 media without the growth factors VEGF and bFGF. To ensure continuous perfusion, the LCDs are connected to media reservoirs and a media height difference of 10 mmH_20 between the P_H and P_L was maintained for the static culture period. The entire setup is placed in a 5% O_2/ 5% CO_2 incubator to induce vasculogenesis for 4 days.

Intracellular vacuoles in HUAECs can be observed on Day 1 as shown in Figure 5-5 A. The intracellular vesicles fuse together to form the hollow vacuoles that later becomes the vascular lumen. After pre-lumen and vacuole formation, neighboring ECs align, connect and fuse their vacuoles together (Figure 5-5 B) to form endothelial tubes by Day 2. Figure 5-6 shows the development of vasculogenesis in a device from Day 2 to Day 5. By Day 4, the vascular tubes matured and form the primary vascular network within the gel. On Day 4, the side channels were seeded with HUAECs (5.0×10^6 cells/mL) to facilitate anastomosis with the pre-developed vascular network. As shown by the dotted lines in Figure 5-6 C, a confluent layer of HUAECs was observed along the side channels on Day

doi:10.6342/NTU202600103

5. Following cell seeding, the device was maintained under the diffusion culture system until Day 7, allowing the endothelial cells in the side channels to undergo angiogenic extension and establish connections with the existing microvascular network.

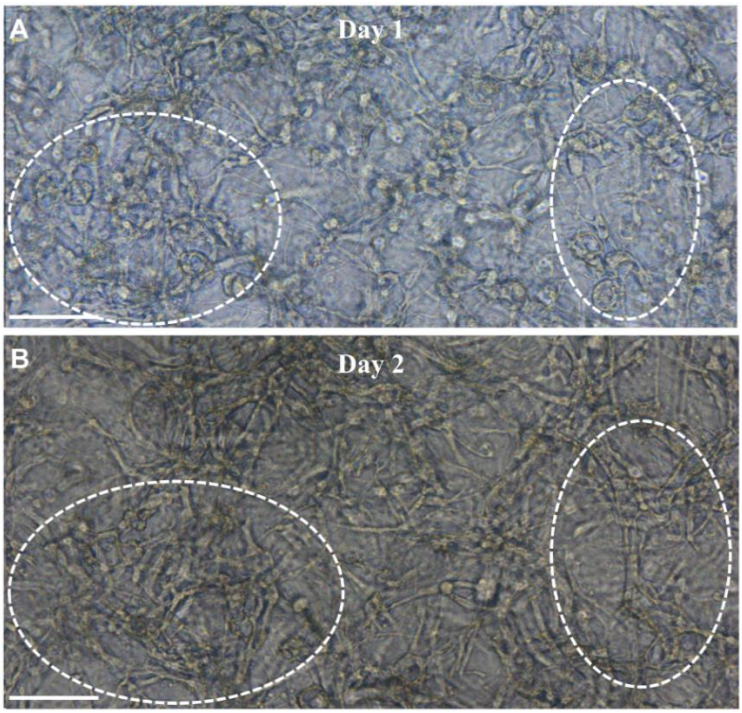

Figure 5-5 Initiation of vasculogenesis. (A) Formation of vacuoles on Day 1 (B) Fusion of vacuoles to form endothelial tubes. (scale bar = 50 μm)

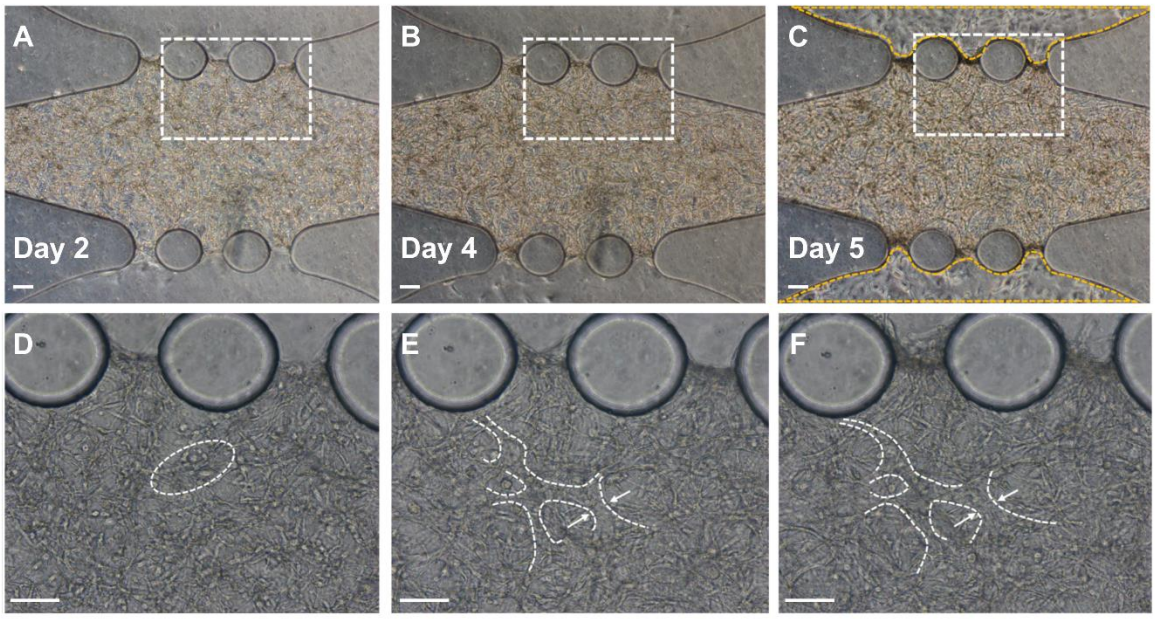

doi:10.6342/NTU202600103

Figure 5-6 Development of vasculogenesis in a device from (A) Day 2 (B) Day 4 and (C) Day 5. Enlarged images of selected regions from (D) Day 2 (E) Day 4 and (F) Day 5. Yellow dotted lines in (C) indicate seeding of cells on side channels for anastomosis. (scale bar = 100 μm)

5.2.2 Arteriogenesis for vascular network remodeling and optimization

On Day 7, the devices were checked for perfusability by flowing 70k Da FITC-dextran. Figure 5-7 A shows the FITC image of a device on Day 7. As observed, the FITC traced the path of perfusable vessels, revealing the primary plexus developed due to vasculogenesis. The connection of the device at the pore (white dotted circle) shows the point of anastomosis of the HUAECs lined on the side channels and the vessels inside the microchamber.

As successful connection was observed, we rocked the device in a rocker to induce arteriogenesis. Figure 5-7 A and B shows the development of the vessels due to the application of high oscillating flow for 48 hrs. We also observed intussusceptive angiogenesis in our devices. Small holes (shown by yellow dotted lines) in an undifferentiated primary plexus is observed in Figure 5-7 A represents the intraluminal pillar formed by the contact of opposing endothelial walls. After application of high oscillating flow for 24 hrs, the holes expanded and divided the lumen and formed clear vessel structures. In the next 24 hrs of applying high oscillating flow, the vessels elongated and became thinner, indicating vascular network optimization.

doi:10.6342/NTU202600103

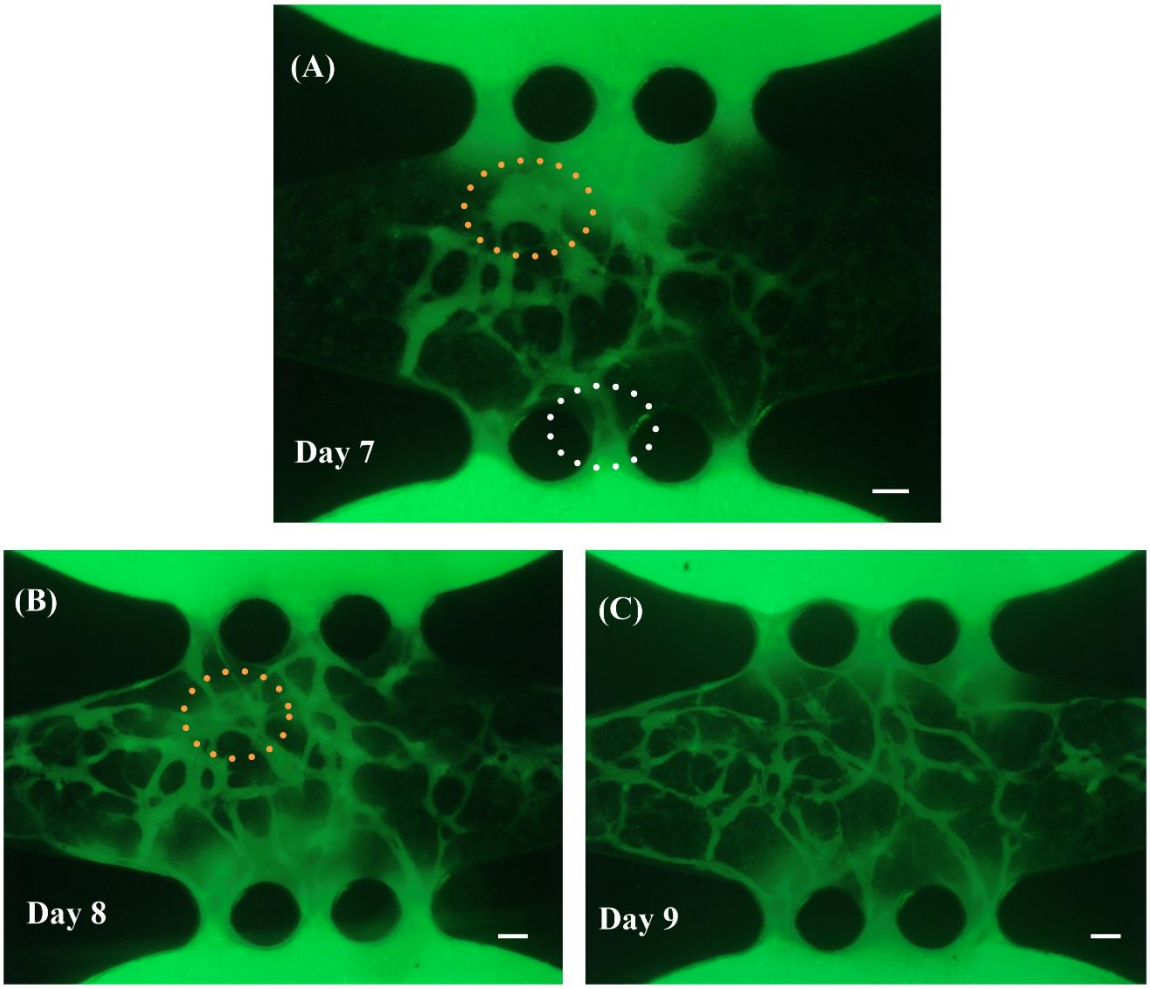

Figure 5-7 FITC Dextran test and arteriogenesis for high oscillating flow (A) FITC image for Day 7 before arteriogenesis. Vessel remodeling after (B) 24 hrs and (C) 48 hrs of oscillating flow. White dotted circle shows the anastomosis of side channel HUAEC to the MVN inside vessel network. Yellow dotted circle shows intussusceptive angiogenesis development.

For the next part, few images are partially reproduced from our published Lab on a chip paper [134]. We have obtained the necessary permission to reproduce in my dissertation and the certificate is attached in the appendix.

doi:10.6342/NTU202600103

5.3 Effect of oscillating shear stress on vascular perfusability and dynamic remodeling

Vessel perfusability is important in assessing the quality of the matured vascular networks. The sustenance of perfusable networks were studied for the above three conditionsTo investigate the effect of different levels of oscillatory flow on vessel perfusion, we examined three conditions: (i) static, (ii) low flow or low shear stress (LS), and (iii) high flow or high shear stress (HS). For the static condition, the devices were cultured in diffusion for the entire experiment without any flow inside the chamber. For the LS condition, the devices were cultured with pipette tips on the outlet and media height was adjusted so that the net pressure generated inside the chamber was around 82.37 Pa while rocking. For high oscillating flow, the media outlets were connected with long microchannels and the media height was adjusted so that the net pressure generated inside the chamber while rocking was around 785 Pa. The pressure created by high oscillating flow was around 9.53 times higher than low oscillating flow. Figure 5-8 shows the FITC images of devices cultured under different conditions for 48 hrs. The devices were checked for perfusability on Day 7 which was marked as investigating day 0 (ID0). The perfusable devices were cultured for 48 hrs (ID1 and ID2, respectively) and were checked for perfusion after every 24 hrs by flowing FITC.

Under static condition, the vessels were initially perfused on ID0 as shown in Figure 5-8 A. However, with the loss of flow, perfusion began to decline by ID1, and by ID2, the vessels had completely lost perfusability. For low flow condition, the initial vessel perfusion was limited (Figure 5-8 B). However, the application of low shear stress enhanced perfusion at ID1, and by ID2, vessel perfusion further improved, with interconnected vessels spanning from pore to pore across opposite sides. Over the rocking

doi:10.6342/NTU202600103

period, the vessel perfusability increased continuously with expanding the vascular network and perfusing previously imperfusable vessels. For high shear stress condition, the device perfusability and network connectivity increased on ID1 (Figure 5-8 C). New perfusable vessel segments were created as indicated by the white arrows. However, upon further application of shear stress of same magnitude, vessels remodeled to optimize the MVN. On ID2, regression of vessel segments were observed as indicated by the red arrows. The vessels that were thicker and connected directly to the pores (primary) remained perfused while the ones away from the pore and thinner (secondary) started regressing as shown in red. The regressing vessels are indicated by either imperfusability of the vessel segments or thinning of the diameters.

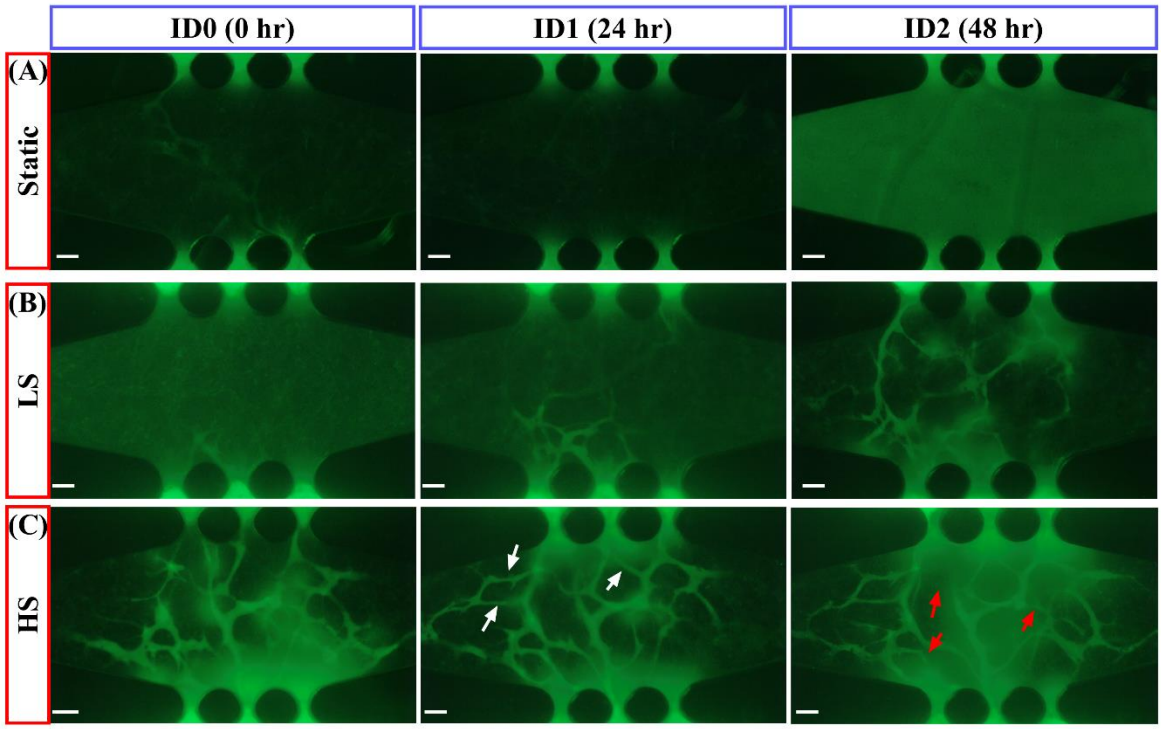

Figure 5-8 Fluorescent micrographs of the HUAEC vessels grown under (A) static, (B) low (LS) and (C) high (HS) oscillating flow on Day 7 (ID0), Day 8 (ID1) and Day 9 (ID2). ($n \geq 3$) (scale bar = 100 μm)

doi:10.6342/NTU202600103

Next, we quantified the vascular remodeling using FITC images by analyzing vessel parameters such as diameter, branch length, number of branches and branch points (nodes). As discussed above, the static condition lost perfusion on ID1. Hence, vessel parameters for static condition are calculated only on ID0. Figure 5-9 A shows the change in diameter of vessels over the 48 hrs. of inducing arteriogenesis. The median diameter for was 18 ± 5.3 μm for static condition on ID0. The median vessel diameter for LS condition was calculated as 22 ± 9.1 μm, 24 ± 9.5 μm and 23 ± 10.3 μm respectively for ID0, ID1 and ID2, respectively. The diameter didn't change significantly over the experimental period although marginal increment in diameter could be observed. Similarly, the median vessel length was calculated to be 77 ± 52.41 μm, 87 ± 76.65 μm and 101 ± 70.09 μm for ID0, ID1 and ID2, respectively (Figure 5-9 B). Although the vessel length didn't increase significantly over the experimental period, the vessel length was maximum on ID2 suggesting continuous exposure to low shear stress improves vascular connectivity and longevity. To further demonstrate the expansive effect of low shear stress on vessel perfusability, the number of branches and nodes was highest on ID2 compared to earlier time points. For HS condition, the diameter increased significantly increased from 18 ± 7.9 μm on ID0 to 25 ± 9.6 μm on ID1. On ID2, the diameter decreased insignificantly to 24 ± 10.03 μm. Vessel length didn't change significantly for any of the condition as shown in Figure 5-9 B and The median vessel length was 101 ± 63.5 μm, 88 ± 61.12 μm and 120 ± 64.9 μm for ID0, ID1 and ID2, respectively (Figure 5-9 B). Also, the number of perfusable branches and nodes were similar on ID0 and ID1 but decreased on ID2 as shown in Figure 5-9 B and D.

doi:10.6342/NTU202600103

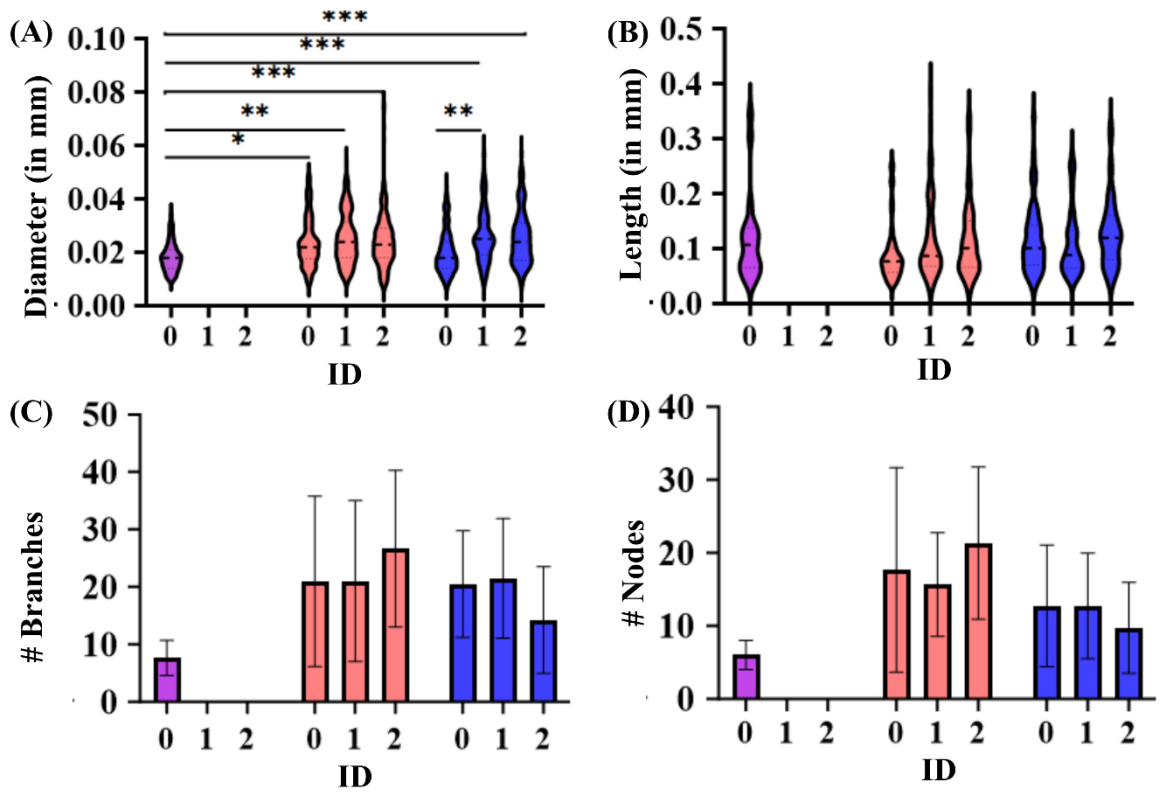

Figure 5-9 Comparison of vessel parameters such as vessel (A) diameter (B) length (C) number of branches and (D) number of nodes in control, low shear (LS) and high shear (HS) condition before rocking (ID0), after 24 hours (ID1) and 48 hours of rocking (ID2) ($n \geq 3$). (control = purple, LS = red, HS = blue) (measured vessel segments are 18, 50 and 37 for control, low shear and high shear conditions, respectively) [134]

As we observed that some vessels remain perfused while others regressed after application of high oscillating flow, we were curious to understand if the initial vessel diameters influenced this outcome. In smaller-diameter vessels, intraluminal shear stress tends to be higher, which could play a critical role in determining the long-term perfusability of the vessels. To investigate the effect of initial diameter on long-term vessel perfusability in high oscillating flow condition, we categorized the developed vessels into three categories: (i) vessels that were perfused on ID0 and lost perfusion on ID1 and ID2 ($ID_{0\text{-}0}$) (green) ((ii) vessels that were perfused on ID0 and ID1 and lost

doi:10.6342/NTU202600103

perfusion on ID2 (ID_{0-1}) (orange) and (iii) vessels that were perfused through ID0 to ID2 (ID_{0-2}) (purple). Figure 5-10 A shows the comparison of vessel diameters for the above conditions. We compared the diameter change of the vessels every 24 hrs until their perfusion period. The ID0 diameter for ID_{0-0}, ID_{0-1} and ID_{0-2} conditions were calculated as 14.8 ± 4.5 μm, 17.2 ± 4.9 μm and 21.0 ± 7.9 μm, respectively. As predicted, median diameter of ID_{0-0} condition is smallest among all three before introducing high oscillating flow. The median diameter in ID_{0-2} condition was significantly higher among all three conditions on ID0. This is crucial observation suggesting the importance of larger diameter in sustaining high shear stress due to high oscillating flow and allowing the vessels to remodel accordingly. This observation is further fortified in subsequent analysis on ID1 and ID2. The median diameter of ID_{0-1} on ID1 (19.3 ± 5.8 μm) was significantly less than ID_{0-2} (27.5 ± 9.7μm). Another interesting observation is the change in diameter on ID1 is also dependent on the initial diameter on ID0. For ID_{0-1}, the diameter increased by 12.2 % whereas for ID_{0-2}, the diameter increased by 30.9% on ID1. This suggest that vessels with larger initial diameters undergo greater expansion upon exposure to high oscillating flow.

Next, we calculated the diameter enlargement ratio to understand how continuous high flow affects diameter changes. We calculated the enlargement ratio for ID_{0-2} and quantified the ratio of diameter change between the following groups: ID1 to ID0 (ID1/ID0), ID2 to ID0 (ID2/ID0) and ID2 to ID1 (ID2/ID1). The results are shown in Figure 5-10 B. We observed that the average diameter enlargement ratio is highest on ID2/ID0 (1.83 ± 0.96) followed by ID1/ID0 (1.51 ± 0.83). However, this ratio is only 1.23 ± 0.28 for ID2/ID1. We believe a sudden transition from static to flow conditions on ID0 resulted in a pronounced increase in vessel diameter, likely due to elevated intraluminal shear stress. By contrast, on ID2, the vessels had already undergone adaptive remodeling

doi:10.6342/NTU202600103

on ID1 in response to sustained high shear stress. As a result, the same magnitude of flow produced comparatively lower shear forces within the already dilated vessels, leading to a reduced diameter enlargement ratio (ID2/ID1). These findings indicate that exposure to oscillatory flow during the initial 24 hours promotes shear stress–mediated vascular remodeling, facilitating the development of a more mature and stable microvascular network that undergoes limited structural alterations upon subsequent flow stimulation.

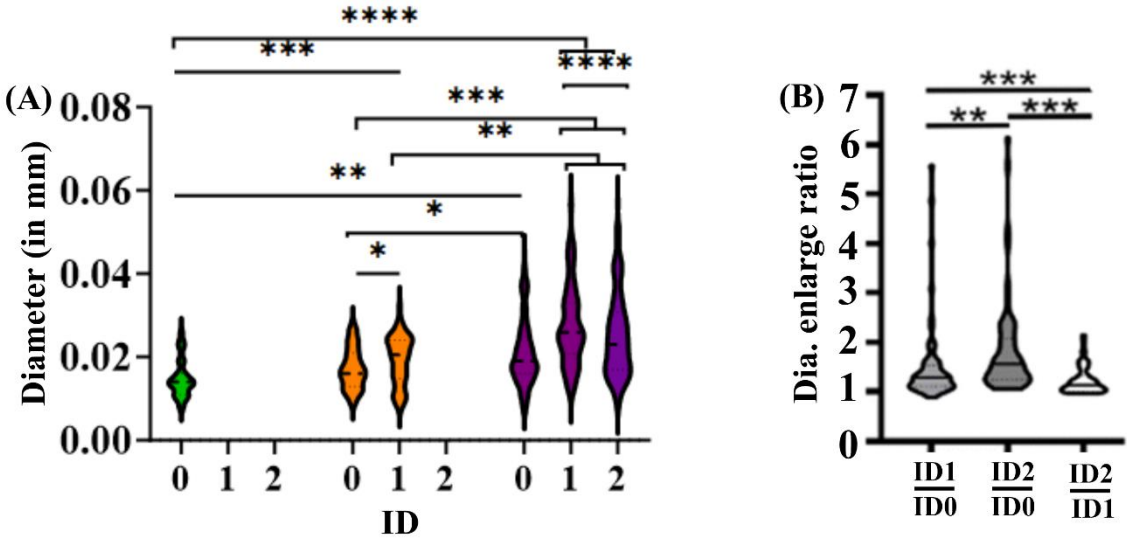

Figure 5-10 (A) Comparison of vessel diameters that were perfused on ID0 ($ID_{0\text{-}0}$) (green), from ID0 to ID1 ($ID_{0\text{-}1}$) (orange) and from ID0 to ID2 ($ID_{0\text{-}2}$) (purple). (B) Diameter enlargement ratio between ID1 to ID0 (ID1/ID0), ID2 to ID0 (ID2/ID0) and ID2 to ID1 (ID2/ID1) [134]

5.4 Analyzing arteriole network in response to different shear stress condition

The primary aim of our research is to develop an *in vitro* arteriole-like structure that closely mimics the architecture of human arterioles. As the *in vivo* arteries are

doi:10.6342/NTU202600103

characterized by co-localization of HUAECs and HUSMCs (Figure 5-11 D), we wanted to determine whether our developed MVNs also had similar organization. We immunostained the fixed arterioles to visualize vessel structures, SMCs, basement membrane (BM) and nucleus. Figure 5-11 A shows a representative section of an arteriole stained for these parameters. To clearly observe the fluorescent staining and their spatial organization, a merged 3D surface reconstruction of vessels and SMCs was created using IMARIS as shown in Figure 5-11B. The images verify that vessels, SMCs and BM are co-localized and have recapitulated the *in vivo* arteriole structure. To further examine the co-localization sequence, a cross-section image was captured along the white dotted lines as shown in Figure 5-11 C. The image distinctly reveals the characteristic layered organization of an arteriole, with HUAECs forming the central lumen (red), surrounded by a layer of HUSMCs (green), and enveloped by the collagen membrane (purple). These findings confirm that our model successfully reproduces the structural hierarchy of human arterioles *in vitro*.

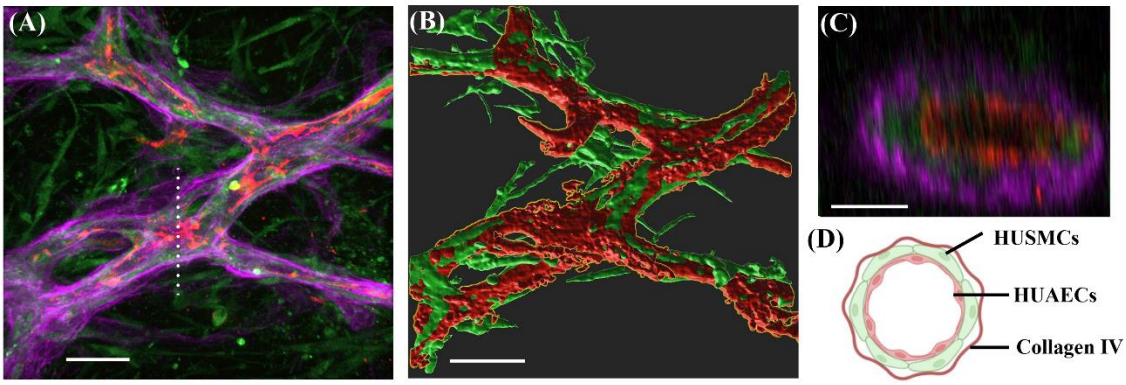

Figure 5-11 Architecture of a developed MVN (A) Immunofluorescent images of a section of an arteriole. (B) 3D merged surface image of vessel. (scale bar = 40 μm) (C) cross-section image of the white dotted line showing inner HUAEC layer (red), surrounded by HUSMC (green) layer and collagen membrane (purple) (scale bar = 10

doi:10.6342/NTU202600103

μm). (D) Schematic representation of a cross section of a typical human artery (image drawn in Biorender.com) (red = CD31, green = calponin and purple = collagen IV) [134]

Next, we aimed to understand how varying flow conditions influence the formation of final vascular network. Figure 5-12 shows the fluorescent images and 3D renderings of representative devices cultured in static, LS and HS conditions. Comparing the vessel structures in all three conditions, we observe that the vessels in static condition are fragmented and sparsely connected as shown in Figure 5-12 A. This observation is similar to the FITC cases where we observed loss in perfusion in static condition due to the absence of flow. The vessels in LS condition are comparatively longer and thinner. As we FITC images showed expansive remodeling for LS condition, we believe application of shear stress elongated the vessels for better connection and perfusability. HS condition had the thickest vessel structures that were well connected demonstrating the ability of high shear stress in optimizing and maturing MVNs.

We investigated the co-localization ability of SMCs in all three conditions. The 3D surface rendering sprovided a better visualization of the co-localization orientation of HUAEC-SMCs as shown in Figure 5-12 D-F. Intuitively, we can observe that the SMCs in static condition are unevenly co-localized and exhibit limited interaction with thr developed MVN. In fact, except few sections, other sections of the MVNs lacked SMC coverage. In contrast, for LS condition, HUAEC-SMC co-localization improved, several sections of the MVN lacked SMC adherence. HS condition showed highest co-localization with maximum vessels enveloped by SMCs. In fact, the SMC density is also visibly higher in HS condition as shown in Figure 5-12 F. These observations suggests that in the absence of flow or low flow rate condition, the developed MVN resembles capillary-like structure instead of arterioles as they lack the structural hierarchy. Conversely, high flow condition promotes the formation of structureal hierarchy as

doi:10.6342/NTU202600103

observed in an actual arteriole-like vessel, indicating the role of magnitude of flow in directing arteriole formation.

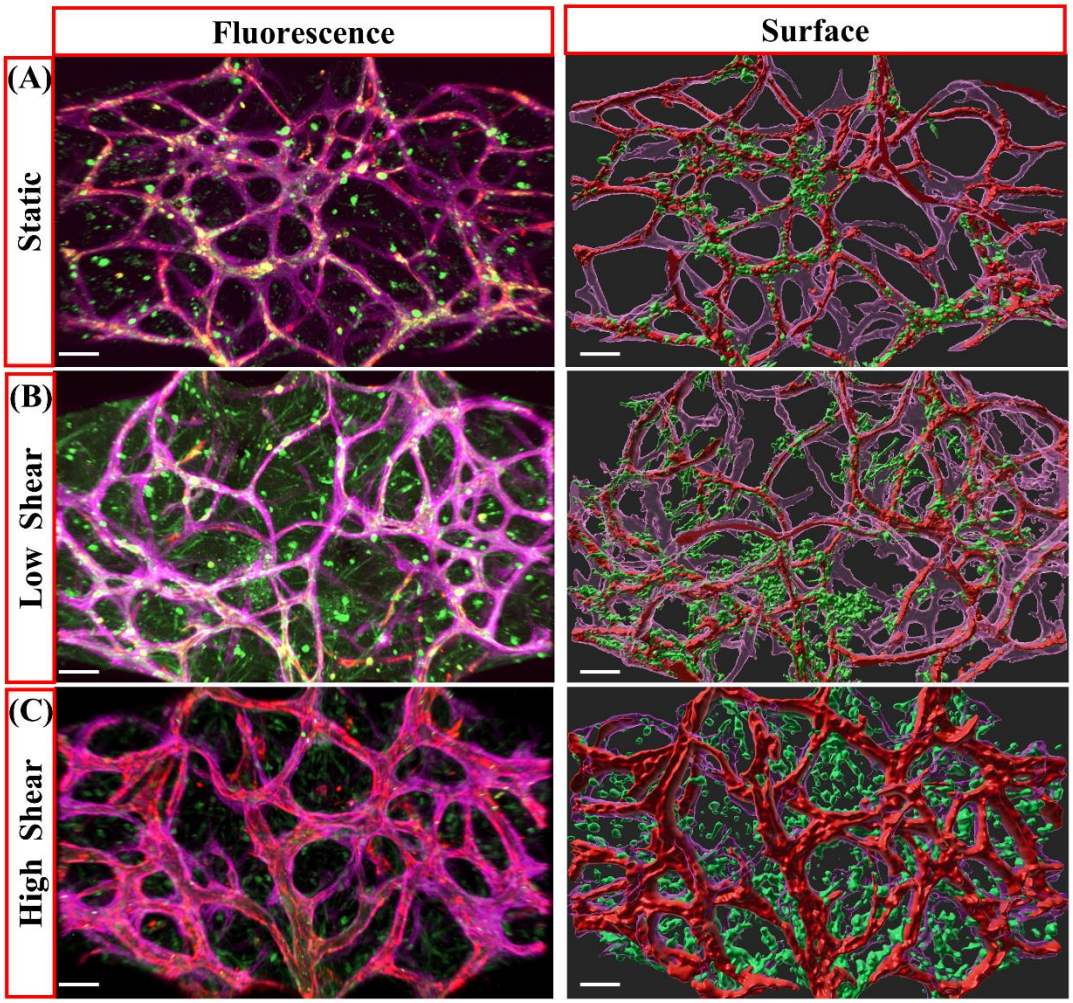

Figure 5-12 Fluorescent images and 3D surface images of vessels developed in (A) static (B) LS and (HS) condition (scale bar = 100 μm) red = CD31, purple = collagen IV, green = calponin ($n \geq 3$) [134]

We quantified several vessel parameters such as SMC, vessel and collagen area and vessel diameter in all three condition to differentiate quantifiably the development of MVNs due to varying flow conditions as shown in Figure 5-13. The measured median vessel diameters are 16 ± 8.05 μm, 14 ± 5.53 μm and 28 ± 10.8 μm for static, LS and HS conditions, respectively (Figure 5-13 A). Also, the average vessel area is highest for HS

doi:10.6342/NTU202600103

condition (46.69 ± 8.42%) followed by LS (20.27 ± 4.11%) and static (13.74 ± 2.6%) conditions. As expected, the HUAEC parameters like vessel area and diameter are significantly higher in HS condition than both LS and static condition. However, interestingly, the diameter in LS condition is lower than static condition. This could be due to the elongation effect induced by low flow that promotes increased vascular connectivity and perfusability. As previously observed, vessels formed initially due to vasculogenesis and angiogenesis represent primary plexus, which is a loosely organized network with limited structure. Application of flow simulates the vessels to interconnect and move towards the perfusion pores, leading to the formation of longer, thinner and more interconnected vascular network.

Similar to vessel area, SMC and basement membrane area were also significantly higher in HS condition compared to static and LS condition. Average SMC area for static, LS and HS condition was calculated as 27.5% ± 5.5%, 33.1% ± 8.8% and 55.4% ± 7.9%. Interestingly, average BM area was comparable for all conditions and were measured as 52.6% ± 5.2% and LS 56.6 ± 3.2% and 67.1 ± 11.7 % for static, LS and HS conditions, respectively.

doi:10.6342/NTU202600103

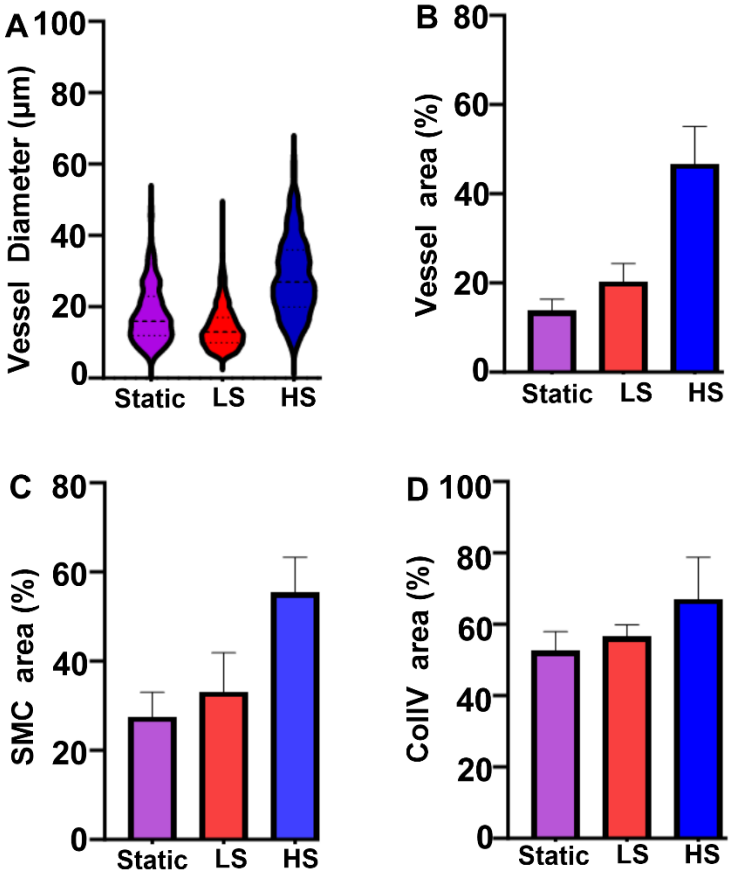

Figure 5-13 Quantification of vessel parameters for static, low shear (LS) and high shear (HS) conditions. Total number of measured vessel segments are 68, 115 and 112 for static, low shear and high shear conditions, respectively. ($n \geq 3$) [134]

From our previous observations, low flow stimulation promoted the expansion of the vascular network, whereas high flow conditions optimized the network architecture within the perfusable device. However, in some cases, even after the vascuologenesis and angiogenesis phases, many devices remained imperfusable on Day 7. Although the vessel-like strcutures could be visible via bright field imaging, perfusion with FITC dye revealed no continuous or connected lumens**.** To address this, we wanted to check if the application of low/high shear stress could influence these imperfusable networks. In such devices, flow primarily bypasses the vascular lumens and instead travels through the surrounding matrix, generating interstitial flow rather than intraluminal flow. Therefore,

doi:10.6342/NTU202600103

we aimed to determine whether the magnitude of interstitial flow could affect vessel perfusability.

Figure 5-14 A shows a device on Day 7 with no perfusable vascular network. We rocked the device in low flow condition for 24 hrs and perfused the device with FITC on Day 8 as shown in Figure 5-14 B. Within 24 hrs of application of low shear stress, we observed few perfused vessels. Some devices needed prolonged application of low flow (48 -72 hrs) to become perfusable. However, introduction of high flow to imperfusable devices did not restore vessel connectivity or improved perfusion. These examples highlight the importance of magnitude of flow in improving perfusability.

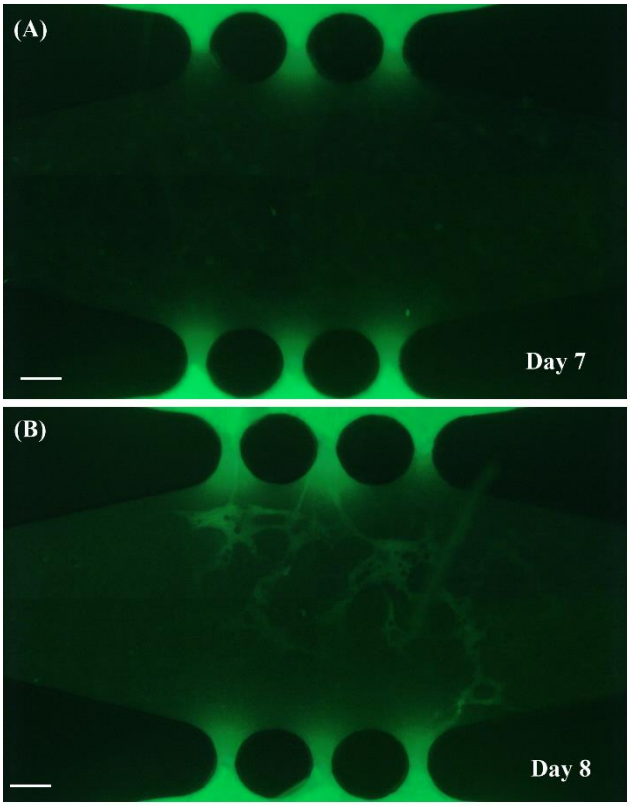

Figure 5-14 Application of low shear stress stimulates perfusion. (A) Device with no perfusion on Day 7 and perfusable vessels appear on (B) Day 8 (scale bar = 100 μm) [134]

doi:10.6342/NTU202600103

5.5 Analyzing vascular network remodeling from initial vascular plexus using vessels and basement membrane

As discussed above, BM represents the initial vascular blueprint outlining the early vascular network developed due to vasculogenesis and angiogenesis. Quantification of BM area in Figure 5-13 also showed no significant difference among the three conditions. However, the final vessel network in all three conditions were significantly different with HS condition having highest vessel area. Hence, we aimed to investigate the extent to which initial structure was remodeled to form the final vascular network in response to varying oscillating flow. Figure 5-15 shows the immunofluorescent images of vessels (CD31) and BM (purple) for all three conditions. IMARIS surface module was used to generate the 3D surface renderings and visualize the spatial correlation between vessels and BM for static, LS and HS conditions as shown in Figure 5-15 C, F and I, respectively.

Immunofluorescent images clearly show that the vessels and BMs are co-localized. However, the vessel networks appear thinner than the BM network. The analysis of surface images (Figure 5-15 C – F) reveal that the vessel network forms a subset within the broader BM network. In fact, several regions within the BM network appear vacant without any vessels inside them (white arrows). Furthermore, other areas in the network have partially regressed vessels where the remnants of the vessel are still enclosed within the BM sleeve. These empty BM sleeves, also known as “ghost” membranes, represent regions that were previously occupied by vessels that have undergone regression. Hence, the appearance of “ghost” membranes are a proof of vessel regression and reflects the remodeling and maturation of the final network in response to various stimuli. In our study, since varying flow conditions were the only stimulus introduced, the resulting vascular architecture represents the remodeling of the initial

doi:10.6342/NTU202600103

network driven by shear stress. Understanding vascular remodeling from the initial network due to the application of shear stress is crucial to elucidate the optimal flow condition for optimizing vascular networks while minimizing aberrant vessel regression. Moreover, vessel regression is a common phenomenon observed *in vivo* and is essential for pruning secondary and redundant vessels. The ability of our device to successfully recapitulate this demonstrates its potential as an *in vitro* platform for studying flow-mediated vascular remodeling.

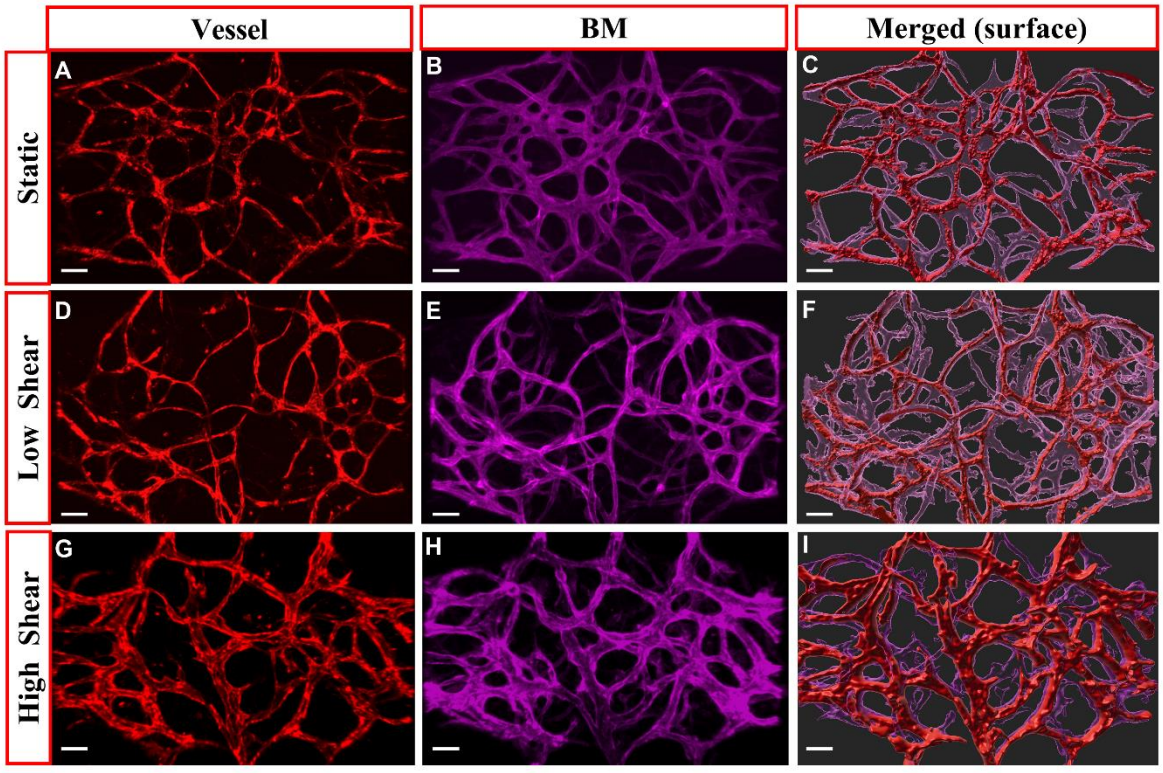

Figure 5-15 Vascular remodeling analysis using vessels and basement membrane (BM). Vessels (CD31), BM (Col IV) and merged surface images of (A-C) static, (D-F) LS and (G-I) HS conditions. ($n \geq 3$) (Scale bar = 100 μm) [134]

Figure 5-16 A shows the statistical analysis of calculated diameter for vessels and BM networks. As expected, BM network had significantly larger diameter than final vessel network across all the three conditions. The median diameters of vessels under static, LS

doi:10.6342/NTU202600103

and HS conditions were 16 ± 8.0 μm, 13 ± 5.9 μm and 27 ± 10.8 μm whereas the diameter of their corresponding BM networks were 23 ± 10 μm, 20 ± 6.5 μm and 32 ± 11.9 μm, respectively. The results corroborate with our previous observation with FITC imaging where high oscillating flow promoted enlargement of diameters. However, the comparison of area coverage is interesting. For both static and LS condition, the vessel area was significantly lesser than BM area. The area coverage in static condition reduced from 52.69 ± 5.29 % to 13.57 ± 2.59% whereas for LS condition it reduced from 56.62 ± 2.81 % to 20.27 ± 3.56%. However, for HS condition the vessel area (46.69 ± 6.87%) did not significantly reduce from the BM area (67.05 ± 9.61%). This is a very crucial observation highlighting the significance of high flow conditions in maintaining and stabilizing the initial vascular networks.

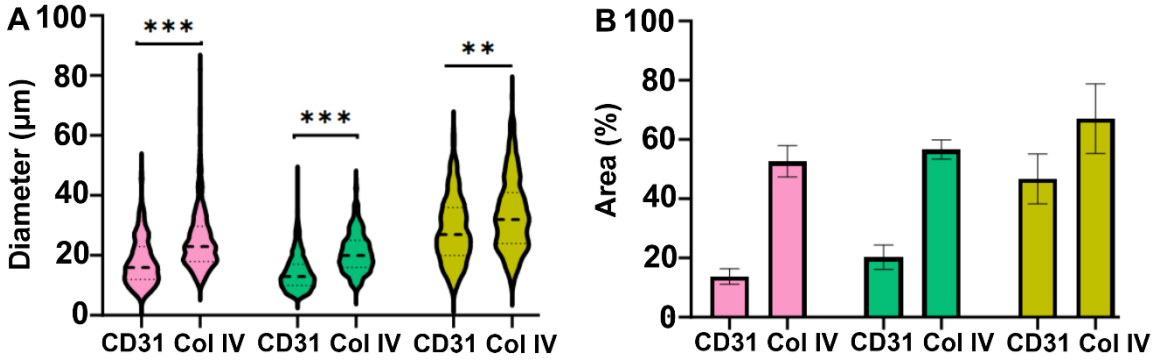

Figure 5-16 Comparison of (A) diameter and (B) area percentage for vessels and basement membrane networks. Total number of measured vessel segments are 68, 115 and 112 for static, low shear and high shear conditions, respectively. (n ≥ 3) [134]

5.6 Finite element analysis of shear stress inside MVN

From previous sections, we observed that the initial vascular network undergoes extensive remodeling to form the final vascular network depending on the magnitude of applied shear stress. The primary and final MVNs are identified by BM and CD31

doi:10.6342/NTU202600103

immunofluorescent stains, respectively. We were curious how the shear stress and flow rate changed within the MVN as the network remodeled from initial to final state. To achieve this, we first introduced blood flow into a matured vascular network, as shown in

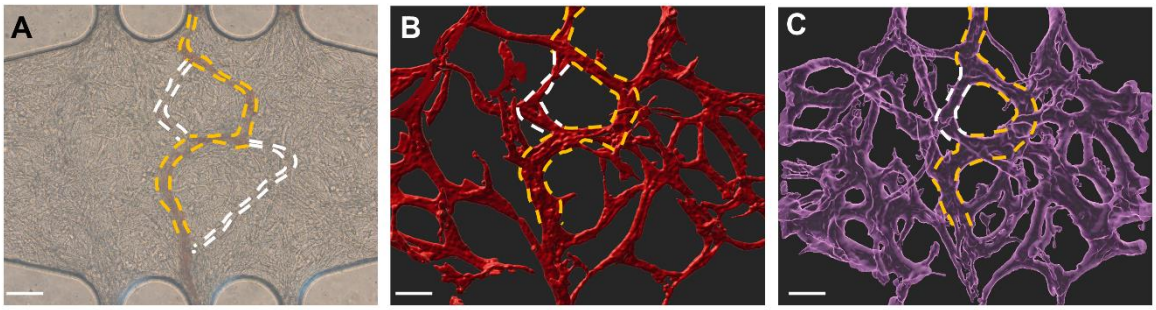

A. This device was rocked in high oscillating flow condition and hence the final MVN is remodeled as per the high shear stress inside the arterioles. We chose this particular arteriole as we can observe blood flow in both primary and secondary arterioles. At the entrance, we can observe the blood flow is divided into two parts: (A) left part with lesser flow (white dashed line) and (B) right part with substantial flow (yellow dashed line). Next to the right arteriole, another secondary arteriole was observed (white dashed line) with little flow. For analysis, we focused only on the upper region of the network and designated the right and left arterioles as the primary and secondary vessels, respectively.

To model flow inside the arterioles, we first obtained the 3D surface renderings of vessel and BM structures as shown in Figure 5-17 A and B, respectively. Although the BM structure may appear wider due to the contribution of an intermediate smooth muscle layer, it still provides a reliable approximation of the initial vascular architecture. This geometry is sufficient for evaluating how fluid shear stress and velocity through the networks are altered when the MVNs are exposed to high oscillatory flow. To evaluate the shear stress and velocity inside the selected segments, we trimmed the sections as shown in dotted lines using 3D slicer [135]. The trimmed section was imported into COMSOL multiphysics for obtaining the finite element analysis.

doi:10.6342/NTU202600103

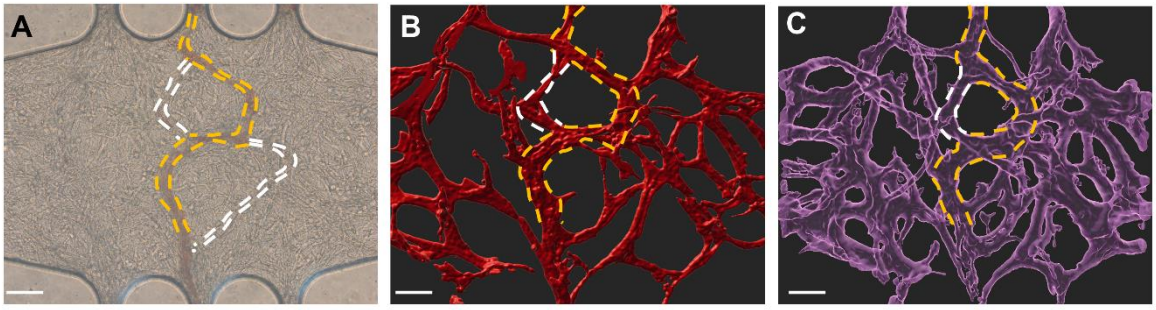

Figure 5-17 (A) Blood flow inside a developed arteriole. Yellow and white dashed lines represent primary and secondary arterioles, respectively. 3D renderings of (B) vessel structures and (C) BM structures. (scale bar = 100 μm) [134]

Figure 5-18 C and D shows the trimmed vascular and BM network, respectively. As this device was subjected to high oscillating flow, we set the input pressure as 785 Pa and the output pressure as 0 Pa. Figure 5-18 A and B shows the shear stress and velocity profiles of the vessel segment and Figure 5-18 C and D show the similar profiles for BM network. The BM networks have generally broader diameter than vessel networks. Hence, both velocity and shear stress profiles are lower in BM segments than their vessel counter parts. Among the primary and secondary segments, it can be intuitively observed that the velocity and shear stress profiles for secondary segment appear higher than the primary network in both cases likely due to their smaller diameters. Hence, thinner structures have larger velocity and shear stress profiles than wider structures.

doi:10.6342/NTU202600103

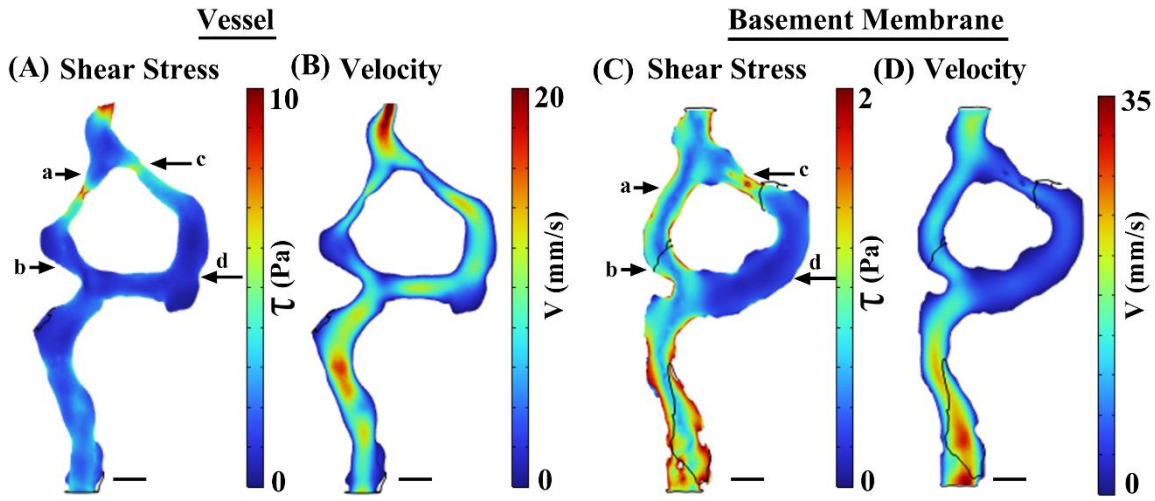

Figure 5-18 Velocity and shear stress profiles inside various points of vessels and BM network. Scale bar = 50 μm (A-D) and, 100 μm (E-H)

To quantify the velocity and shear stress profiles, the primary and secondary vessels were sectioned into eight slices from c → d and a → b, respectively, with each slice spaced 25 μm apart. The BM network was also sectioned in the same manner, with the slices spaced 20 μm apart. We calculated the average velocity and wall shear stress at the defined segments as shown in Figure 5-19. For the vessels, the wall shear stress ranged between 1.42 Pa - 8.13 Pa in secondary vessel and 1.49 Pa – 3.84 Pa for the primary vessel (Figure 5-19 B). Similarly, the fluid velocity ranged from 1.95 mm/s – 9.35 mm/s for secondary vessel and 2.9 mm/s – 5.68 mm/s in primary vessel as shown in Figure 5-19 A. Similarly, for BM structures, the wall shear stress ranged between 0.49 Pa – 1.5 Pa and 0.21 Pa – 0.66 Pa in secondary and primary BM segment, respectively as shown in Figure 5-19 D. The velocity profile was also higher in secondary collagen (2.7 mm/s – 5.5 mm/s) as compared to primary collagen (1.7 mm/s – 4.6 mm/s). As discussed above, the velocity and wall shear stress in the vessel network were higher than in the collagen network, as the latter, serving as the initial, larger-lumen scaffold, gradually remodeled into the more

doi:10.6342/NTU202600103

refined and compact final vascular network. We also calculated the total volume flow rate within those networks as shown in Figure 5-19 E. As expected, the flow rate in larger collagen networks was higher (0.0748 μL s−1) than the vessel network (0.04 μL s−1). These observations give crucial insight into vascular remodeling due to application of high shear stress.

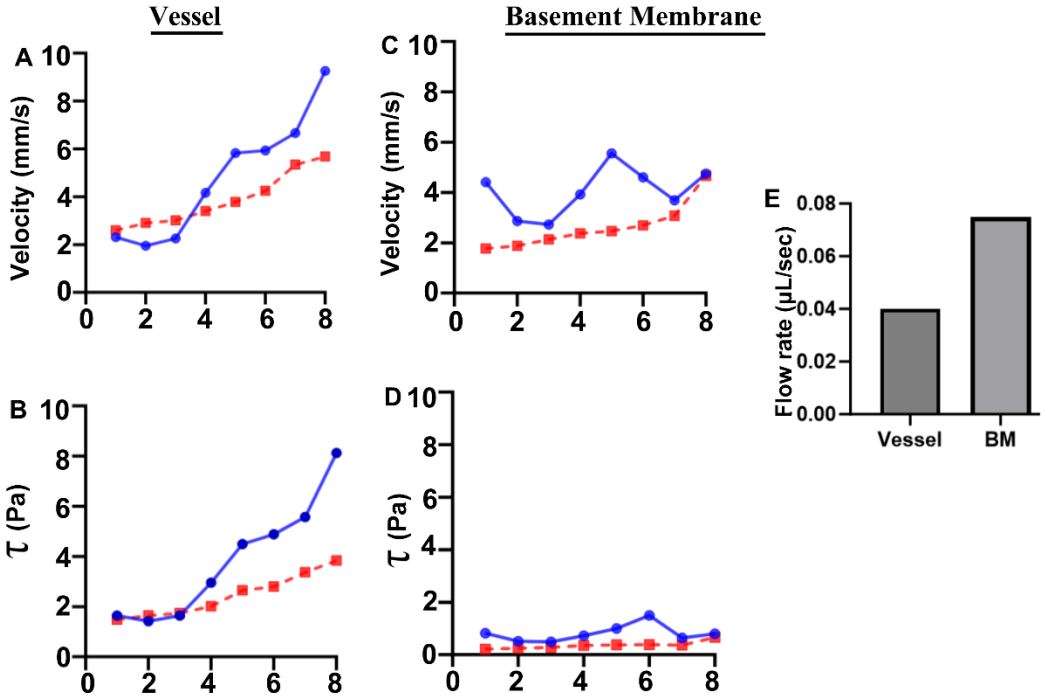

Figure 5-19 Quantification of average velocity and shear stress at defined regions. Velocity and shear stress profiles for (A-B) vessel network and (C-D) BM network. (E) Total flow rate in vessel and BM network [134]

5.7 Vascular Functionality

5.7.1 Vasomotion in response to different dosage of dopamine

We next evaluated the contractile functionality of the engineered MVNs by assessing their response to a vasostimulant. Dopamine was selected as it is a well-established vasoactive molecule with both vasodilatory and vasoconstrictive effects [136]. Previous

doi:10.6342/NTU202600103

studies have demonstrated that low concentrations of dopamine induce vessel dilation, whereas higher concentrations trigger vessel constriction [137]. This response is due to the difference in receptors dopamine act upon at different concentrations. At low concentrations, dopamine primarily activates dopaminergic (D1) receptors, leading to relaxation of vascular smooth muscle and resulting in vasodilation. As the dose increases to a moderate range, dopamine begins to activate β-adrenergic receptors, producing mixed or transitional responses, where some vessels may dilate while others show minimal change. At high concentrations, dopamine predominantly stimulates α-adrenergic receptors, causing vascular smooth muscle contraction and leading to vasoconstriction [138], [139], [140]. This dose-dependent behavior makes dopamine a suitable stimulant for assessing the dynamic contractile ability of our MVNs.

Most existing studies on dopamine dosage effects have been performed in animal models, where dopamine is directly infused into the bloodstream. As our devices have micro-vessels, we introduced smaller dosage to test vessel movement. We tried three dosage of dopamine in our developed MVN: (i) 0.5 mg/mL (ii) 1 mg/mL and (iii) 2 mg/mL. Because the MVNs are dense and highly complex, only vessel segments that exhibited clear and distinguishable vasomotion were selected for analysis. Figure 5-20 A shows the FITC image of a representative arteriolar segment before dopamine treatment. Figure 5-20 B-D presents time-lapse images following dopamine treatment at 10 sec, 20 sec and 30 sec for dopamine concentrations of 0.5 mg/mL, 1 mg/mL and 2 mg/mL, respectively. To quantify the changes in diameter, the percentage change at 10 sec, 20 sec and 30 sec was calculated relative to the initial diameter. The corresponding plot is show in Figure 5-20 E. At a concentration of 0.5 mg/mL, the vessels predominantly dilated with an average diameter increase of 6.68 ± 3.3% relative to the base diameter. When the concentration was increased to 1 mg/mL, the vessels still dilated but the magnitude was

doi:10.6342/NTU202600103

reduced, resulting in an average dilation of 4.92 ± 3.8%. In contrast, for 2mg/mL, dopamine induced vasoconstriction where the vessels diameter decreased from the initial state with an average constriction of -8.22 ± 4.9%. We observed that for 0.5 mg/mL the vasodilation was obvious and consistently greater than vessel dilation at 1 mg/mL. Although 1 mg/mL still promoted vessel dilation in many vessels, we observed no measurable dilation or even mild constriction indicating the transitional effect of the intermediate range. Hence, the lower dose promotes vasodilation whereas intermediary range shows transitional response from dilation to constriction. At highest studied dose of 2 mg/mL, all the vessels showed consistent vasoconstriction, with a reduction of diameter across all segments. In fact after few more seconds, there was complete loss of perfusion. These bi-phasic response of vessels to different concentrations of dopamine corroborates with previously reported *in vivo* studies. Taken together, these results demonstrate that our arteriole-on-a-chip platform can reproduce the dose-dependent vasomotor behavior of dopamine and can be used for drug-response studies involving vasomotion.

doi:10.6342/NTU202600103

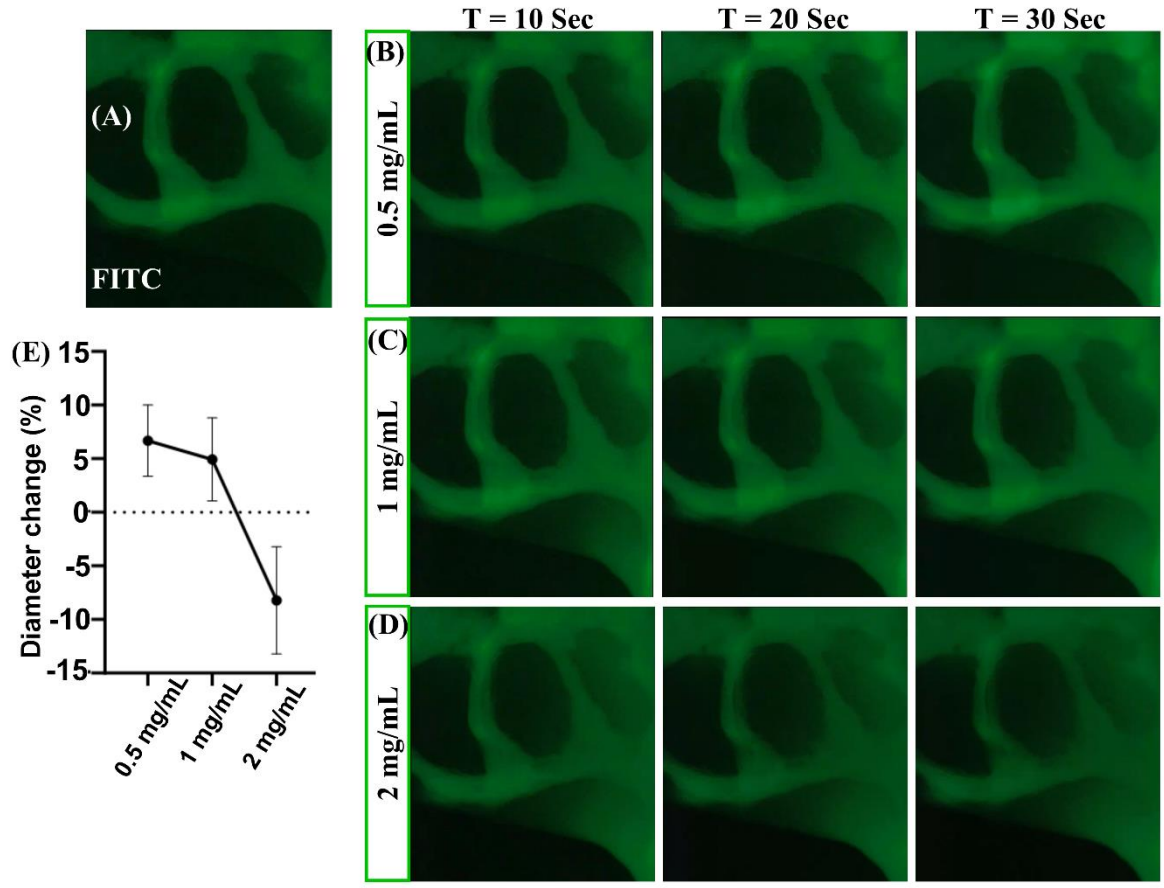

Figure 5-20 Effective of dopamine dosage on HUAEC+NHLF+HUSMC co-culture (A) FITC image of a section of an MVN before dopamine treatment. Time lapse images of dopamine at (B) 0.5 mg/mL (C) 1 mg/mL and (D) 2 mg/mL. (E) Statistical analysis in percentage change in vessel diameter after introducing dopamine at different concentrations. Four different sections demonstrating vasomotion were analyzed for quantification).

Studies have shown that dopamine's vasostimulatory effect is sensed by the receptors expressed in the vascular smooth muscle cells. So, we hypothesized that MVN lacking an SMC layers would be unable to exhibit vasomotion in response to dopamine. To test this hypothesis, we generated MVNs composed of only HUAEC+NHLF co-cultured at a 1:1 ratio (2E7 cells/mL) to obtain vessels without the SMC layer.

doi:10.6342/NTU202600103

We perfused dopamine at the same concentrations used in the previous experiments and monitored the vessels. As expected, no measurable vasomotion was observed at any dosage of dopamine (Figure 2-2Figure 5-21 A-C), confirming that SMC layers is the primary mediator of dopamine-induced vasomotion in blood vessels.

However, despite loss of vasomotion, we observed complete loss of perfusion within 10 seconds of perfusion at highest concentration of 2 mg/mL (Figure 5-21 C). For HUAEC+NHLF+HUSMC MVNs, this response happened after 30 seconds of perfusion. This suggests that, perfusion loss is mediated by the response of endothelial cells and diameter change happens due to the responses of smooth muscle cells.

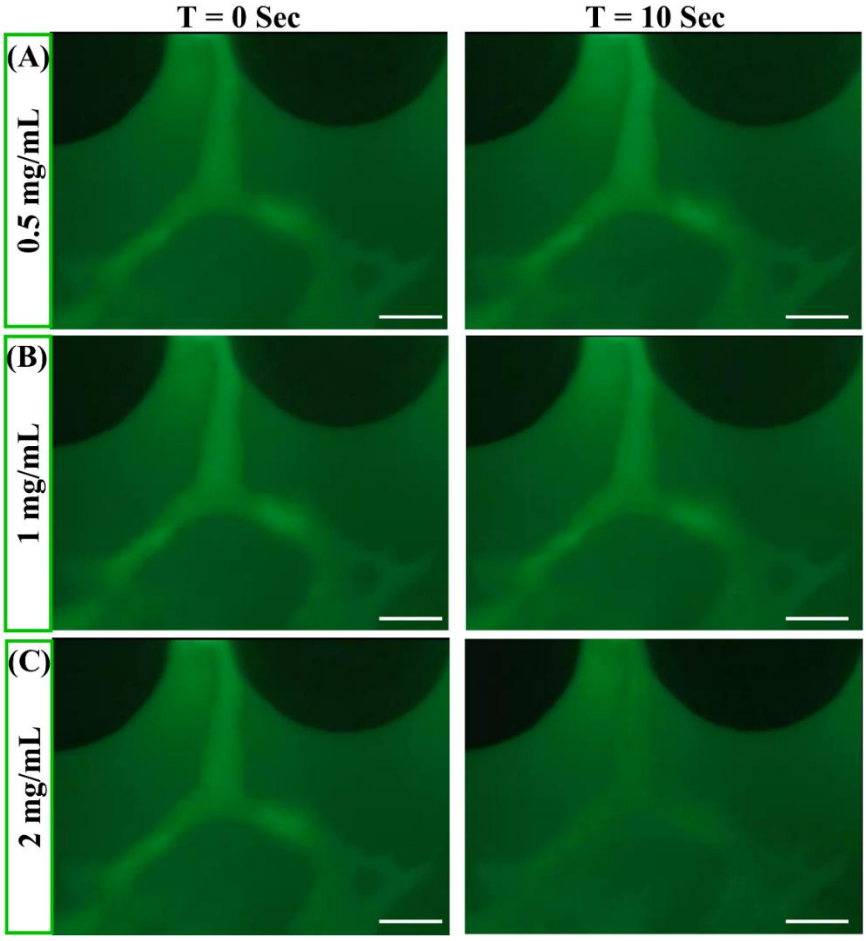

doi:10.6342/NTU202600103

Figure 5-21 Effective of dopamine dosage on HUAEC+NHLF co-culture. Time-lapse images of dopamine at (A) 0.5 mg/mL (B) 1 mg/mL and (C) 2 mg/mL. (Scale bar = 50 μm) [134]

5.7.2 Nitric Oxide (NO) release in response to high shear stress

Studies have confirmed that vascular NO production is modulated by shear stress. High shear stress stimulates eNOS activation that subsequently converts L-arginine to nitric oxide [19]. This nitric oxide is important for maintaining vascular homoeostasis by promoting vasodilation so that EC can maintain their quiescent stage and prevent occurrence of thrombosis and atherosclerosis. As we observed diameter change in the MVNs when subjected to high shear stress, we hypothesized that NO release might have played an important role. Therefore, we wanted to verify if the NO levels were higher in high flow devices than in control devices.

We immunostained both control and high flow device with NO-sensitive fluorescent probe, DAF-FM after device fixation. An important note here is DAF-FM has a significantly short half-life and its fluorescence signal to diminish substantially following fixation. Despite this limitation, we observed a clear and reproducible difference in DAF-FM fluorescence intensity between the static and high-shear devices even after fixation. This qualitative difference suggests a persistent disparity in nitric oxide–associated signaling between the two conditions. Given the constraints of DAF-FM stability post-fixation, the present results are presented to highlight the the impact of shear stress on endothelial nitric oxide signaling, rather than quantitative assessment.

Figure 5-22 A and B show basement membrane and NO detection staining in control and high shear devices, respectively. Clearly, the fluorescence intensity in high shear devices are much higher than control devices suggesting elevated release of NO due to high flow

doi:10.6342/NTU202600103

condition. This confirms that our MVNs exhibit physiologically relevant responses, similar to *in vivo* behavior, where vessels exposed to high shear stress release greater amounts of NO compared with low-flow conditions.

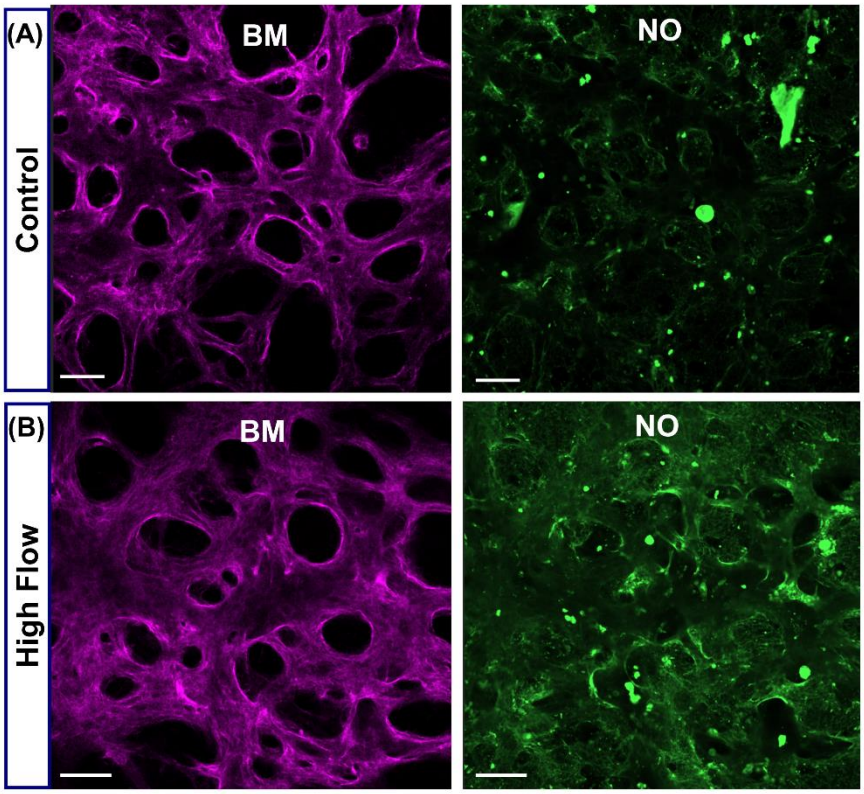

Figure 5-22 Nitric oxide (NO) detection in (A) control (B) high flow devices (scale bar = 70 μm). (purple = collagen IV, green = DAF-FM diacetate)

Next, we wanted to check the spatial distribution of NO production in high shear device. shows NO levels in a segment of an MVN subjected to high flow. As indicated by the white arrow, NO production is elevated along only one wall of the vessel, while other regions show minimal signal. This suggests that, although the entire microchamber experiences high flow, shear stress is not uniformly distributed across the MVN. This could be due to variations in vessel diameter and local flow velocity that create uneven shear environments. Thus, our experiment not only recapitulates shear-induced NO production but also reveals which regions of the MVN experience higher shear stress.

doi:10.6342/NTU202600103

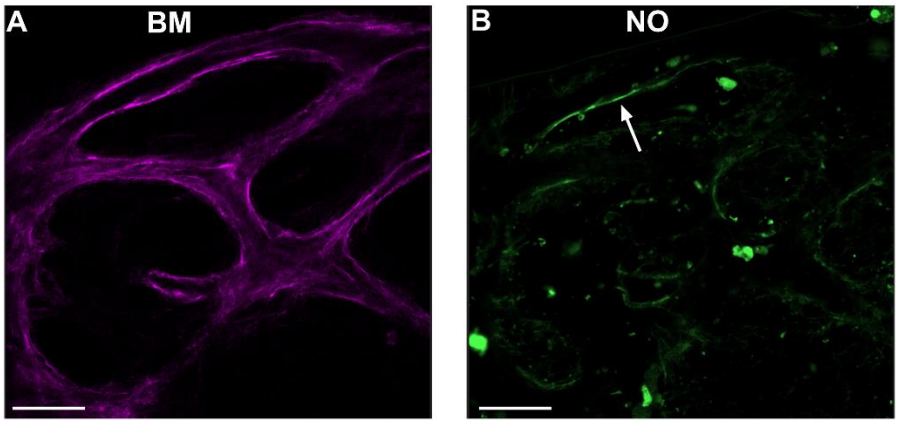

Figure 5-23 No distribution in a high shear device stained with (A) basement membrane (B) NO. The white arrow shows elevated high NO production in a segment. NO production is not uniform throughout the device. (scale bar = 50 μm)

5.8 Arterial Disease Modeling

5.8.1 Thrombosis

Thrombosis is the precursor to many complicated cardiovascular diseases. Many researchers have developed thrombosis *in vitro* [141]. These systems help researchers test antithrombotic drugs, understand clotting mechanisms, and study how shear forces influence thrombosis. Most thrombotic models are developed on single endothelial layer and lack the structural complexity of a real blood vessel. Hence, although these models can replicate isolate mechanism, they cannot recapture how the structural complexity and cell-cell interaction influence thrombosis/thrombolysis. Hence, we aim to induce thrombosis in our multicellular arteriole-on-a-chip to develop physiologically relevant model in an arteriole-like structure.

We first developed a mature and fully perfusable MVN by subjecting the network to high-shear arteriogenesis conditions, ensuring robust co-localization of HUAECs and HUSMCs and the formation of an arteriole-like structure. To initiate thrombosis, it was

doi:10.6342/NTU202600103

necessary to activate the endothelial layer and stimulate the release of von Willebrand factor (vWF). So, we perfused 50 ng/mL phorbol 12-myristate 13-acetate (PMA) in EGM-2 media for 30 mins. After stimulation, the excess PMA was removed using PBS and then whole human blood was perfused for 1 hour. Thrombosis is a rapid process with the clot formation time happening in few minutes. However, as we aimed for immunostaining the thrombus, we wanted to form a stable clot that would not displace during subsequent washing and device fixation steps.

Figure 5-24 A shows the confocal image of multiple clots formed within the developed MVN following PMA stimulation and blood perfusion. Figure 5-24 B - D present enlarged confocal images of the highlighted white box from figure A showing basement membrane, vWF and platelets, respectively. We stained BM instead of vessels as the platelets and vessels had overlapping fluorescent spectra, making it impossible to distinguish them. As BM is deposited by the ECs, staining BM could represent the indirect EC structures surrounding the vWF release sites.

The release of abundant vWF within the vessels proves that stimulation with PMA effectively damaged the endothelial cells and triggered the release of vWF. Platelets from the perfused blood adhered to these vWFs and formed multiple clots at different sites. To better visualize the clot formation, we rendered 3D surface images of BM, vWF and platelets as shown in Figure 5-24 E. The widespread release of vWF from various parts of the vessels suggests the perfusion of PMA throughout the MVN. However, blood could only flow through certain wider sections of the MVN. Thus, for any kind of blood related experiments, it is important to have wider vessels to accommodate the blood cells and maintain perfusion. Also, we observed the secondary/narrower sections of the MVN has more accumulation of vWF, possibly due to reduced PMA flow velocity through these sections. Platelets aggregation are clearly found either within vWF-rich segments or to

doi:10.6342/NTU202600103

the periphery of released vWF deposits. To further confirm thrombus formation is due to vWF-platelet interaction, we imaged a cross section of a clot as shown in Figure 5-24 F. The spatial orientation shows the cross linking of vWF and platelets cluster, demonstrating vWF is the primary mediator of clot formation.

Next, we wanted to verify if the release of vWF is influenced by the PMA activation of the endothelial cells. Hence, we immunostained vWF in a control device that was not subjected to PMA perfusion. Figure 5-25 A and B show vWF immunostain in a control and PMA stimulated device, respectively. In control environment, the vWF staining is barely recognizable as they are still present inside the Weibel-Palade bodies of the endothelial cells [24]. This suggest that in control device, ECs are healthy and don't secrete much vWF. However, in the PMA stimulated device, the vWF staining is quite distinct and traces the lining of the vessel structure. This suggests that PMA stimulation damaged the endothelial cells and released the stored vWF.

Next, we calculated the density and coverage of triggered platelet adhesion to vWF in the vessels perfused with blood. The platelet adhesion density was 1.7×10^4 platelets/mm^2 and the surface area coverage was around 28%. Quantitative assays in flow systems have shown platelet deposition surface coverage exceeding 15% under high shear stressin the presence of vWF [142]. Another *in vivo* study reported platelet adhesion density of 2.5×10^4 platelets/mm^2 after stimulation of mouse venules with a calcium ionophore (A23187) that enhanced the release of vWF [143]. These data align with the observed platelet adhesion density and coverage area we report for vWF-mediated adhesion in our model.

doi:10.6342/NTU202600103

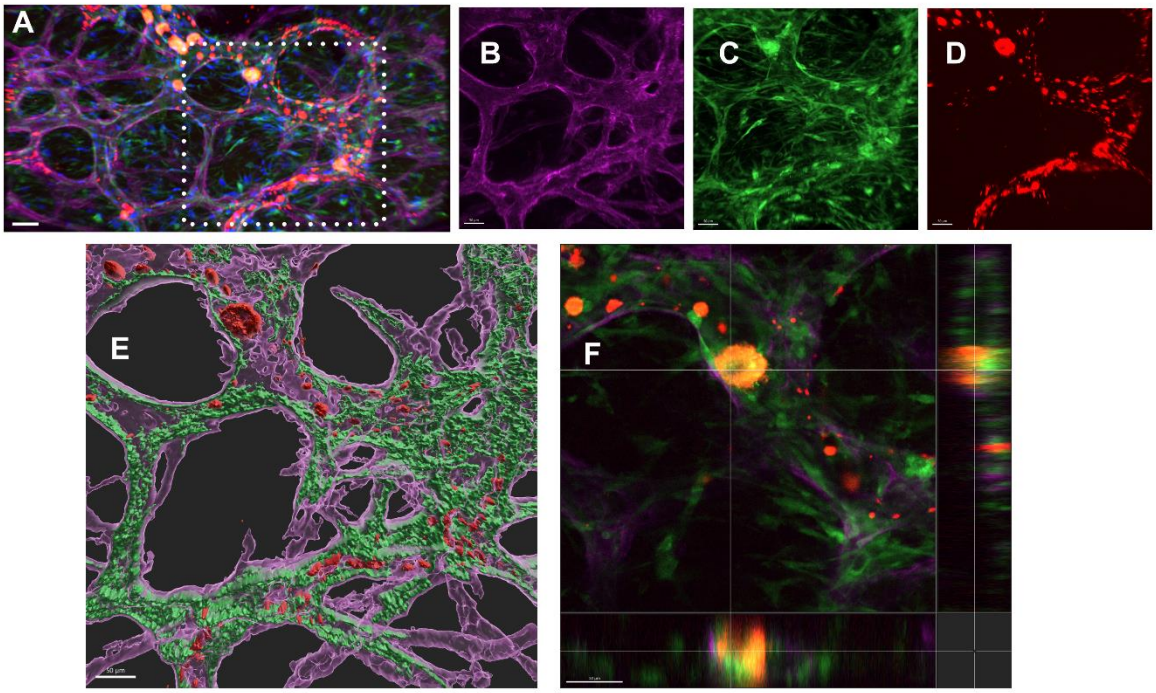

Figure 5-24 Development of thrombosis on arteriole-on-a-chip platform. (A) Fluorescent micrograph of thrombosis developed in an arterial MVN (scale bar = 100 μm). Enlarged images of white dashed box from (A) showing (B) basement membrane (C) released vWF (D) platelets adhered to blood vessel. (E) IMARIS surface renderings of basement membrane, vWF and platelets. (F) Cross-section image of a thrombus showing platelet-vWF accumulation. (scale bar = 50 μm) [134]

doi:10.6342/NTU202600103

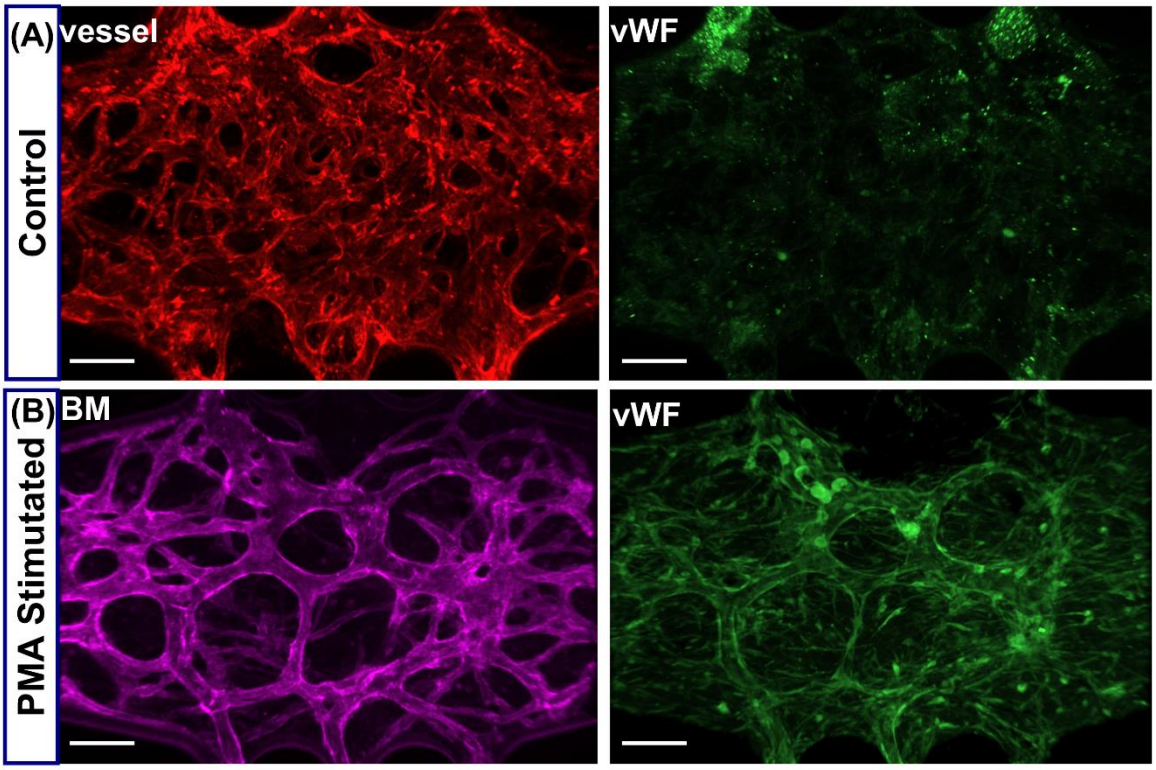

Figure 5-25 Release of vWF in (A) Control MVN (B) PMA stimulated MVN (scale bar = 150 μm)

5.8.2 Atherosclerosis

Effect of TMAO in causing atherosclerosis has been studied on 2D EC monocultures where isolated platelets and macrophages on static co-cultures show that TMAO can activate inflammatory signaling, alter barrier function and upregulate macrophage foam-cell pathways [28], [144]. Microfluidic and 3D cultures examine the flow dependent endothelial response and immune cell recruitment but lack the true in vivo geometry of an arteriole and whole blood perfusion. This limits the understanding of multicellular level interaction during early atherosclerosis events, which could provide mechanistic insight and guide drug development for better efficacy. Hence, we aimed to recapitulate the early atherosclerosis events in our platform to evaluate its ability to reproduce the underlying mechanism. The early events of atherosclerosis are marked by endothelial

doi:10.6342/NTU202600103

dysfunction that increases endothelial permeability and upregulates adhesion molecules such as VCAM-1, ICAM-1 and E-Selectin. Monocytes and T-cells are recruited to the inflamed endothelium via these adhesion molecules and subsequently transmigrate into the intima and differentiate into macrophages [25].

We first developed matured arteriole MVN by subjecting a perfusable device to high shear stress ensuring that the developed network recapitulated the three-layered vessel structure. Next, we perfused TMAO (200 μM) for 2 hours to model early atherosclerosis. After 2 hrs, excess TMAO was removed using PBS. Next, whole blood was perfused through the stimulated MVNs for 1 hr. Post perfusion, the devices were washed with PBS and then proceeded for fixation and immunostaining. The MVNs were immunostained for leukocytes, vessels and nucleus to visualize adhesion of leukocytes to the inflamed vessels.

Figure 5-26 A shows the fluorescent image of a matured MVN where blood was perfused post stimulation with TMAO. Figure 5-26 B shows the merged fluorescent image of vessels and nucleus. As observed, leukocytes are trapped at four distinct locations within the MVN as labeled i, ii, iii and iv. Sections i and ii show relatively low leukocyte adhesion, with three and one leukocyte, respectively.

Figure 5-26 C and D show the enlarged vessel and merged images of sections iii and iv, which exhibited higher leukocyte adhesion. Specifically, section iii and iv have 33 and 21 trapped leukocytes, respectively. Notably, these vessel segments are narrower compared to the other sections of the MVN and are closer to the perfusion port. Due to the proximity to the inlet, these segments experience frequent blood flow compared to other segments. Based on these observations, we hypothesize the combination of narrow

doi:10.6342/NTU202600103

vessel diameter and continuous perfusion increased leukocyte-endithelium interactions in these regions, thereby enhancing the probability of leukocyte adhesion.

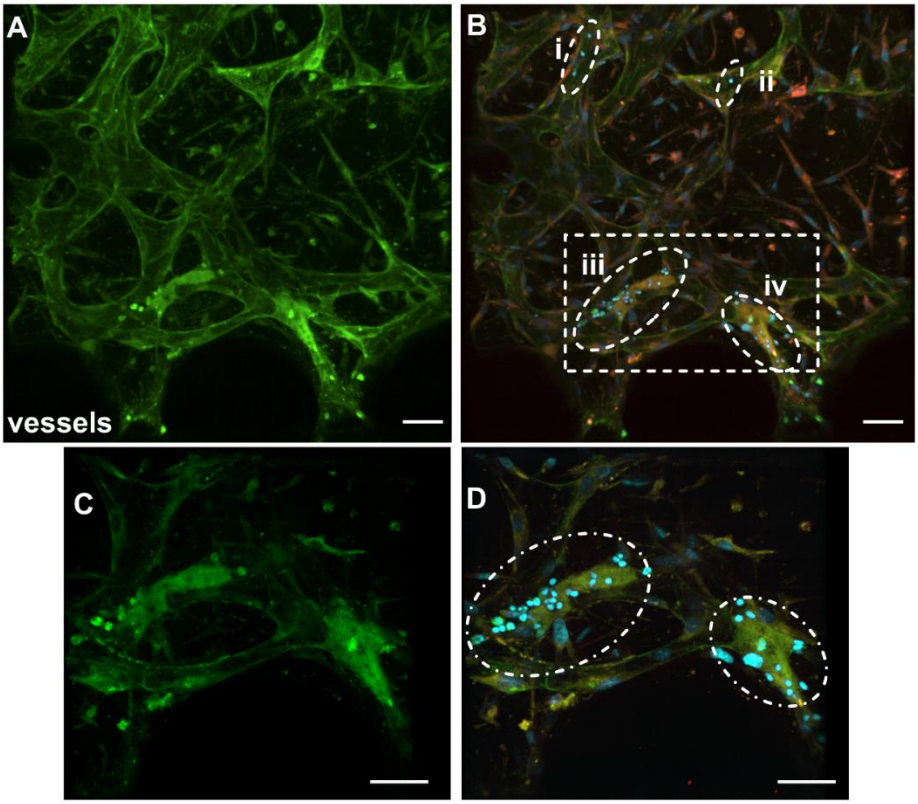

Figure 5-26 Atherosclerosis-on-a-chip development. Immunofluorescent staining of (A) vessels (B) leukocytes (C) merged image of vessels, leukocytes and nucleus (scale bar = 50 μm)

doi:10.6342/NTU202600103

6. Discussion

In this study, we have successfully developed a method to co-culture three primary human cell types in a microfluidic device to obtain a self-assembled, and matured and functional arteriole network. The key innovation of this work is the first integration of primary HUAECs and HUSMCs to form an arteriolar network that faithfully mimics in vivo structural organization, coupled with the reproduction of dynamic vascular remodeling driven by physiologically relevant oscillatory flow.

Many studies have successfully developed self-assembled vascular networks and investigated the role of flow in vessel formation [112], [145], [146], [147], [148]. However, the focus have primarily been on HUVEC-HLF co-cultures or tri-cultures involving brain endothelial cells, pericytes, and astrocytes. Also, they use static interstitial flow in these models that occurs over millimeter-scale gradients. In our study, we employed vasculogenesis and angiogenesis to guide HUAECs, NHLFs and HUSMCs into forming perfused vascular network. To implement both mechanisms, the devices were cultured in hypoxic condition. The method to induce hypoxia is previously reported by the corresponding author of this paper, Dr. Hsu [95]. Hypoxia in the AoC device was achieved in three ways: (i) the device was placed on a PMMA layer that blocked the exchange of gas through bottom, (ii) the PDMS device was thick enough to block the exchange of gas through the environment [149], and (iii) the entire setup was placed in 5% O_2 incubator. This ensured that oxygen was primarily supplied via the side channels, effectively creating a hypoxic microenvironment within the culture chamber.

Next, we applied continuosus oscillatory flow to the perfused vessels that increased intraluminal shear stress. The arteriogenic process observed in our study contrasts with previously reported interstitial flow-driven HMVEC vessel growth, which relied on convective flow within the interstitial space [145], [146], [147]. The studies

doi:10.6342/NTU202600103

focused mostly on the importance of interstitial flow in angiogenesis or diameter change while ours focused on remodeling and vessel maturation. Our results reveal a direct relationship between applied flow magnitude and vessel remodeling, highlighting the importance of hemodynamic forces in vascular adaptation. In the absence of flow, devices cultured under static condition showed progressive loss of perfusion in previously perfused vessels (Figure 5-8 A). At a low shear stress (~ 83 Pa), expansive vascular remodeling is observed, characterized by increased number of perfused vessel segments without significant change in vessel diameter (Figure 5-8 B). Interestingly, low shear stress promoted the perfusion of previously non-perfused vessels, emphasizing shear stress as a key regulator of vessel perfusion. At high shear stress (785 Pa), both expansive and regressive vascular remodeling was observed. In the first 24 hrs, significantly diameter of larger vessels increased significantly whereas smaller vessels regressed. Over the next 24 hours, secondary vessels continued to regress and vessel diameters of perfused vessels increased marginally (Figure 5-8 C). This critical observation highlights the temporal sensitivity of vascular remodeling to shear stress magnitude. The abrupt application of high shear stress triggered rapid network remodeling, after which the network optimized according to the hydrodynamic environment. A previous study examined how endothelial cells regulate vascular remodeling in response to fluid shear stress, focusing on the "shear-stress set point" that governs endothelial mechanoadaptation. [150]. The study demonstrated that endothelial cells (ECs) from different organs have different ranges of shear stress at which they function optimally—referred to as their "shear-stress set point." These set points vary according to the tissue-specific hemodynamic environment. The authors further identified VEGFR3 expression levels as a key molecular determinant of the set point. Experimentally, they showed that upregulating VEGFR3 lowers the shear-stress set point, whereas reducing VEGFR3

doi:10.6342/NTU202600103

expression elevates it. Shear stresses below the set point induce inward (constrictive) remodeling characterized by vessel narrowing, whereas shear stresses above the set point trigger outward (expansive) remodeling aimed at restoring the local shear stress toward the optimal set point. Consistent with our findings, Clark *et al.* demonstrated in a frog model that reductions in flow lead to regression of small vessels, whereas vessels exposed to high shear stress are stabilized [151]. Hence, our observations align closely with previous reports highlighting the role of wall shear stress in vascular remodeling. We further hypothesize that increasing shear stress magnitude may drive additional vessel enlargement and remodeling, thereby optimizing the vascular network to accommodate elevated hemodynamic demands.

Analysis of immunostained devices under the three experimental conditions quantitatively highlighted clear variations in vessel architecture that arose from differences in the applied shear stress. Higher shear stress enhanced the co-localization of smooth muscle cells (SMCs) with HUAECs and was associated with the formation of thicker, more efficiently perfused vessels. Notably, the high-shear (HS) condition exhibited the greatest SMC proliferation and extensive circumferential wrapping of SMCs around the endothelium. In contrast, the control condition showed minimal SMC–vessel association, while the low-shear condition displayed an intermediate level of SMC co-localization. Studies have shown that both interstitial and intraluminal flow influence SMC recruitment by distinct mechanisms. Previous research have shown that interstitial flow upregulates MMP-1 production which promotes migration and recruitment of SMCs to the ECs via chemokine gradient formation [152]. While this gradient-mediated recruitment guides SMCs toward ECs, it is less spatially organized. However, intraluminal flow generates shear stress on ECs, that enhances SMC recruiting factors such as PDGF-BB and TGF-β [153], [154], [155]. In this case, the SMCs are directed

doi:10.6342/NTU202600103

towards the ECs and facilitate the formation of tightly wrapped multilayered vascular structures. Our findings are consistent with previous studies, which show that higher intraluminal flow induces high shear stress and modulates the formation of better arteriole-like architecture. These observations highlight the crucial role of shear stress and arteriogenesis in achieving physiologically relevant arteriole architecture within self-assembling microfluidic devices. In fact, without flow, our control devices resembled capillaries. Hence, developing disease models on platforms that generate MVNs only using vasculogenesis and angiogenesis cannot fully recapitulate the cell-cell cross talk in disease progression.

Empty basement membranes indicates regressed blood vessels. Animal studies have shown that these structures represent remnants of a pre-existing vascular network that persist following vessel regression [156], [157]. These findings suggest that the basement membrane preserves a structural imprint of the vasculature established during vasculogenesis and angiogenesis, which is later reshaped in response to both external and intrinsic cues. Our results further demonstrate that the extent to which this initial vascular architecture is maintained depends on the magnitude of the applied shear stress. No flow and low shear stress conditions showed over 30% reduction in vessel diameters compared to only 15% in the HS condition. Final vessel area coverage comapared to the BM area coverage was also greatly reduced in static (74.24%) and LS (64.19%) conditions, while HS showed only a 30.37% reduction. Hence, better retention of initial vessel network in HS condition underscores the importance of high oscillatory shear stress in maintaining arteriolar structure and stability.

To investigate the influence of local hydrodynamic environment on endothelial and basement membrane behavior in determining vessel hierarchy, we performed finite element analysis. As shown in Figure 5-17 A, two vessel segments originated from a

doi:10.6342/NTU202600103

common source, with shear stress guiding the development of one into a primary vessel and the other into a secondary vessel. Shear stress mapping revealed that secondary vessels exhibited higher wall shear stress compared to primary vessels (Figure 5-18 A). Since remodeling originated from the basement membrane (BM), analysis of the BM also revealed elevated shear stress in regions corresponding to secondary vessel structures (Figure 5-18 C). This suggests that regions of the basement membrane with lower shear stress preferentially guided fluid flow and developed into primary vessels, while areas exposed to higher shear stress formed secondary vessels. The level of wall shear stress for vessels was between 1.42 Pa to 8.13Pa. As the mean WSS is arterioles ranges between 2.0 Pa – 10 Pa [158], our method can simulate in vivo arteriolar physiology. Interestingly, the wall shear stress at the basement membrane was roughly fivefold lower than at the endothelial surface. This reduction is due to the interposed smooth muscle cell layer, which increases the effective diameter of the basement membrane. Nevertheless, the shear stress profile continues to mirror the hydrodynamic conditions of the original vessel architecture.

We hypothesised that vessel remodeling and functional performance represent distinct aspects of vascular behavior. While remodeling reflects the developmental changes of the vessel, functional performance is determined by the types and interactions of vascular cells. Once the hydrodynamic and metabolic conditions stabilized, the arteriolar structure reached equilibrium, and remodeling activity largely subsided. The functional properties of these arterioles arise from the coordinated signaling between the endothelium and the surrounding smooth muscle layer. To confirm this, we assessed arteriole functionality through smooth muscle cell–mediated vasomotion.

Vasomotion is a critical physiological characteristic of arteries. Active regulation of vessel diameters is dependent on SMCs [159], [160]. Vasodilators are used to lower

doi:10.6342/NTU202600103

blood pressure and manage conditions like acute heart failure, myocardial infarction, and chronic congestive heart failure, while vasoconstrictors are applied in treating hypothermia, shock, asthma, and COPD. Dopamine can act as either a vasodilator or a vasoconstrictor, depending on the administered dose. In this study, we used different dosages of dopamine to test the functionality of our developed vessels. We found that low doses of dopamine induced vasodilation, while higher doses led to vessel constriction and loss of perfusion. Notably, dopamine's vasomotor effects depend on the presence of SMCs, as they express the relevant receptors [138], [161]. Our findings confirm that the SMCs wrapped around the endothelium in our model respond to dopamine dosage, mediating vessel tone accordingly. However, we also observed that in HUAEC+NHLF co-culture, although vessel diameters did not change due to absence of SMCs, total loss of perfusion was still observed at higher dosage of dopamine. This could be due to multiple factors such as endothelial dysfunction, local collapse, or microvascular blockages. Hence, we can clearly observe the distinct impact of dopamine on endothelial and smooth muscle cells. This highlights the importance of a human-like multicellular arterial structure; drug response on individual cell type can be elucidated, facilitating the development of precision medicine. We studied another aspect of vessel functionality, examining the production of endothelial nitric oxide in response to high shear stress. Our experiment confirmed that high shear stress enhances NO production, whereas in the absence of flow, NO levels remained minimal and undetectable. (Figure 5-22). Together, these results demonstrate that our model can generate *in vitro* arteriolar MVNs that replicate key *in vivo* arteriolar functions, providing a robust platform for drug testing and analysis.

Next we assessed the feasibility of our device for vascular disease modeling. We aimed to develop thrombosis and atherosclerosis. Thrombosis is the abnormal formation

doi:10.6342/NTU202600103

of a blood clot within a vessel, which can obstruct circulation and lead to life-threatening complications. However, the mechanisms of arterial thrombosis, venous thrombosis, and microvascular thrombosis are different. Reference [162] explains their differences clearly. Most existing vessel-on-a-chip systems predominantly employ HUVECs or HMVECs, which are either cultured along artificial microchannels [163], [164] or on porous membranes with smooth muscle cells positioned on the opposite side [165]. Yet, arterial endothelial cells can exhibit responses distinct from those of endothelial cells in microvascular or venous networks. Importantly, arterial thrombosis frequently develops from atherosclerosis, an inflammatory disorder characterized by impaired vasoconstriction–vasodilation balance and enhanced vascular permeability to lipoproteins. In this context, smooth muscle cells migrate into the intimal layer, undergo proliferation, resist apoptosis, and drive the accumulation of extracellular matrix and lipids, ultimately resulting in thickened arterial walls and lumen narrowing. [166]. Similar to thrombosis, atherosclerosis also has been studied on engineered artificial vessel-like structures that do not fully recapitulate the in vitro dimension or anatomy of blood vessels [167], [168]. Therefore, accurately modeling atherosclerosis and arterial thrombosis requires faithful reconstruction of arterial anatomy. In this study, we successfully induced arterial thrombosis within a self-assembled arteriole-on-a-chip model. We could damage the EC lining of the vessel and trigger the release of vWF (Figure 5-24). Upon flowing blood, platelets adhered to the released vWFs and formed platelet-induced thrombosis. We also developed the primary stage of atherosclerosis marked by leukocyte adhesion to the endothelial walls. Gut microbiota-derived metabolite TMAO has been increasingly recognized as an atherogenic agent. To verify this, we flowed 200 μM TMAO for 2 hrs in a matured aarteriolar network to upregulate inflammatory pathways in ECs. We perfused blood through stimulated ECs for 1 hr and

doi:10.6342/NTU202600103

observed adherence of leukocytes to the arterial walls after immunostaining Figure 5-26). Our results show that self-assembled arterioles can model both atherosclerosis and thrombosis, providing a platform for studying the underlying cell–cell interactions in these diseases.

While this study provides a novel platform to study the pathobiology of arterial diseases, a few limitations should be acknowledged. First, the low shear condition relies on pipette tips that equilibrate within a few hours, causing the applied pressure to decrease and become inconsistent over time. Developing new methods for continuous perfusion to maintain stable low shear stress could enable more accurate long-term studies. Second, modeling the chronic effects of TMAO on atherosclerosis remains challenging, as vessel structures have not yet been maintained beyond 13 days. Ultimately, exploring different matrix stiffnesses may help extend the lifespan of the developed microvascular networks and enhance the robustness of long-term disease modeling.

doi:10.6342/NTU202600103

7. Conclusion

In this study, we present a physiologically inspired methodology to develop the first self-assembled human arteriole network within a microfluidic platform using human umbilical artery endothelial cells (HUAECs), human umbilical smooth muscle cells (HUSMCs), and normal human lung fibroblasts (NHLFs). We precisely controlled the physiological microenvironment within the three-dimensional culture chamber of the arteriole-on-a-chip (AoC) device to induce vasculogenesis, angiogenesis and aretriogenesis. Initially, a hypoxic condition was applied to promote vasculogenesis and angiogenesis, resulting in the formation of a primitive vascular network. Subsequently, either a relatively high or low flow was introduced within the arterioles at 1 Hz oscillatory pressure to stimulate arteriogenesis. Our findings demonstrate that oscillating fluid shear stress serves as a critical physiological regulator of arterial development, influencing vessel perfusability, arterial remodeling, and the spatial co-localization of endothelial and smooth muscle cells. Furthermore, we show that magnitude of wall shear stress plays a key role in arterial maturation and maintaining physiologically relevant shear stress levels is essential for accurately recapitulating the *in vivo* arterial environment. Importantly, this arteriole-on-a-chip model supports functional vasodilation and vasoconstriction and allows direct perfusion of whole human blood through the arteriole network. These capabilities enable *in vitro* studies of arterial pathologies, including thrombosis and atherosclerosis.

In summary, this work introduces a novel arteriole-on-a-chip platform that provides a robust and physiologically relevant alternative to animal models for investigating artery-related cardiovascular diseases, aligning with the 3Rs principles (replacement, reduction, and refinement) in drug discovery and development.

doi:10.6342/NTU202600103

8. Future Work

Current dissertation focused on understanding vascular remodeling and developing disease models. In the future, we aim to use our engineered MVN system as a preclinical platform to screen and evaluate potential drugs for preventing or mitigating thrombosis and atherosclerosis, providing an initial assessment of drug efficacy before progressing to animal or human studies.

Our device also can help to study vasomotion—the rhythmic contraction and relaxation of blood vessels—by testing agents similar to dopamine. Intriguingly, our preliminary data suggest that dopamine exerts differential effects on endothelial cells (ECs) and smooth muscle cells (SMCs), a finding that underscores the importance of examining cell-specific responses to vascular stimuli. Given our ability to model arterioles both with and without SMC layers, we can dissect the individual contributions of ECs and SMCs in drug response and disease dynamics. This modularity allows for targeted testing of therapeutic candidates, and facilitates a deeper understanding of how specific vascular cell types respond to physiological or pathological stimuli.

Overall, our arteriole-on-a-chip platform provides a powerful, scalable alternative to traditional animal models for arterial disease research. It offers a more precise, rapid, and human-relevant system for studying disease mechanisms and screening potential therapeutics, thereby accelerating the discovery and development of vascular-targeted interventions.

doi:10.6342/NTU202600103

9. References

[1] "The top 10 causes of death." Accessed: Feb. 21, 2025. [Online]. Available: https://www.who.int/news-room/fact-sheets/detail/the-top-10-causes-of-death

[2] I. V. Hinkson, B. Madej, and E. A. Stahlberg, "Accelerating Therapeutics for Opportunities in Medicine: A Paradigm Shift in Drug Discovery," *Front Pharmacol*, vol. 11, p. 770, June 2020, doi: 10.3389/fphar.2020.00770.

[3] "Poor Translatability of Biomedical Research Using Animals — A Narrative Review - Lindsay J. Marshall, Jarrod Bailey, Manuela Cassotta, Kathrin Herrmann," https://journals.sagepub.com/doi/10.1177/02611929231157756

[4] "Pre-clinical animal models are poor predictors of human toxicities in phase 1 oncology clinical trials | British Journal of Cancer." https://www.nature.com/articles/s41416-020-01033-x

[5] G. A. Van Norman, "Limitations of Animal Studies for Predicting Toxicity in Clinical Trials: Is it Time to Rethink Our Current Approach?," *JACC: Basic to Translational Science*, vol. 4, no. 7, pp. 845–854, Nov. 2019, doi: 10.1016/j.jacbts.2019.10.008.

[6] "Classification & Structure of Blood Vessels | SEER Training." Available:https://training.seer.cancer.gov/anatomy/cardiovascular/blood/classification.html

[7] M. Kapałczyńska *et al.*, "2D and 3D cell cultures – a comparison of different types of cancer cell cultures," *Arch Med Sci*, vol. 14, no. 4, pp. 910–919, June 2018, doi: 10.5114/aoms.2016.63743.

[8] M. C. Koyilot *et al.*, "Breakthroughs and Applications of Organ-on-a-Chip Technology," *Cells*, vol. 11, no. 11, p. 1828, June 2022, doi: 10.3390/cells11111828.

doi:10.6342/NTU202600103

[9] P. Zamprogno *et al.*, "Second-generation lung-on-a-chip with an array of stretchable alveoli made with a biological membrane," *Commun Biol*, vol. 4, no. 1, p. 168, Feb. 2021, doi: 10.1038/s42003-021-01695-0.

[10] A. Valiei, J. Aminian-Dehkordi, and M. R. K. Mofrad, "Gut-on-a-chip models for dissecting the gut microbiology and physiology," *APL Bioeng*, vol. 7, no. 1, p. 011502, Feb. 2023, doi: 10.1063/5.0126541.

[11] J. Lee and S. Kim, "Kidney-on-a-Chip: A New Technology for Predicting Drug Efficacy, Interactions, and Drug-induced Nephrotoxicity," *Curr Drug Metab*, vol. 19, no. 7, pp. 577–583, 2018, doi: 10.2174/1389200219666180309101844.

[12] B. Liu *et al.*, "Heart-on-a-chip: a revolutionary organ-on-chip platform for cardiovascular disease modeling," *Journal of Translational Medicine*, vol. 23, no. 1, p. 132, Jan. 2025, doi: 10.1186/s12967-024-05986-y.

[13] L. Qiu, B. Kong, T. Kong, and H. Wang, "Recent advances in liver-on-chips: Design, fabrication, and applications," *Smart Medicine*, vol. 2, no. 1, p. e20220010, 2023, doi: 10.1002/SMMD.20220010.

[14] L. Amirifar *et al.*, "Brain-on-a-chip: Recent advances in design and techniques for microfluidic models of the brain in health and disease," *Biomaterials*, vol. 285, p. 121531, June 2022, doi: 10.1016/j.biomaterials.2022.121531.

[15] S. R. Moses, J. J. Adorno, A. F. Palmer, and J. W. Song, "Vessel-on-a-chip models for studying microvascular physiology, transport, and function in vitro," *Am J Physiol Cell Physiol*, vol. 320, no. 1, pp. C92–C105, Jan. 2021, doi: 10.1152/ajpcell.00355.2020.

[16] H. Deng, A. Eichmann, and M. A. Schwartz, "Fluid Shear Stress–Regulated Vascular Remodeling: Past, Present, and Future," *Arteriosclerosis, Thrombosis, and*

doi:10.6342/NTU202600103

Vascular Biology, vol. 45, no. 6, pp. 882–900, June 2025, doi: 10.1161/ATVBAHA.125.322557.

[17] "Frequency of a Beating Heart - The Physics Factbook." Accessed: Nov. 14, 2025. [Online]. Available: https://hypertextbook.com/facts/1998/ArsheAhmed.shtml

[18] S. Dimmeler, I. Fleming, B. Fisslthaler, C. Hermann, R. Busse, and A. M. Zeiher, "Activation of nitric oxide synthase in endothelial cells by Akt-dependent phosphorylation," *Nature*, vol. 399, no. 6736, pp. 601–605, June 1999, doi: 10.1038/21224.

[19] I. Fleming, B. Fisslthaler, M. Dixit, and R. Busse, "Role of PECAM-1 in the shear-stress-induced activation of Akt and the endothelial nitric oxide synthase (eNOS) in endothelial cells," *J Cell Sci*, vol. 118, no. Pt 18, pp. 4103–4111, Sept. 2005, doi: 10.1242/jcs.02541.

[20] A. Yamashita and Y. Asada, "Underlying mechanisms of thrombus formation/growth in atherothrombosis and deep vein thrombosis," *Pathol Int*, vol. 73, no. 2, pp. 65–80, Feb. 2023, doi: 10.1111/pin.13305.

[21] A. Michels, D. Lillicrap, and M. Yacob, "Role of von Willebrand factor in venous thromboembolic disease," *JVS Vasc Sci*, vol. 3, pp. 17–29, Oct. 2021, doi: 10.1016/j.jvssci.2021.08.002.

[22] Z. M. Ruggeri, "The role of von Willebrand factor in thrombus formation," *Thromb Res*, vol. 120 Suppl 1, no. Suppl 1, pp. S5-9, 2007, doi: 10.1016/j.thromres.2007.03.011.

[23] M. Franchini and G. Lippi, "Von Willebrand factor and thrombosis," *Ann Hematol*, vol. 85, no. 7, pp. 415–423, July 2006, doi: 10.1007/s00277-006-0085-5.

doi:10.6342/NTU202600103

[24] G. Y. H. Lip and A. Blann, “von Willebrand factor: a marker of endothelial dysfunction in vascular disorders?,” *Cardiovasc Res*, vol. 34, no. 2, pp. 255–265, May 1997, doi: 10.1016/S0008-6363(97)00039-4.

[25] S. Jebari-Benslaiman *et al.*, “Pathophysiology of Atherosclerosis,” *Int J Mol Sci*, vol. 23, no. 6, p. 3346, Mar. 2022, doi: 10.3390/ijms23063346.

[26] H. Pan *et al.*, “Atherosclerosis Is a Smooth Muscle Cell–Driven Tumor-Like Disease,” *Circulation*, vol. 149, no. 24, pp. 1885–1898, June 2024, doi: 10.1161/CIRCULATIONAHA.123.067587.

[27] Y. H. Oktaviono *et al.*, “The roles of trimethylamine-N-oxide in atherosclerosis and its potential therapeutic aspect: A literature review,” *Biomol Biomed*, vol. 23, no. 6, pp. 936–948, Nov. 2023, doi: 10.17305/bb.2023.8893.

[28] M. M. Seldin *et al.*, “Trimethylamine N-Oxide Promotes Vascular Inflammation Through Signaling of Mitogen-Activated Protein Kinase and Nuclear Factor-κB,” *J Am Heart Assoc*, vol. 5, no. 2, p. e002767, Feb. 2016, doi: 10.1161/JAHA.115.002767.

[29] Y. Zhu, Q. Li, and H. Jiang, “Gut microbiota in atherosclerosis: focus on trimethylamine N-oxide,” *APMIS*, vol. 128, no. 5, pp. 353–366, May 2020, doi: 10.1111/apm.13038.

[30] W. Risau and I. Flamme, “Vasculogenesis,” *Annual Review of Cell and Developmental Biology*, vol. 11, no. Volume 11, 1995, pp. 73–91, Nov. 1995, doi: 10.1146/annurev.cb.11.110195.000445.

[31] “Angiogenesis, Vasculogenesis, and Induction of Healing in Chronic Wounds.” Accessed: July 30, 2025. [Online]. Available: https://journals.sagepub.com/doi/epdf/10.1177/153857440503900401

doi:10.6342/NTU202600103

[32] S. Balaji, A. King, T. M. Crombleholme, and S. G. Keswani, "The Role of Endothelial Progenitor Cells in Postnatal Vasculogenesis: Implications for Therapeutic Neovascularization and Wound Healing," *Adv Wound Care (New Rochelle)*, vol. 2, no. 6, pp. 283–295, July 2013, doi: 10.1089/wound.2012.0398.

[33] S. Patel-Hett and P. A. DAmore, "Signal transduction in vasculogenesis and developmental angiogenesis," *Int. J. Dev. Biol.*, vol. 55, no. 4–5, pp. 353–363, 2011, doi: 10.1387/ijdb.103213sp.

[34] R. K. Jain, "Molecular regulation of vessel maturation," *Nat Med*, vol. 9, no. 6, pp. 685–693, June 2003, doi: 10.1038/nm0603-685.

[35] A. M. Goodwin and PatriciaA. D'Amore, "Vessel Maturation and Perivascular Cells," in *Tumor Angiogenesis: Basic Mechanisms and Cancer Therapy*, D. Marmé and N. Fusenig, Eds., Berlin, Heidelberg: Springer, 2008, pp. 273–288. doi: 10.1007/978-3-540-33177-3_15.

[36] D. Stenzel, E. Nye, M. Nisancioglu, R. H. Adams, Y. Yamaguchi, and H. Gerhardt, "Peripheral mural cell recruitment requires cell-autonomous heparan sulfate," *Blood*, vol. 114, no. 4, pp. 915–924, July 2009, doi: 10.1182/blood-2008-10-186239.

[37] K. Yrigoin and G. E. Davis, "Selective mural cell recruitment of pericytes to networks of assembling endothelial cell-lined tubes," *Front. Cell Dev. Biol.*, vol. 12, June 2024, doi: 10.3389/fcell.2024.1389607.

[38] D. S. Grant, H. K. Kleinman, and G. R. Martin, "The Role of Basement Membranes in Vascular Development," *Annals of the New York Academy of Sciences*, vol. 588, no. 1, pp. 61–72, 1990, doi: 10.1111/j.1749-6632.1990.tb13197.x.

[39] A. S. Harris, R. Lennon, and J.-M. Schwartz, "Building basement membranes with computational approaches," *Matrix Biology*, vol. 140, pp. 88–99, Sept. 2025, doi: 10.1016/j.matbio.2025.07.001.

doi:10.6342/NTU202600103

[40] J. H. Miner, “Renal basement membrane components,” *Kidney International*, vol. 56, no. 6, pp. 2016–2024, Dec. 1999, doi: 10.1046/j.1523-1755.1999.00785.x.

[41] M. S. Thomsen, L. J. Routhe, and T. Moos, “The vascular basement membrane in the healthy and pathological brain,” *J Cereb Blood Flow Metab*, vol. 37, no. 10, pp. 3300–3317, Oct. 2017, doi: 10.1177/0271678X17722436.

[42] S. Patan, “Vasculogenesis and Angiogenesis,” in *Angiogenesis in Brain Tumors*, M. Kirsch and P. McL. Black, Eds., Boston, MA: Springer US, 2004, pp. 3–32. doi: 10.1007/978-1-4419-8871-3_1.

[43] P. Carmeliet, “Angiogenesis in life, disease and medicine,” *Nature*, vol. 438, no. 7070, pp. 932–936, Dec. 2005, doi: 10.1038/nature04478.

[44] M. G. Tonnesen, X. Feng, and R. A. F. Clark, “Angiogenesis in Wound Healing,” *Journal of Investigative Dermatology Symposium Proceedings*, vol. 5, no. 1, pp. 40–46, Dec. 2000, doi: 10.1046/j.1087-0024.2000.00014.x.

[45] T. H. Adair and J.-P. Montani, “Overview of Angiogenesis,” in *Angiogenesis*, Morgan & Claypool Life Sciences, 2010. Accessed: Aug. 05, 2025. [Online]. Available: https://www.ncbi.nlm.nih.gov/books/NBK53238/

[46] “Tumour Angiogenesis | Radiology Key.” Accessed: Aug. 05, 2025. [Online]. Available: https://radiologykey.com/tumour-angiogenesis/

[47] T. H. Adair and J.-P. Montani, “Overview of Angiogenesis,” in *Angiogenesis*, Morgan & Claypool Life Sciences, 2010. Accessed: Dec. 05, 2025. [Online]. Available: https://www.ncbi.nlm.nih.gov/books/NBK53238/

[48] R. S. Alameddine, L. Hamieh, and A. Shamseddine, “From Sprouting Angiogenesis to Erythrocytes Generation by Cancer Stem Cells: Evolving Concepts in Tumor Microcirculation,” *Biomed Res Int*, vol. 2014, p. 986768, 2014, doi: 10.1155/2014/986768.

doi:10.6342/NTU202600103

[49] "Angiopoietin-2, a Natural Antagonist for Tie2 That Disrupts in vivo Angiogenesis | Science." Accessed: Aug. 05, 2025. [Online]. Available: https://www.science.org/doi/10.1126/science.277.5322.55?url_ver=Z39.88-2003&rfr_id=ori:rid:crossref.org&rfr_dat=cr_pub%20%200pubmed

[50] N. W. Gale and G. D. Yancopoulos, "Growth factors acting via endothelial cell-specific receptor tyrosine kinases: VEGFs, angiopoietins, and ephrins in vascular development," *Genes Dev*, vol. 13, no. 9, pp. 1055–1066, May 1999, doi: 10.1101/gad.13.9.1055.

[51] L. M. Coussens *et al.*, "Inflammatory mast cells up-regulate angiogenesis during squamous epithelial carcinogenesis," *Genes Dev.*, vol. 13, no. 11, pp. 1382–1397, June 1999.

[52] D. Kolte, J. A. McClung, and W. S. Aronow, "Chapter 6 - Vasculogenesis and Angiogenesis," in *Translational Research in Coronary Artery Disease*, W. S. Aronow and J. A. McClung, Eds., Boston: Academic Press, 2016, pp. 49–65. doi: 10.1016/B978-0-12-802385-3.00006-1.

[53] I. Cebola, G. M. Birdsey, and A. M. Randi, "Transcriptional pausing as a molecular mechanism of sprouting angiogenesis," *Nat Cardiovasc Res*, vol. 3, no. 10, pp. 1184–1186, Oct. 2024, doi: 10.1038/s44161-024-00547-4.

[54] A. A. Ucuzian, A. A. Gassman, A. T. East, and H. P. Greisler, "Molecular Mediators of Angiogenesis," *J Burn Care Res*, vol. 31, no. 1, p. 158, 2010, doi: 10.1097/BCR.0b013e3181c7ed82.

[55] S. J. Mentzer and M. A. Konerding, "Intussusceptive Angiogenesis: Expansion and Remodeling of Microvascular Networks," *Angiogenesis*, vol. 17, no. 3, pp. 499–509, July 2014, doi: 10.1007/s10456-014-9428-3.

doi:10.6342/NTU202600103

[56] R. Gianni-Barrera *et al.*, "VEGF over-expression in skeletal muscle induces angiogenesis by intussusception rather than sprouting," *Angiogenesis*, vol. 16, no. 1, pp. 123–136, Jan. 2013, doi: 10.1007/s10456-012-9304-y.

[57] A. Pandita *et al.*, "Intussusceptive Angiogenesis in Human Metastatic Malignant Melanoma," *Am J Pathol*, vol. 191, no. 11, pp. 2023–2038, Nov. 2021, doi: 10.1016/j.ajpath.2021.07.009.

[58] P. Schlatter, M. F. König, L. M. Karlsson, and P. H. Burri, "Quantitative Study of Intussusceptive Capillary Growth in the Chorioallantoic Membrane (CAM) of the Chicken Embryo," *Microvascular Research*, vol. 54, no. 1, pp. 65–73, July 1997, doi: 10.1006/mvre.1997.2022.

[59] A. N. Makanya, D. Stauffer, D. Ribatti, P. H. Burri, and V. Djonov, "Microvascular growth, development, and remodeling in the embryonic avian kidney: The interplay between sprouting and intussusceptive angiogenic mechanisms," *Microscopy Research and Technique*, vol. 66, no. 6, pp. 275–288, 2005, doi: 10.1002/jemt.20169.

[60] M. D. Brown and O. Hudlicka, "Modulation of physiological angiogenesis in skeletal muscle by mechanical forces: Involvement of VEGF and metalloproteinases," *Angiogenesis*, vol. 6, no. 1, pp. 1–14, Oct. 2003, doi: 10.1023/A:1025809808697.

[61] W. De Spiegelaere *et al.*, "Intussusceptive Angiogenesis: A Biologically Relevant Form of Angiogenesis," *J Vasc Res*, vol. 49, no. 5, pp. 390–404, June 2012, doi: 10.1159/000338278.

[62] V. Djonov, M. Schmid, S. A. Tschanz, and P. H. Burri, "Intussusceptive Angiogenesis," *Circulation Research*, vol. 86, no. 3, pp. 286–292, Feb. 2000, doi: 10.1161/01.RES.86.3.286.

doi:10.6342/NTU202600103

[63] S. Paku *et al.*, “A New Mechanism for Pillar Formation during Tumor-Induced Intussusceptive Angiogenesis: Inverse Sprouting,” *The American Journal of Pathology*, vol. 179, no. 3, pp. 1573–1585, Sept. 2011, doi: 10.1016/j.ajpath.2011.05.033.

[64] R. Hlushchuk *et al.*, “Tumor Recovery by Angiogenic Switch from Sprouting to Intussusceptive Angiogenesis after Treatment with PTK787/ZK222584 or Ionizing Radiation,” *The American Journal of Pathology*, vol. 173, no. 4, pp. 1173–1185, Oct. 2008, doi: 10.2353/ajpath.2008.071131.

[65] M. A. Konerding *et al.*, “Inflammation-Induced Intussusceptive Angiogenesis in Murine Colitis,” *Anat Rec (Hoboken)*, vol. 293, no. 5, pp. 849–857, May 2010, doi: 10.1002/ar.21110.

[66] M. Ackermann *et al.*, “Pulmonary Vascular Endothelialitis, Thrombosis, and Angiogenesis in Covid-19,” *New England Journal of Medicine*, vol. 383, no. 2, pp. 120–128, July 2020, doi: 10.1056/NEJMoa2015432.

[67] E. Deindl and W. Schaper, “The art of arteriogenesis,” *Cell Biochem Biophys*, vol. 43, no. 1, pp. 1–15, Aug. 2005, doi: 10.1385/CBB:43:1:001.

[68] W. Cai and W. Schaper, “Mechanisms of arteriogenesis,” *ABBS*, vol. 40, no. 8, pp. 681–692, Aug. 2008, doi: 10.1093/abbs/40.8.681.

[69] “Influence of Mechanical, Cellular, and Molecular Factors on Collateral Artery Growth (Arteriogenesis) | Circulation Research.” Accessed: Sept. 12, 2025. [Online]. Available: https://www.ahajournals.org/doi/10.1161/01.RES.0000141145.78900.44?url_ver=Z39.88-2003&rfr_id=ori:rid:crossref.org&rfr_dat=cr_pub%20%200pubmed

doi:10.6342/NTU202600103

[70] B. J. Ballermann, A. Dardik, E. Eng, and A. Liu, “Shear stress and the endothelium,” *Kidney International*, vol. 54, pp. S100–S108, Sept. 1998, doi: 10.1046/j.1523-1755.1998.06720.x.

[71] “The distribution of blood rheological parameters in the microvasculature of cat mesentery.” Accessed: Sept. 15, 2025. [Online]. Available: https://www.ahajournals.org/doi/epdf/10.1161/01.RES.43.5.738

[72] N. Raj, C. Pan, A. M. Starke, A. L. L. Matos, O. Soehnlein, and V. Gerke, “Altered shear stress of blood flow causes plasma membrane damage in endothelial cells,” *Blood Vessels, Thrombosis & Hemostasis*, vol. 2, no. 1, p. 100040, Jan. 2025, doi: 10.1016/j.bvth.2024.100040.

[73] “Role of Shear Stress in Atherosclerosis and Restenosis After Coronary Stent Implantation,” *Revista Española de Cardiología (English Edition)*, vol. 59, no. 1, pp. 1–4, Jan. 2006, doi: 10.1016/S1885-5857(06)60040-6.

[74] K. S. Cunningham and A. I. Gotlieb, “The role of shear stress in the pathogenesis of atherosclerosis,” *Laboratory Investigation*, vol. 85, no. 1, pp. 9–23, Jan. 2005, doi: 10.1038/labinvest.3700215.

[75] M. Zhou *et al.*, “Wall shear stress and its role in atherosclerosis,” *Front. Cardiovasc. Med.*, vol. 10, Apr. 2023, doi: 10.3389/fcvm.2023.1083547.

[76] C. M. Warboys, N. Amini, A. de Luca, and P. C. Evans, “The role of blood flow in determining the sites of atherosclerotic plaques,” *F1000 Med Rep*, vol. 3, p. 5, Mar. 2011, doi: 10.3410/M3-5.

[77] L. D. C. Casa, D. H. Deaton, and D. N. Ku, “Role of high shear rate in thrombosis,” *Journal of Vascular Surgery*, vol. 61, no. 4, pp. 1068–1080, Apr. 2015, doi: 10.1016/j.jvs.2014.12.050.

doi:10.6342/NTU202600103

[78] “Flow-Dependent Remodeling of Small Arteries.” Accessed: Sept. 16, 2025. [Online]. Available: https://www.ahajournals.org/doi/epub/10.1161/01.RES.0000233144.65663.23

[79] M. J. Mulvany, “Vascular remodelling of resistance vessels: can we define this?,” *Cardiovasc Res*, vol. 41, no. 1, pp. 9–13, Jan. 1999, doi: 10.1016/S0008-6363(98)00289-2.

[80] C. A. Franco *et al.*, “Dynamic Endothelial Cell Rearrangements Drive Developmental Vessel Regression,” *PLOS Biology*, vol. 13, no. 4, p. e1002125, Apr. 2015, doi: 10.1371/journal.pbio.1002125.

[81] J. R. Crawshaw, J. A. Flegg, M. O. Bernabeu, and J. M. Osborne, “Mathematical models of developmental vascular remodelling: A review,” *PLoS Comput Biol*, vol. 19, no. 8, p. e1011130, Aug. 2023, doi: 10.1371/journal.pcbi.1011130.

[82] W. Yao, Y. Li, and G. Ding, “Interstitial Fluid Flow: The Mechanical Environment of Cells and Foundation of Meridians,” *Evid Based Complement Alternat Med*, vol. 2012, p. 853516, 2012, doi: 10.1155/2012/853516.

[83] J. Scallan, V. H. Huxley, and R. J. Korthuis, “The Interstitium,” in *Capillary Fluid Exchange: Regulation, Functions, and Pathology*, Morgan & Claypool Life Sciences, 2010. Accessed: Sept. 17, 2025. [Online]. Available: https://www.ncbi.nlm.nih.gov/books/NBK53446/

[84] W. Liu, Y. Cao, X. Zhou, and D. Han, “Interstitial Fluid Behavior and Diseases,” *Adv Sci (Weinh)*, vol. 9, no. 6, p. 2100617, Jan. 2022, doi: 10.1002/advs.202100617.

[85] J. M. Munson and A. C. Shieh, “Interstitial fluid flow in cancer: implications for disease progression and treatment,” *Cancer Management and Research*, vol. 6, pp. 317–328, Aug. 2014, doi: 10.2147/CMAR.S65444.

doi:10.6342/NTU202600103

[86] G. Follain *et al.*, "Fluids and their mechanics in tumour transit: shaping metastasis," *Nat Rev Cancer*, vol. 20, no. 2, pp. 107–124, Feb. 2020, doi: 10.1038/s41568-019-0221-x.

[87] J. Choi, E. Choi, and D. Choi, "The ambivalent nature of the relationship between lymphatics and cancer," *Front. Cell Dev. Biol.*, vol. 10, Sept. 2022, doi: 10.3389/fcell.2022.931335.

[88] J. M. Munson, "Interstitial fluid flow under the microscope: is it a future drug target for high-grade brain tumours such as glioblastoma?," *Expert Opin Ther Targets*, p. 10.1080/14728222.2019.1647167, July 2019, doi: 10.1080/14728222.2019.1647167.

[89] G. Sriram and H. Makkar, "Microfluidic organ-on-chip systems for periodontal research: advances and future directions," *Front. Bioeng. Biotechnol.*, vol. 12, Jan. 2025, doi: 10.3389/fbioe.2024.1490453.

[90] S. Shuchat, G. Yossifon, and M. Huleihel, "Perfusion in Organ-on-Chip Models and Its Applicability to the Replication of Spermatogenesis In Vitro," *Int J Mol Sci*, vol. 23, no. 10, p. 5402, May 2022, doi: 10.3390/ijms23105402.

[91] B. Kramer *et al.*, "Interstitial Flow Recapitulates Gemcitabine Chemoresistance in A 3D Microfluidic Pancreatic Ductal Adenocarcinoma Model by Induction of Multidrug Resistance Proteins," *International Journal of Molecular Sciences*, vol. 20, no. 18, p. 4647, Jan. 2019, doi: 10.3390/ijms20184647.

[92] D. Bazou, M. R. Ng, J. W. Song, S. M. Chin, N. Maimon, and L. L. Munn, "Flow-induced HDAC1 phosphorylation and nuclear export in angiogenic sprouting," *Sci Rep*, vol. 6, no. 1, p. 34046, Sept. 2016, doi: 10.1038/srep34046.

[93] V. S. Shirure, A. Lezia, A. Tao, L. F. Alonzo, and S. C. George, "Low levels of physiological interstitial flow eliminate morphogen gradients and guide

doi:10.6342/NTU202600103

angiogenesis," *Angiogenesis*, vol. 20, no. 4, pp. 493–504, Nov. 2017, doi: 10.1007/s10456-017-9559-4.

[94] M. L. Moya, Y.-H. Hsu, A. P. Lee, C. C. W. Hughes, and S. C. George, "In Vitro Perfused Human Capillary Networks," *Tissue Eng Part C Methods*, vol. 19, no. 9, pp. 730–737, Sept. 2013, doi: 10.1089/ten.tec.2012.0430.

[95] Y.-H. Hsu, M. L. Moya, P. Abiri, C. C. W. Hughes, S. C. George, and A. P. Lee, "Full range physiological mass transport control in 3D tissue cultures," *Lab Chip*, vol. 13, no. 1, pp. 81–89, Jan. 2013, doi: 10.1039/c2lc40787f.

[96] Y.-H. Hsu, M. L. Moya, C. C. W. Hughes, S. C. Georgea, and A. P. Lee, "A microfluidic platform for generating large-scale nearly identical human microphysiological system arrays," *Lab Chip*, vol. 13, no. 15, pp. 2990–2998, Aug. 2013, doi: 10.1039/c3lc50424g.

[97] I. S. Ilan, A. R. Yslas, Y. Peng, R. Lu, and E. Lee, "A 3D Human Lymphatic Vessel-on-Chip Reveals the Roles of Interstitial Flow and VEGF-A/C for Lymphatic Sprouting and Discontinuous Junction Formation," *Cell Mol Bioeng*, vol. 16, no. 4, pp. 325–339, Aug. 2023, doi: 10.1007/s12195-023-00780-0.

[98] K. C. Boardman and M. A. Swartz, "Interstitial Flow as a Guide for Lymphangiogenesis," *Circulation Research*, vol. 92, no. 7, pp. 801–808, Apr. 2003, doi: 10.1161/01.RES.0000065621.69843.49.

[99] Y. L. Huang, Y. Ma, C. Wu, C. Shiau, J. E. Segall, and M. Wu, "Tumor spheroids under perfusion within a 3D microfluidic platform reveal critical roles of cell-cell adhesion in tumor invasion," *Sci Rep*, vol. 10, p. 9648, June 2020, doi: 10.1038/s41598-020-66528-2.

doi:10.6342/NTU202600103

[100] Q. D. Tran, Marcos, and D. Gonzalez-Rodriguez, “Permeability and viscoelastic fracture of a model tumor under interstitial flow,” *Soft Matter*, vol. 14, no. 30, pp. 6386–6392, Aug. 2018, doi: 10.1039/C8SM00844B.

[101] W. J. Polacheck, J. L. Charest, and R. D. Kamm, “Interstitial flow influences direction of tumor cell migration through competing mechanisms,” *Proceedings of the National Academy of Sciences*, vol. 108, no. 27, pp. 11115–11120, July 2011, doi: 10.1073/pnas.1103581108.

[102] C. P. Ng, B. Hinz, and M. A. Swartz, “Interstitial fluid flow induces myofibroblast differentiation and collagen alignment in vitro,” *J Cell Sci*, vol. 118, no. Pt 20, pp. 4731–4739, Oct. 2005, doi: 10.1242/jcs.02605.

[103] J. M. Rutkowski and M. A. Swartz, “A driving force for change: interstitial flow as a morphoregulator,” *Trends in Cell Biology*, vol. 17, no. 1, pp. 44–50, Jan. 2007, doi: 10.1016/j.tcb.2006.11.007.

[104] M. Daems, H. M. Peacock, and E. A. V. Jones, “Fluid flow as a driver of embryonic morphogenesis,” *Development*, vol. 147, no. 15, p. dev185579, Aug. 2020, doi: 10.1242/dev.185579.

[105] X.-Y. Wang *et al.*, “An artificial blood vessel implanted three-dimensional microsystem for modeling transvascular migration of tumor cells,” *Lab Chip*, vol. 15, no. 4, pp. 1178–1187, 2015, doi: 10.1039/C4LC00973H.

[106] G. Lamberti *et al.*, “Bioinspired Microfluidic Assay for In Vitro Modeling of Leukocyte–Endothelium Interactions,” *Anal. Chem.*, vol. 86, no. 16, pp. 8344–8351, Aug. 2014, doi: 10.1021/ac5018716.

[107] S. Zhang, Z. Wan, and R. D. Kamm, “Vascularized organoids on a chip: Strategies for engineering organoids with functional vasculature,” *Lab Chip*, vol. 21, no. 3, pp. 473–488, Feb. 2021, doi: 10.1039/d0lc01186j.

doi:10.6342/NTU202600103

[108] D.-H. T. Nguyen *et al.*, "Biomimetic model to reconstitute angiogenic sprouting morphogenesis in vitro," *Proceedings of the National Academy of Sciences*, vol. 110, no. 17, pp. 6712–6717, Apr. 2013, doi: 10.1073/pnas.1221526110.

[109] C. F. Buchanan, S. S. Verbridge, P. P. Vlachos, and M. N. Rylander, "Flow shear stress regulates endothelial barrier function and expression of angiogenic factors in a 3D microfluidic tumor vascular model," *Cell Adhesion & Migration*, vol. 8, no. 5, pp. 517–524, Sept. 2014, doi: 10.4161/19336918.2014.970001.

[110] J. Lim *et al.*, "The Edifice of Vasculature-On-Chips: A Focused Review on the Key Elements and Assembly of Angiogenesis Models," *ACS Biomater. Sci. Eng.*, vol. 10, no. 6, pp. 3548–3567, June 2024, doi: 10.1021/acsbiomaterials.3c01978.

[111] S. Kim, H. Lee, M. Chung, and N. L. Jeon, "Engineering of functional, perfusable 3D microvascular networks on a chip," *Lab Chip*, vol. 13, no. 8, pp. 1489–1500, Mar. 2013, doi: 10.1039/C3LC41320A.

[112] M. Campisi, Y. Shin, T. Osaki, C. Hajal, V. Chiono, and R. D. Kamm, "3D Self-Organized Microvascular Model of the Human Blood-Brain Barrier with Endothelial Cells, Pericytes and Astrocytes," *Biomaterials*, vol. 180, pp. 117–129, Oct. 2018, doi: 10.1016/j.biomaterials.2018.07.014.

[113] A. Günther *et al.*, "A microfluidic platform for probing small artery structure and function," *Lab Chip*, vol. 10, no. 18, pp. 2341–2349, Aug. 2010, doi: 10.1039/C004675B.

[114] N. C. A. van Engeland, A. M. A. O. Pollet, J. M. J. den Toonder, C. V. C. Bouten, O. M. J. A. Stassen, and C. M. Sahlgren, "A biomimetic microfluidic model to study signalling between endothelial and vascular smooth muscle cells under hemodynamic conditions," *Lab Chip*, vol. 18, no. 11, pp. 1607–1620, May 2018, doi: 10.1039/C8LC00286J.

doi:10.6342/NTU202600103

[115] M. Vila Cuenca *et al.*, "Engineered 3D vessel-on-chip using hiPSC-derived endothelial- and vascular smooth muscle cells," *Stem Cell Reports*, vol. 16, no. 9, pp. 2159–2168, Sept. 2021, doi: 10.1016/j.stemcr.2021.08.003.

[116] C. Su *et al.*, "A novel human arterial wall-on-a-chip to study endothelial inflammation and vascular smooth muscle cell migration in early atherosclerosis," *Lab Chip*, vol. 21, no. 12, pp. 2359–2371, June 2021, doi: 10.1039/D1LC00131K.

[117] Y. Zheng *et al.*, "In vitro microvessels for the study of angiogenesis and thrombosis," *Proceedings of the National Academy of Sciences*, vol. 109, no. 24, pp. 9342–9347, June 2012, doi: 10.1073/pnas.1201240109.

[118] Y. S. Zhang *et al.*, "Bioprinted Thrombosis-on-a-Chip," *Lab Chip*, vol. 16, no. 21, pp. 4097–4105, Oct. 2016, doi: 10.1039/c6lc00380j.

[119] A. Shakeri *et al.*, "Engineering organ-on-a-chip systems for vascular diseases," *Arterioscler Thromb Vasc Biol*, vol. 43, no. 12, pp. 2241–2255, Dec. 2023, doi: 10.1161/ATVBAHA.123.318233.

[120] J. Zhou, Y.-S. Li, and S. Chien, "Shear Stress–Initiated Signaling and Its Regulation of Endothelial Function," *Arteriosclerosis, Thrombosis, and Vascular Biology*, vol. 34, no. 10, pp. 2191–2198, Oct. 2014, doi: 10.1161/ATVBAHA.114.303422.

[121] Y. I. Wang and M. L. Shuler, "UniChip enables long-term recirculating unidirectional perfusion with gravity-driven flow for microphysiological systems," *Lab Chip*, vol. 18, no. 17, pp. 2563–2574, Aug. 2018, doi: 10.1039/C8LC00394G.

[122] H. Ehlers, T. Olivier, S. J. Trietsch, P. Vulto, T. P. Burton, and L. J. van den Broek, "Microfluidic artery-on-a-chip model with unidirectional gravity-driven flow for high-throughput applications," *Lab Chip*, vol. 25, no. 10, pp. 2376–2389, May 2025, doi: 10.1039/D4LC01109K.

doi:10.6342/NTU202600103

[123] F. Mirzapour-Shafiyi *et al.*, "Flow-Induced Vascular Remodeling on-Chip: Implications for Anti-VEGF Therapy," *Advanced Functional Materials*, vol. n/a, no. n/a, p. 2501416, doi: 10.1002/adfm.202501416.

[124] "madar-ju.com/storage/images/files/file_1738964502J91C4.pdf." Accessed: Nov. 24, 2025. [Online]. Available: https://madar-ju.com/storage/images/files/file_1738964502J91C4.pdf

[125] S. J. Ling, W. Moebs, J. Sanny, S. J. Ling, W. Moebs, and J. Sanny, "9.4 Ohm's Law - University Physics Volume 2 | OpenStax." Accessed: Nov. 24, 2025. [Online]. Available: https://openstax.org/books/university-physics-volume-2/pages/9-4-ohms-law

[126] K. W. Oh, K. Lee, B. Ahn, and E. P. Furlani, "Design of pressure-driven microfluidic networks using electric circuit analogy," *Lab Chip*, vol. 12, no. 3, pp. 515–545, 2012, doi: 10.1039/C2LC20799K.

[127] H. Bruus, "Acoustofluidics 1: Governing equations in microfluidics," *Lab Chip*, vol. 11, no. 22, p. 3742, 2011, doi: 10.1039/c1lc20658c.

[128] D. Di Carlo, "Inertial microfluidics," *Lab Chip*, vol. 9, no. 21, p. 3038, 2009, doi: 10.1039/b912547g.

[129] H.-J. Wang and Y.-H. Hsu, "Study on the effect of shear stress on the remodeling of human vessel using a vessel-on-a-chip".

[130] J. Aaron, "Polydimethylsiloxane (PDMS) in Microfluidics: A Comprehensive Guide," Aline. Accessed: Nov. 30, 2025. [Online]. Available: https://www.alineinc.com/polydimethylsiloxane-pdms-in-microfluidics/

[131] I. Miranda *et al.*, "Properties and Applications of PDMS for Biomedical Engineering: A Review," *J Funct Biomater*, vol. 13, no. 1, p. 2, Dec. 2021, doi: 10.3390/jfb13010002.

doi:10.6342/NTU202600103

[132] I. T. Whelan, E. Moeendarbary, D. A. Hoey, and D. J. Kelly, “Biofabrication of vasculature in microphysiological models of bone,” *Biofabrication*, vol. 13, no. 3, p. 032004, July 2021, doi: 10.1088/1758-5090/ac04f7.

[133] C. B. X. Huang and T.-Y. Tu, “Recent advances in vascularized tumor-on-a-chip,” *Front Oncol*, vol. 13, p. 1150332, Mar. 2023, doi: 10.3389/fonc.2023.1150332.

[134] S. Shivani, H.-J. Wang, Y.-T. Chen, C.-T. Lin, and Y.-H. Hsu, “Self-assembled human arteriole-on-a-chip for arterial functionality testing and disease modeling,” *Lab on a Chip*, vol. 25, no. 20, pp. 5162–5179, 2025, doi: 10.1039/D5LC00530B.

[135] “3D Slicer image computing platform,” 3D Slicer. Accessed: Nov. 11, 2025. [Online]. Available: https://slicer.org/

[136] J. Sonne, A. Goyal, and W. Lopez-Ojeda, “Dopamine,” in *StatPearls*, Treasure Island (FL): StatPearls Publishing, 2025. Accessed: Nov. 17, 2025. [Online]. Available: http://www.ncbi.nlm.nih.gov/books/NBK535451/

[137] U. Pfeil *et al.*, “Intrinsic vascular dopamine – a key modulator of hypoxia-induced vasodilatation in splanchnic vessels,” *J Physiol*, vol. 592, no. Pt 8, pp. 1745–1756, Apr. 2014, doi: 10.1113/jphysiol.2013.262626.

[138] C. Zeng *et al.*, “Dopamine D1 Receptor Augmentation of D3 Receptor Action in Rat Aortic or Mesenteric Vascular Smooth Muscles,” *Hypertension*, vol. 43, no. 3, pp. 673–679, Mar. 2004, doi: 10.1161/01.HYP.0000118958.27649.6f.

[139] J. Reinsberg and R. Kullmann, “Characterization of Vascular Dopamine Receptors in the Gastric Circulation of the Rabbit,” *Journal of Cardiovascular Pharmacology*, vol. 8, no. 5, p. 1067, Sept. 1986.

[140] M. Bauer, “Cardiovascular Anatomy and Pharmacology,” *Basic Sciences in Anesthesia*, pp. 195–228, July 2017, doi: 10.1007/978-3-319-62067-1_11.

doi:10.6342/NTU202600103

[141] S. Ayyoub, R. Orriols, E. Oliver, and O. T. Ceide, “Thrombosis Models: An Overview of Common In Vivo and In Vitro Models of Thrombosis,” *Int J Mol Sci*, vol. 24, no. 3, p. 2569, Jan. 2023, doi: 10.3390/ijms24032569.

[142] K. Tomokiyo *et al.*, “Von Willebrand factor accelerates platelet adhesion and thrombus formation on a collagen surface in platelet-reduced blood under flow conditions,” *Blood*, vol. 105, no. 3, pp. 1078–1084, Feb. 2005, doi: 10.1182/blood-2004-05-1827.

[143] P. André *et al.*, “Platelets adhere to and translocate on von Willebrand factor presented by endothelium in stimulated veins,” *Blood*, vol. 96, no. 10, pp. 3322–3328, Nov. 2000, doi: 10.1182/blood.V96.10.3322.

[144] W. Zhu *et al.*, “Gut Microbial Metabolite TMAO Enhances Platelet Hyperreactivity and Thrombosis Risk,” *Cell*, vol. 165, no. 1, pp. 111–124, Mar. 2016, doi: 10.1016/j.cell.2016.02.011.

[145] H. Sano, M. Watanabe, T. Yamashita, K. Tanishita, and R. Sudo, “Control of vessel diameters mediated by flow-induced outward vascular remodeling in vitro,” *Biofabrication*, vol. 12, no. 4, p. 045008, July 2020, doi: 10.1088/1758-5090/ab9316.

[146] A. Blazeski *et al.*, “Engineering microvascular networks using a KLF2 reporter to probe flow-dependent endothelial cell function,” *Biomaterials*, vol. 311, p. 122686, Dec. 2024, doi: 10.1016/j.biomaterials.2024.122686.

[147] M. A. Winkelman, D. Y. Kim, S. Kakarla, A. Grath, N. Silvia, and G. Dai, “Interstitial flow enhances the formation, connectivity, and function of 3D brain microvascular networks generated within a microfluidic device,” *Lab Chip*, vol. 22, no. 1, pp. 170–192, Dec. 2021, doi: 10.1039/D1LC00605C.

doi:10.6342/NTU202600103

[148] S. Zhang, Z. Wan, G. Pavlou, A. X. Zhong, L. Xu, and R. D. Kamm, "Interstitial Flow Promotes the Formation of Functional Microvascular Networks In Vitro through Upregulation of Matrix Metalloproteinase-2," *Advanced Functional Materials*, vol. 32, no. 43, p. 2206767, 2022, doi: 10.1002/adfm.202206767.

[149] M. E. Cox and B. Dunn, "Oxygen diffusion in poly(dimethyl siloxane) using fluorescence quenching. I. Measurement technique and analysis," *Journal of Polymer Science Part A: Polymer Chemistry*, vol. 24, no. 4, pp. 621–636, 1986, doi: 10.1002/pola.1986.080240405.

[150] N. Baeyens *et al.*, "Vascular remodeling is governed by a VEGFR3-dependent fluid shear stress set point," *eLife*, vol. 4, p. e04645, Feb. 2015, doi: 10.7554/eLife.04645.

[151] E. R. Clark, "Studies on the growth of blood-vessels in the tail of the frog larva—by observation and experiment on the living animal," *American Journal of Anatomy*, vol. 23, no. 1, pp. 37–88, 1918, doi: 10.1002/aja.1000230103.

[152] Z.-D. Shi, X.-Y. Ji, H. Qazi, and J. M. Tarbell, "Interstitial flow promotes vascular fibroblast, myofibroblast, and smooth muscle cell motility in 3-D collagen I via upregulation of MMP-1," *Am J Physiol Heart Circ Physiol*, vol. 297, no. 4, pp. H1225–H1234, Oct. 2009, doi: 10.1152/ajpheart.00369.2009.

[153] A. Dardik, A. Yamashita, F. Aziz, H. Asada, and B. E. Sumpio, "Shear stress-stimulated endothelial cells induce smooth muscle cell chemotaxis via platelet-derived growth factor-BB and interleukin-1alpha," *J Vasc Surg*, vol. 41, no. 2, pp. 321–331, Feb. 2005, doi: 10.1016/j.jvs.2004.11.016.

[154] X. Han, N. Sakamoto, N. Tomita, H. Meng, M. Sato, and M. Ohta, "Influence of TGF-β1 expression in endothelial cells on smooth muscle cell phenotypes and MMP

doi:10.6342/NTU202600103

production under shear stress in a co-culture model," *Cytotechnology*, vol. 71, no. 2, pp. 489–496, Apr. 2019, doi: 10.1007/s10616-018-0268-7.

[155] M. Ohno, J. P. Cooke, V. J. Dzau, and G. H. Gibbons, "Fluid shear stress induces endothelial transforming growth factor beta-1 transcription and production. Modulation by potassium channel blockade.," *J Clin Invest*, vol. 95, no. 3, pp. 1363–1369, Mar. 1995, doi: 10.1172/JCI117787.

[156] T. Inai *et al.*, "Inhibition of vascular endothelial growth factor (VEGF) signaling in cancer causes loss of endothelial fenestrations, regression of tumor vessels, and appearance of basement membrane ghosts," *Am J Pathol*, vol. 165, no. 1, pp. 35–52, July 2004, doi: 10.1016/S0002-9440(10)63273-7.

[157] L. I. Los, M. J. van Luyn, and P. Nieuwenhuis, "Vascular remnants in the rabbit vitreous body. I. Morphological characteristics and relationship to vitreous embryonic development," *Exp Eye Res*, vol. 71, no. 2, pp. 143–151, Aug. 2000, doi: 10.1006/exer.2000.0864.

[158] "Wall shear stress revisited - ClinicalKey." Accessed: Dec. 01, 2025. [Online]. Available: https://www.clinicalkey.com/?adobe_mc=MCMID%3D06442181697255489850066943222557656725%7CMCORGID%3D4D6368F454EC41940A4C98A6%2540AdobeOrg%7CTS%3D1764581837#!/content/journal/1-s2.0-S1872931209000106

[159] C. Aalkjær and H. Nilsson, "Vasomotion: cellular background for the oscillator and for the synchronization of smooth muscle cells," *British Journal of Pharmacology*, vol. 144, no. 5, pp. 605–616, 2005, doi: 10.1038/sj.bjp.0706084.

[160] M. Lamboley, A. Schuster, J.-L. Bény, and J.-J. Meister, "Recruitment of smooth muscle cells and arterial vasomotion," *American Journal of Physiology-Heart and*

doi:10.6342/NTU202600103

Circulatory Physiology, vol. 285, no. 2, pp. H562–H569, Aug. 2003, doi: 10.1152/ajpheart.00526.2002.

[161] I. Armando, V. A. M. Villar, and P. A. Jose, "Dopamine and Renal Function and Blood Pressure Regulation," *Compr Physiol*, vol. 1, no. 3, pp. 1075–1117, July 2011, doi: 10.1002/cphy.c100032.

[162] N. K. R. Pandian, R. G. Mannino, W. A. Lam, and A. Jain, "Thrombosis-on-a-chip: Prospective impact of microphysiological models of vascular thrombosis," *Curr Opin Biomed Eng*, vol. 5, pp. 29–34, Mar. 2018, doi: 10.1016/j.cobme.2017.12.001.

[163] J. Berry, F. J. Peaudecerf, N. A. Masters, K. B. Neeves, R. E. Goldstein, and M. T. Harper, "An 'occlusive thrombosis-on-a-chip' microfluidic device for investigating the effect of anti-thrombotic drugs," *Lab Chip*, vol. 21, no. 21, pp. 4104–4117, Oct. 2021, doi: 10.1039/D1LC00347J.

[164] "In vitro microvessels for the study of angiogenesis and thrombosis | PNAS." Accessed: Dec. 02, 2025. [Online]. Available: https://www.pnas.org/doi/10.1073/pnas.1201240109

[165] A. Jain *et al.*, "Primary Human Lung Alveolus-on-a-chip Model of Intravascular Thrombosis for Assessment of Therapeutics," *Clin Pharmacol Ther*, vol. 103, no. 2, pp. 332–340, Feb. 2018, doi: 10.1002/cpt.742.

[166] R. Ross and J. A. Glomset, "Atherosclerosis and the arterial smooth muscle cell: Proliferation of smooth muscle is a key event in the genesis of the lesions of atherosclerosis," *Science*, vol. 180, no. 4093, pp. 1332–1339, June 1973, doi: 10.1126/science.180.4093.1332.

[167] J. Chen *et al.*, "Recent Progress in in vitro Models for Atherosclerosis Studies," *Front. Cardiovasc. Med.*, vol. 8, Jan. 2022, doi: 10.3389/fcvm.2021.790529.

doi:10.6342/NTU202600103

[168] B. J. Tefft, “A Sophisticated Model of Human Atherosclerosis on a Chip,” *Arteriosclerosis, Thrombosis, and Vascular Biology*, vol. 44, no. 12, pp. 2473–2475, Dec. 2024, doi: 10.1161/ATVBAHA.124.321804.

doi:10.6342/NTU202600103

10. Appendix

10.1 Certificate for reproduction of material from Lab on a Chip

Rights retained by authors

When the author accepts the exclusive licence to publish for a journal article, they retain certain rights that may be exercised without reference to the Royal Society of Chemistry.

- **Reproduce/republish portions of the article** (including the abstract).
- **Photocopy the article** and distribute such photocopies and copies of the PDF of the article for personal or professional use only (the Royal Society of Chemistry makes this PDF available to the corresponding author of the article upon publication. Any such copies should not be offered for sale. Persons who receive or access the PDF mentioned above must be notified that this may not be made available further or distributed.).
- **Adapt the article and reproduce adaptations of the article** for any purpose other than the commercial exploitation of a work similar to the original.
- **Reproduce, perform, transmit and otherwise communicate the article to the public** in spoken presentations (including those that are accompanied by visual material such as slides, overheads and computer projections).

As the article you are requesting to reproduce material from is published under a CC-BY open access licence (https://creativecommons.org/licenses/by/3.0/) you do not have to formally request permission to reproduce material from it. It is therefore ok for you to reproduce parts of the article in your own thesis provided you consider the points below.

Please note that if the material specified below or any part of it appears with credit or acknowledgement to a third party then you must also secure permission from that third party before reproducing that material.

Please ensure that the published article carries a credit to The Royal Society of Chemistry (see http://rsc.li/permissions for details) and that any electronic version of the work includes a hyperlink to the article on the Royal Society of Chemistry website.

With thanks

Best wishes

Becky

Becky Roberts
Contracts & Copyright Executive, Sales Operations
Royal Society of Chemistry
www.rsc.org

ROYAL SOCIETY OF CHEMISTRY

doi:10.6342/NTU202600103

10.2 Fluorescent Images

10.2.1 Fluorescent image for figures 5.12 and 5.15

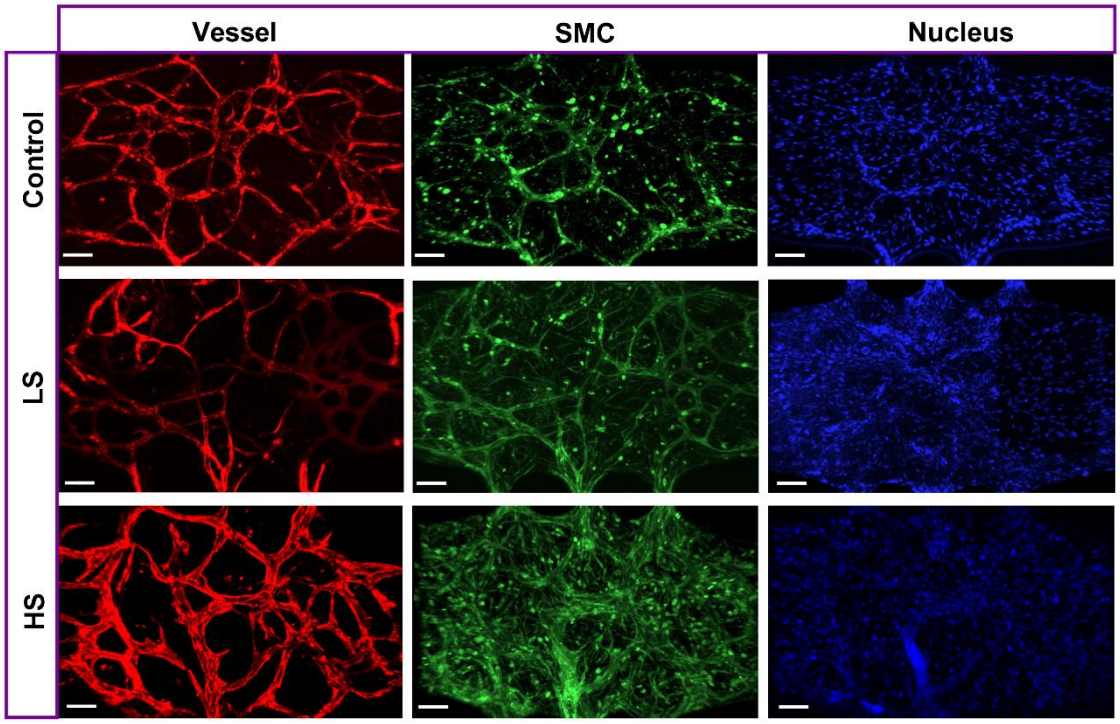

Figure 10-1 Fluorescent images of devices cultured in control, low shear (LS) and high shear (HS) devices. Red = CD31, green = Calponin, blue = Hoescht 33342 (scale bar = 100 μm)

doi:10.6342/NTU202600103

10.2.2 Fluorescent images for figure 5.22

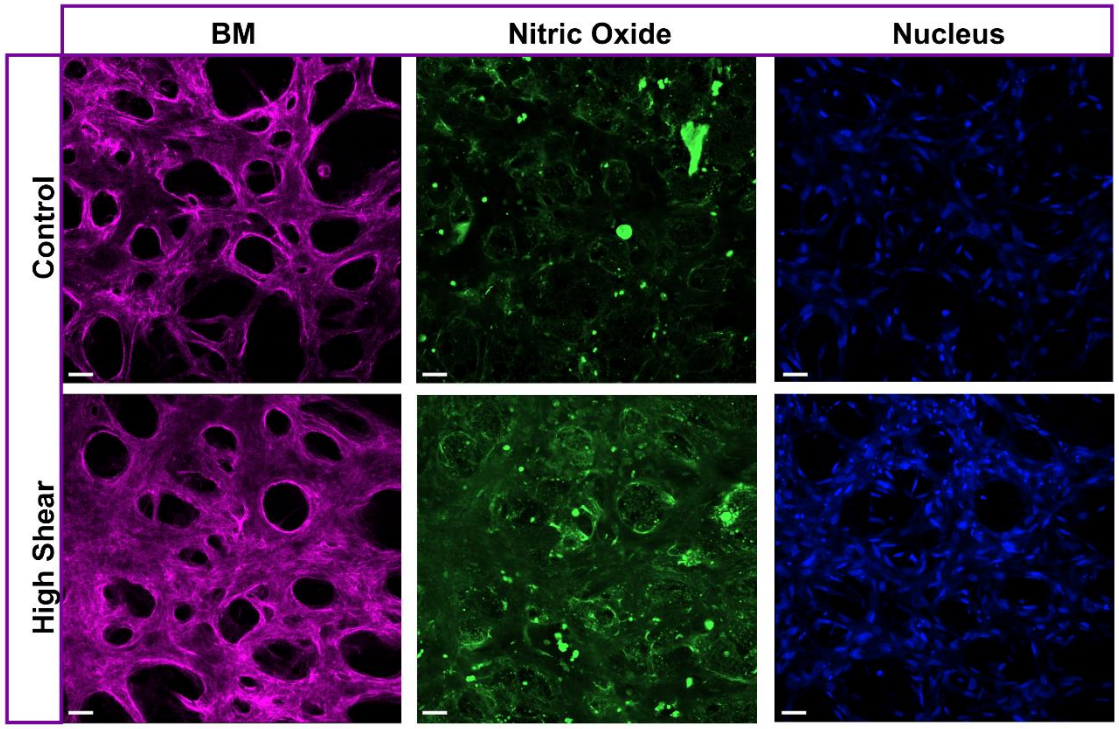

Figure 10-2 Fluorescent images of nitric oxide production in devices cultured in control, and high shear) devices. Purple = Collagen IV, green = DAF-FM diacetate, blue = Hoescht 33342 (scale bar = 50 μm)

10.2.3 Fluorescent images for figure 5.24 and 5.25

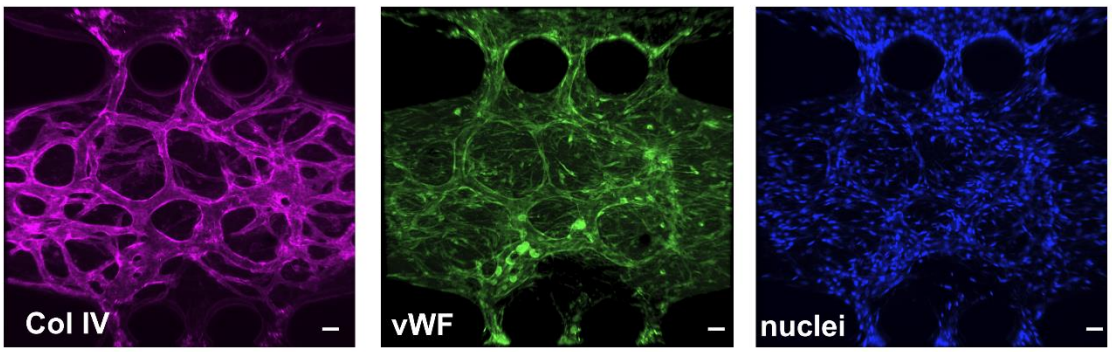

Figure 10-3 Fluorescent images of nitric oxide production in devices cultured in control, and high shear) devices. Purple = Collagen IV, green = vWF, blue = Hoescht 33342 (scale bar = 50 μm)

doi:10.6342/NTU202600103